



THESIS APPROVAL

GRADUATE SCHOOL, KASETSART UNIVERSITY

Master of Engineering (Advanced and Sustainable Environmental Engineering)

DEGREE

Advanced and Sustainable Environmental Engineering

Engineering

FIELD

FACULTY

TITLE: Synthesis and Characterization of Pd-Ni-Sn Electro-catalyst for Use in Direct Ethanol Fuel Cells

NAME: Mr. Sompoch Jonsomjit

THIS THESIS HAS BEEN ACCEPTED BY

THESIS ADVISOR

(Mrs. Paweena Prapainainar, Ph.D.)

THESIS CO-ADVISOR

(Ms. Korakot Sombatmankhong, Ph.D.)

**GRADUATE COMMITTEE
CHAIRMAN**

(Associate Professor Thongchai Rohitathisa Srinophakun, Ph.D.)

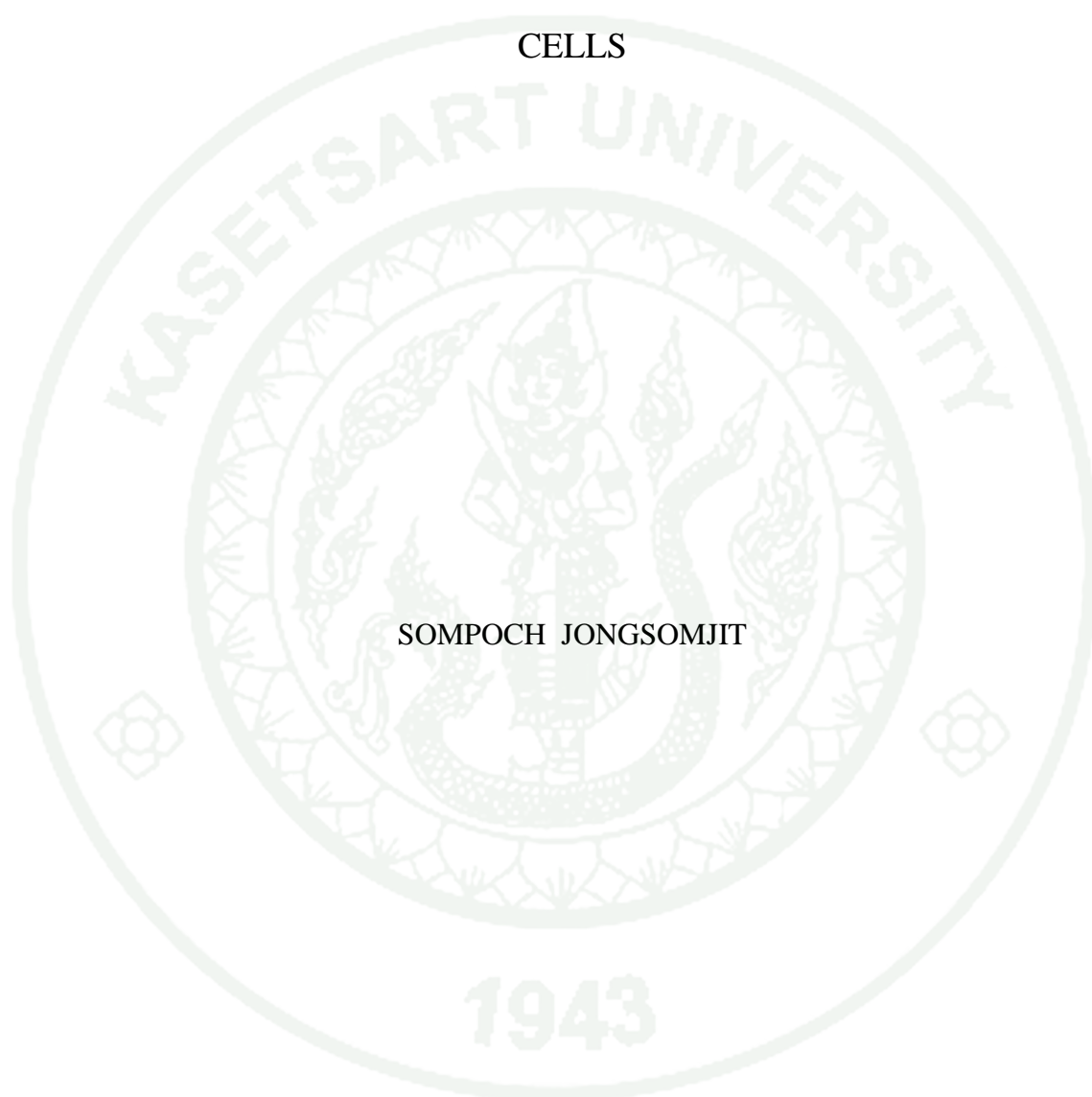
APPROVED BY THE GRADUATE SCHOOL ON _____

DEAN

(Associate Professor Gunjana Theeragool, D.Agr.)

THESIS

SYNTHESIS AND CHARACTERIZATION OF Pd-Ni-Sn
ELECTROCATALYST FOR USE IN DIRECT ETHANOL FUEL
CELLS



SOMPOCH JONGSOMJIT

A Thesis Submitted in Partial Fulfillment of
the Requirements for the Degree of
Master of Engineering (Advanced and Sustainable Environmental Engineering)
Graduate School, Kasetsart University

2014

Sompoch Jongsomjit 2014: Synthesis and Characterization of Pd-Ni-Sn Electrocatalyst for Use in Direct Ethanol Fuel Cells. Master of Engineering (Advanced and Sustainable Environmental Engineering), Major Field: Advanced and Sustainable Environmental Engineering, Faculty of Engineering. Thesis Advisor: Mrs. Paweena Prapainainar, Ph.D. 143 pages.

The sodium borohydride reduction method was used to prepare different Pd-Ni-Sn electrocatalytic compositions impregnated on carbon black (Vulcan XC-72R) for use in direct ethanol fuel cells (DEFCs). The as-prepared catalysts were mono catalyst, binary catalyst and ternary catalyst using Pd as a base catalyst. X-ray diffraction (XRD) results showed the presence of Ni(OH)₂ peak and SnO₂ peak with respect to the Ni content and the Sn content catalysts, respectively. The oxidation number was guaranteed by X-ray photoelectron spectroscopy (XPS). Transmission electron microscopy (TEM) was used to investigate the particle size of catalysts. The average particle size for all types of catalyst was in the range of 5.46-10.56 nm. Energy dispersive spectrometry (EDX) was employed to verify the ratio of metal loadings for all catalyst samples. Scanning electron microscopy (SEM) results demonstrated that the surface morphology was uniform for all catalysts. CO chemisorption was used to verify the number of active sites and the metal dispersion. Cyclic voltammetry (CV) was used to investigate the catalyst activity which associated to the ethanol oxidation reaction (EOR) in 1 M ethanol and in 1M KOH mixture solutions. It was found that the 20%Pd10%Ni10%Sn/CB ternary catalyst exhibited the highest current density of EOR. This composition was further used to be deposited on various supports with and without sulfuric and nitric acids functionalization. In addition, the electrochemical investigations including CO-tolerance, durability and electrochemical surface area (ESA) of catalysts were carried out. The 20%Pd10%Ni10%Sn on acid functionalized multi-walled carbon nanotubes showed the superior electrochemical properties. It is a good catalyst for DEFCs.

Student's signature

Thesis Advisor's signature

ACKNOWLEDGEMENTS

I would like to gratefully thank Dr. Paweena Prapainainar, my thesis advisor, and Dr. Korakot Sombatmankhong, my thesis co-advisor for advice, for their invaluable support, constant encouragement, and kindness to give suggestions and guidance toward the study including the revision of this thesis until its completion. I would sincerely like to thank Associate Professor Dr. Manop Charoenchaitrakool my examination chairperson and Assistant Professor Dr. Nisit Tantavichet my external examiner for their devote time, valuable comment and suggestion. I would like to thank Associate Professor Dr. Shisuke Mori for devote time and suggestion. I would like to thank Associate Professor Dr. Thongchai Rohitathisa Srinophakun, the program director, for many suggestions and comments.

All financial supports in this research were from Kasetsart University Research and Development Institute (KURDI). The National Metal and Materials Technology Center (MTEC), NSTDA have supported place for doing research, some testing and characterizations in this research. The Department of Chemical Engineering of Kasetsart University was supported for a place and equipment for doing some parts of research. And the financial of tuition was supported Thailand Advanced Institute of Science and Technology and Tokyo Institute of Technology (TAIST-Tokyo tech).

I am especially appreciated my parents and brothers for their continuing encouragements. Finally, thanks to all my friends and member of Materials for Energy Research Unit, MTEC for suggestions throughout the research.

Sompoch Jongsomjit

July 2014

TABLE OF CONTENTS

	Page
TABLE OF CONTENTS	i
LIST OF TABLES	ii
LIST OF FIGURES	v
LIST OF ABBREVIATIONS	x
INTRODUCTION	1
OBJECTIVES	4
LITERATURE REVIEW	5
MATERIALS AND METHODS	35
Materials	35
Methods	36
RESULTS AND DISCUSSION	43
CONCLUSION AND RECOMMENDATIONS	89
Conclusion	89
Recommendations	90
LITERATURE CITED	92
APPENDICES	108
Appendix A Calculation for catalyst preparation	109
Appendix B Additional XRD data	112
Appendix C Histogram of particle size distribution of carbon supports and other magnification of SEM images	114
Appendix D CO chemisorption results	122
Appendix E The TGA thermograms and difference curves	127
Appendix F The isotherm results and adsorption isotherm and hysteresis loop standard of IUPAC	130
Appendix G XPS spectra data	137
Appendix H The equations for reversible systems	140
CURRICULUM VITAE	143

LIST OF TABLES

Table		Page
1	Comparison of fuel cell technologies	10
2	The characterization of carbon blacks	14
3	The characterization of CNTs and CNFs	15
4	Summary of all materials and instruments	35
5	The details of metal compositions synthesis in this research work with their abbreviations	37
6	A summary of XRD parameters extracted from Pd (1 1 1) peak at 39.901°	45
7	A summary of XRD parameters extracted from Pd (2 2 0) peak at 67.618°	46
8	A comparison between the desired and actual compositions of as-prepared electrocatalytic using SEM-EDX technique	48
9	The metal dispersion and numbers of active sites of different catalyst compositions	52
10	The data extracted from cyclic voltammograms of different catalyst compositions for EOR in a mixture of 1M KOH and 1M ethanol at a scan rate of 50 mV s ⁻¹ corresponding to Figure 17	54
11	The onset potential and peak potential of all catalyst compositions for CO oxidation activity corresponding to the voltammograms in Figure 19	58
12	The area under the desorbed OH ⁻ peak (Qs) and ESA of different catalyst compositions	59
13	The I _D /I _G ratio of carbon supports	59
14	Summary of BET surface area, average pore size and total pore volume	65
15	Summary of XRD calculation of peak Pd (2 2 0)	69

LIST OF TABLES (Continued)

Table		Page
16	A comparison between the desired and actual compositions of as-prepared electrocatalysts deposited on various supports	74
17	The metal dispersion and number of active sites of 20%Pd10%Ni10%Sn on various supports	77
18	XPS area ratios of chemical state of Pd, Ni and Sn species	83
19	The data extracted from cyclic voltammograms of 20%Pd10%Ni10%Sn using different types of catalyst supports with/with no functionalization in a mixture of 1 M KOH and 1M ethanol at a scan rate of 50 mA s ⁻¹ corresponding to Figure 40	84
20	Electrochemical CO oxidation activity of 20%Pd10%Ni10%Sn catalyst on various supports	87
21	The area of desorbed OH ⁻ peak and ESA of 20%Pd10%Ni10%Sn catalyst on various supports	88
 Appendix Table		
A1	Chemical properties of substance for catalyst synthesis	109
A2	Summary of the weight of substances for catalyst synthesis	110
D1	CO chemisorption of 20%Pd/CB (catalyst weight = 0.0250 g)	122
D2	CO chemisorption of 20%Pd20%Sn/CB (catalyst weight = 0.0245 g)	122
D3	CO chemisorption of 20%Pd20%Ni/CB (catalyst weight = 0.0260 g)	122
D4	CO chemisorption of 20%Pd5%Ni15%Sn/CB (catalyst weight = 0.0301 g)	124

LIST OF TABLES (Continued)

Appendix Table		Page
D5	CO chemisorption of 20%Pd10%Ni10%Sn/CB (catalyst weight = 0.0278 g)	123
D6	CO chemisorption of 20%Pd15%Ni5%Sn/CB (catalyst weight = 0.0240 g)	123
D7	CO chemisorption of 20%Pd10%Ni10%Sn/CB (catalyst weight = 0.0278 g)	124
D8	CO chemisorption of 20%Pd10%Ni10%Sn/MWCNT (catalyst weight = 0.0214 g)	124
D9	CO chemisorption of 20%Pd10%Ni10%Sn/CB _{sn} (catalyst weight = 0.0216 g)	124
D10	CO chemisorption of 20%Pd10%Ni10%Sn/MWCNT _{sn} (catalyst weight = 0.0252 g)	125

LIST OF FIGURES

Figure		Page
1	The component of single cell of fuel cells	8
2	The schematics of reactant flow of each type of fuel cells	9
3	CV excitation signal	21
4	A cyclic voltammogram of single electron oxidation-reduction reaction	21
5	The mechanism of Pd catalyst with MtO _x promoter	27
6	XPS spectra of (a) Pd ₂ Ni ₃ /C (b) Ni 2p XPS spectrum of Pd ₂ Ni ₃ /C	28
7	Different synthesis pathways for co-reduction process	29
8	The treatment of MWCNTs with acid and followed by rapid microwave-assisted solvothermal	30
9	Schematic of anion and cation exchange membrane direct ethanol fuel cells	33
10	Different DEFC systems	34
11	XRD patterns of prepared electrocatalysts compositions, 2θ = 10-90°	45
12	SEM images (taken at the magnification of 30,000×) of (a) 20%Pd/CB, (b) 20%Pd20%Sn/CB, (c) 20%Pd20%Ni/CB, (d) 20%Pd5%Ni15%Sn/CB, (e) 20%Pd10%Ni-10%Sn/CB and (f) 20%Pd15%Ni5%Sn/CB	47
13	TEM images at 50,000× magnification of (a) 20%Pd/CB, (b) 20%Pd20%Sn/CB, (c) 20%Pd20%Ni/CB, 20%Pd5%Ni15%Sn/CB, (e) 20%Pd10%Ni10%Sn/CB and (f) 20%Pd15%Ni5%Sn/CB	49

LIST OF FIGURES (Continued)

Figure		Page
14	Particle size distribution histograms of (a) 20%Pd/CB, (b) 20%Pd20%Sn/CB, (c) 20%Pd20%Ni/CB, (d) 20%Pd5%Ni-15%Sn/CB, (e) 20%Pd10%Ni10%Sn/CB and (f) 20%Pd15%Ni5%Sn/CB	50
15	TPR profile of 20%Pd/CB catalyst	51
16	Pathways of electrooxidation reaction of ethanol in alkaline media	53
17	Cyclic voltammograms of different catalyst compositions for EOR in a mixture of 1 M KOH and 1 M ethanol at a scan rate of 50 mV s^{-1}	54
18	Chronoamperometric curves of different catalyst compositions in 1 M ethanol containing 1M KOH solution at -0.3 V	55
19	CO stripping voltammograms of all catalyst compositions in 1 M KOH solution	57
20	Cyclic voltammograms for different catalyst compositions in 1 M KOH solution	59
21	SEM images of CB with magnifications of (a) $30,000\times$ and (b) $60,000\times$	61
22	SEM images of CB_{sn} with magnifications of (a) $30,000\times$ and (b) $60,000\times$	61
23	SEM images of MWCNT with magnifications of (a) $30,000\times$ and (b) $60,000\times$	62
24	SEM images of MWCNT_{sn} with magnifications of (a) $30,000\times$ and (b) $60,000\times$	62
25	The Raman spectrum of MWCNT and MWCNT_{sn}	64
26	The Raman spectrum of CB and CB_{sn}	64
27	TGA thermograms of different carbon supports	66

LIST OF FIGURES (Continued)

Figure		Page
28	The FTIR spectrum of MWCNT and MWCNT _{sn}	67
29	The FTIR spectrum of CB and CB _{sn}	67
30	BET plots of functionalized and non-functionalized supports	69
31	The pore size distribution of different carbon supports and inset graph of the micropore and mesopore size distributions of carbon supports	70
32	XRD patterns of the as-prepared 20%Pd10%Ni10%Sn electro-catalyst on various carbon supports, $2\theta = 20-90^\circ$	71
33	SEM images of (a) 20%Pd10%Ni10%Sn/CB, (b) 20%Pd10%Ni10%Sn/CB _{sn} , (c) 20%Pd10%Ni10%Sn/MWCNT and (d) 20%Pd10%Ni10%Sn/MWCNT _{sn} .	73
34	TEM images at $\times 50,000$ magnification of (a) 20%Pd10%Ni10%Sn/CB, (b) 20%Pd10%Ni10%Sn/CB _{sn} , (c) 20%Pd10%Ni10%Sn/MWCNT and (d) 20%Pd10%Ni10%Sn/MWCNT _{sn}	75
35	Particle size distributions for (a) 20%Pd10%Ni10%Sn/CB, (b) 20%Pd10%Ni10%Sn/CB _{sn} , (c) 20%Pd10%Ni10%Sn/MWCNT and (d) 20%Pd10%Ni10%Sn/MWCNT _{sn}	76
36	The survey XPS spectrum of (a) 20%Pd10%Ni10%Sn/CB _{sn} and (b) 20%Pd10%Ni10%Sn/MWCNT _{sn}	79
37	The detailed XPS spectrum of Pd for (a) 20%Pd10%Ni10%Sn/CB _{sn} and (b) 20%Pd10%Ni10%Sn/MWCNT _{sn}	80
38	The detailed XPS spectrum of Ni for (a) 20%Pd10%Ni10%Sn/CB _{sn} (b) 20%Pd10%Ni10%Sn/MWCNT _{sn}	81
39	The detailed XPS spectra XPS of Sn for (a) 20%Pd10%Ni10%Sn/CB _{sn} (b) 20%Pd10%Ni10%Sn/MWCNT _{sn}	82

LIST OF FIGURES (Continued)

Figure		Page
40	The voltammograms of 20%Pd10%Ni10%Sn on different types of catalyst supports with/with no functionalization in a mixture of 1 Methanol and 1 M KOH	84
41	Chronoamperometric curve of 20%Pd10%Ni10%Sn catalyst using different catalyst supports in a mixture of 1 M ethanol and 1 M KOH solution at an applied potential of -0.3 V	85
42	CO stripping voltammograms of 20%Pd10%Ni10%Sn catalyst on various supports	86
43	Cyclic voltammograms of 20%Pd10%Ni10%Sn catalyst on various supports in 1M KOH solution	88
Appendix Figure		
C11	SEM images of 20%Pd10%Ni10%Sn/CB, (a) $\times 60,000$ and (b) $\times 80,000$	119
C12	SEM images of 20%Pd10%Ni10%Sn/CB _{sn} , (a) $\times 60,000$ and (b) $\times 80,000$	119
C13	SEM images of 20%Pd10%Ni10%Sn/MWCNT, (a) $\times 60,000$ and (b) $\times 80,000$	120
C14	SEM images of 20%Pd10%Ni10%Sn/MWCNT _{sn} , (a) $\times 60,000$ and (b) $\times 80,000$	120
E1	The TGA thermograms and differential curve of (a) CB and (b) CB _{sn}	127
E2	The TGA thermograms and differential curve of (a) MWCNT and (b) MWCNT _{sn}	128
F1	The isotherm of CB _{sn} support	130
F2	The isotherm of MWCNT _{sn} support	130

LIST OF FIGURES (Continued)

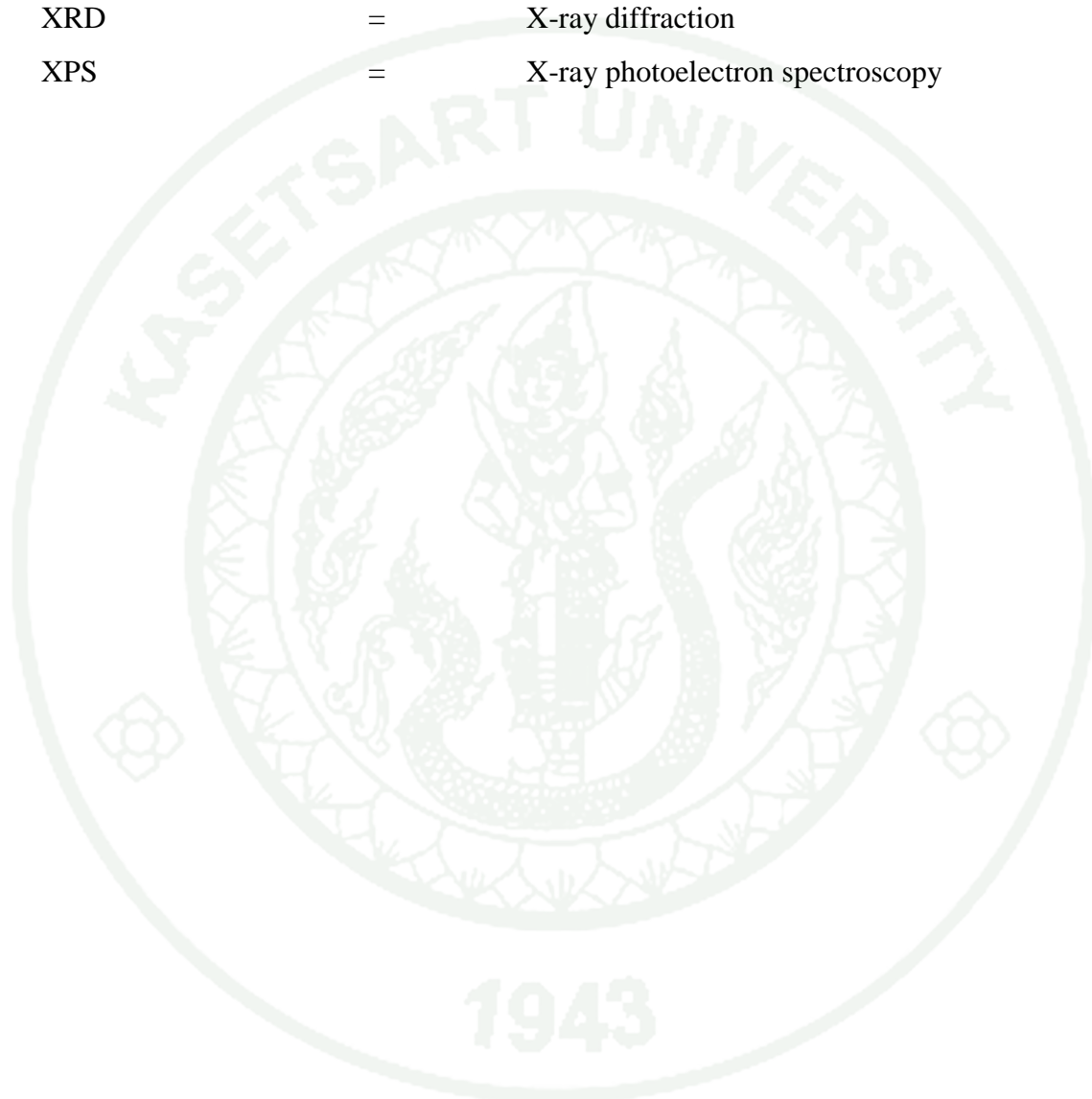
Appendix Figure		Page
F3	The isotherm of CB support	131
F4	The isotherm of MWCNT support	131
F5	The adsorption isotherm types of IUPAC standard	132
F6	The hysteresis loop types of IUPAC standard	133
F7	BET plot of CBsn support	135
G1	XPS spectra of C for 20%Pd10%Ni10%Sn/CB _{sn}	137
G2	XPS spectra of C for 20%Pd10%Ni10%Sn/MWCNT _{sn}	137
G3	XPS spectra of oxygen for 20%Pd10%Ni10%Sn/CB _{sn}	138
G4	XPS spectra of oxygen for 20%Pd10%Ni10%Sn /MWCNT _{sn}	138

LIST OF ABBREVIATIONS

AFC	=	Alkaline fuel cell
AEM	=	Anion exchange membrane
CB	=	Carbon black Vulcan XC-72R
CB _{sn}	=	Carbon black Vulcan XC-72R with functionalization
CEM	=	Cation exchange membrane
CA	=	Chronoamperometry
CE	=	Counter electrode
CV	=	Cyclic voltammetry
DAFC	=	Direct alcohol fuel cell
DMFC	=	Direct methanol fuel cell
ESA	=	Electrochemical surface area
EDX	=	Energy dispersive X-ray spectroscopy
EOR	=	Ethanol oxidation reaction
FTIR	=	Fourier transform Infrared Spectroscopy
GDL	=	Gas diffusion layer
MEA	=	Membrane electrode assembly
MCFC	=	Molten carbonate fuel cell
MWCNT	=	Multi-walled carbon nanotubes
MWCNT _{sn}	=	Multi-walled carbon nanotubes with functionalization
ORR	=	Oxygen reduction reaction
PAFC	=	Phosphoric acid fuel cell
PEMFC	=	Proton exchange membrane fuel cell
RE	=	Reference electrode
SEM	=	Scanning electron microscopy
SOFC	=	Solid oxide fuel cell
BET	=	Surface area and porosity analyzer
TGA	=	Thermogravimetric analysis

LIST OF ABBREVIATIONS (Continued)

TEM	=	transmission electron microscopy
WE	=	Working electrode
XRD	=	X-ray diffraction
XPS	=	X-ray photoelectron spectroscopy



SYNTHESIS AND CHARACTERIZATION OF Pd-Ni-Sn ELECTROCATALYST FOR USE IN DIRECT ETHANOL FUEL CELLS

INTRODUCTION

Nowadays, energy sources have been extensively concerned because most energy has been produced from fossil fuels. Presently, the fossil fuels are running out because the formation rate and consumption rate of fossil fuels are inversely. The fossil fuel consumption has been increased due to the increasing of population and technology. The energy consumption and production process cause the environmental problems. This leads to the search for an alternative energy which is environmental friendly. Several researchers have attempted to build new green innovation and technology to produce energy. A fuel cell is one of promising choices to replace old methods for energy production (Andújar and Segura, 2009; Corbo *et al.*, 2007; Nguyen *et al.*, 2011).

A fuel cell is a device which produces electricity via electrochemical reaction without combustion as often associated with the conventional process. Therefore it yields higher efficiency as it is not limited by Canot efficiency. Moreover, it is low emission when compared to the combustion process (Lutz *et al.*, 2002). Different types of fuel cells have been developed. The most popular one is a proton exchange membrane fuel cells (PEMFCs) because it operates at low temperature and low pressure. It also requires less catalyst loading than other types do and it has higher durability than others have (Hsieh *et al.*, 2011). PEMFCs were applicable for high power requirement devices such as back-up power, automotive and portable power (Lee *et al.*, 2010; Yuan *et al.*, 2011). However, PEMFCs have some disadvantages regarding the storage of explosive hydrogen gas. To solve the fuel storage problem the direct alcohol fuel cells (DAFCs) has been developed as a portable energy sources (David *et al.*, 2014). The alcohol fuels can be methanol, ethanol and 2-propanol which have energy densities of 6.09, 8.00 and 8.58 kWh kg⁻¹, respectively (Antolini and

Gonzalez, 2010; Chu and Shul, 2010). Among them, the most widely used fuel for DAFCs is methanol. However the methanol fuel has low activity to oxidation reaction and causes fuel crossover to cathode; this results low efficiency of the fuel cell. Ethanol is then exploited because of its lower ethanol crossover and higher energy density when compare to methanol. Furthermore, ethanol can be produced form bioprocess; thus it can reduce the production of greenhouse gas (Roelofs *et al.*, 2011).

The advantages of direct alcohol fuel cell are low operating cost and high corrosive resistance. The kinetic rate of ethanol oxidation reaction in alkaline DEFCs is higher than that of DEFCs in acid media. The acid or alkaline media of direct ethanol fuel cell has strongly effect on ethanol oxidation reaction. Platinum-based catalysts exhibit good activity of EOR in acid media. On the other hand, other noble metals (Pd, Ru, Au, Ag) and non-noble metal (Ni) catalysts exhibit activity in alkaline media rather than acid media. These metals are cheaper than platinum (Antolini and Gonzalez, 2010). However, the catalysts have low stability to anodic reaction under low temperature operation of the DEFCs. This is due to electrode the poisoning occurring on the catalyst surface by the CO intermediate. Many researchers have attempted to find non-noble and other noble metal catalysts which have high catalytic activity and simultaneously high poisoning durability (An *et al.*, 2013b; An *et al.*, 2013a; Cai *et al.*, 2013; Castro *et al.*, 2012; Jin *et al.*, 2012; Liu *et al.*, 2009; Merino-Jimenez *et al.*, 2014; Modibedi *et al.*, 2011; Neto *et al.*, 2011; Nie *et al.*, 2007; Qi *et al.*, 2011; Tarasevich *et al.*, 2009; Wang *et al.*, 2008; Wongyao *et al.*, 2011; Xu *et al.*, 2010). The acid media or alkaline media is selected depending on the types of membrane. In alkaline media, both anion exchange membrane (AEM) and cation exchange membrane (CEM) can be used (An and Zhao, 2011; An *et al.*, 2012). In acid media, CEM is the only suitable membrane (An *et al.*, 2011a).

In this work, the palladium-based catalysts for DEFCs was synthesized and characterized to increase the fuel cell efficiency and to reduce the cost of catalysts. The three metals were selected including palladium (Pd), nickel (Ni), and tin (Sn) deposited on two types of carbon supports. Pd resources are abundant in nature with the price cheaper than platinum. The catalytic activity are as good as Pt. Ni was used

to increase the activity and the stability of Pd while Sn was used to facilitate the adsorption of CO-intermediate which occurred during the oxidation reaction (Tayal *et al.*, 2011). The compositions of three metals catalysts were first varied on carbon black (CB). The sodium borohydride reduction method was used to synthesize these catalysts according to Shen *et al.* (Shen *et al.*, 2010). They studied the synthesis of Pd₂Ni₃ on carbon black using sodium borohydride reduction method and found that the catalyst nano-particle exhibited a good dispersion and activity for ethanol oxidation reaction (EOR) with a high power density of 90 mW cm⁻² (Shen *et al.*, 2010). In present work, the EOR activity was tested in alkaline media. The catalyst support was found to be one in many factors to increase the activity of catalysts (Bambagioni *et al.*, 2009; Modibedi *et al.*, 2011). The best catalyst composition for EOR was then used to study effect of carbon based supports including carbon black, acid functionalized carbon black (CB_{sn}), multi-walled carbon nanotubes (MWCNT) and acid functionalized multi-walled carbon nanotubes (MWCNT_{sn}). The HNO₃ and H₂SO₄ treatment was carried out according to Osorio *et al.* procedure (Osorio *et al.*, 2008).

OBJECTIVES

1. To synthesize and investigate the most suitable composition for ethanol oxidation reaction of Pd based tri-metallic catalyst.
2. To investigate the effect of types of carbon supports and functionalization on the catalyst performance.
3. To characterize physical and electrochemical properties of the as prepared catalysts.

Scope of work

1. The catalyst composition were synthesized using sodium borohydride reduction method Metal, binary, ternary catalytic systems containing palladium (Pd), nickel (Ni) and tin (Sn) were synthesized with the different compositions of 20%Pd/CB, 20%Pd20%Ni/CB, 20%Pd20%Sn/CB, 20%Pd15%Ni5%Sn/CB, 20%Pd10%Ni10%Sn, 20%Pd5%Ni15%Sn/CB (weight for all compositions percentage). The proper catalyst composition was determined by current density for EOR and CB, CB_{sn}, MWCNT and MWCNT_{sn}.

2. Characterizations of physical properties were investigated by X-ray diffraction (XRD), scanning electron microscopy (SEM), energy dispersive X-ray spectroscopy (EDX), transmission electron microscopy (TEM), X-ray photoelectron spectroscopy (XPS), Fourier transform infrared spectroscopy (FTIR), thermogravimetric analysis (TGA), Raman imaging microscopy, surface area and porosity analyzer, chemisorption. Characterizations of chemical properties were electrochemical tests consisting of activity, durability, CO tolerance and electrochemical surface area (ESA).

LITERATURE REVIEW

Theory

1. Fuel cell definition

A fuel cell is an apparatus or equipment that is capable of producing electricity at high efficiency through electrochemical reaction. The chemical bonds of the fuel's molecules are converted into electrical energy without going through combustion process. Battery and fuel cell are similar in a way that many of them can be combined from small units into a large unit to increase its energy capacity. A fuel cell is different in a way that it can produce electricity continuously without charging as long as a fuel is fed into the system whether in gas or liquid form.

2. History

In 1838, Christian Friedrich Schoenbein started to study the principle of fuel cell and published it in 1839. Not long after, William Robert Grove invented a wet battery cell which was called "Grove cell" operating in acid solution using Pt and Zn electrodes. Moreover, it was also applied electrode to gas system using H₂ and O₂ gas but the voltage and current were very low. In 1889, Mond and Carl Langer explained the phenomenon of the gas battery which could produce electricity of 6 A ft² at 0.73 V. Moreover in 1893, Friediech explained the principle operation of fuel cell that it was similar to battery. That knowledge was useful for fuel cell researches. In 1896, William intrigued the scientific community in 1896 by producing electricity directly from charcoal which it was so-called "carbon battery".

In 1958, Bacon had demonstrated the alkaline-type fuel cell. In theory, fuel cell showed the highest efficiency at 85% because it was not limited by Carnot cycle. It was only limited by thermodynamic. However, the actual efficiency must be measured before uses. Until around 1960, hydrogen fuel cell had been developed for

United States' Apollo space program to produce energy and drinking water. After that, fuel cell has rigorously developed during the 20th century (Robert *et al.*, 2014). Recently, there are many manufactures that have been interested in developing fuel cells for different kinds of uses (Andújar and Segura, 2009).

3. Fuel cell components

Fuel cell such as proton exchange membrane and direct ethanol fuel cell normally comprises 5 main parts as follows:

3.1 Membrane electrode assembly (MEA)

MEA comprises anode and cathode catalyst layer (catalyst coating on glassy carbon paper) and a proton exchange membrane. MEA is one factor which is important to efficiency of cell (Thanasilp and Hunsom, 2010).

3.1.1 Membrane is the electrolyte which can be some ion pass. The membrane made from fluoro-sulfonate polymers and they have commercial name are Nafion, Flemion, Aciplex, and Neosepta-F etc. Thickness of membrane is about 50-175 micron (Reeve, 2002). The membrane is solid phase so ionization or leak same liquid electrolytes. It acts as an insulator for electron but allows proton to permeate. Also, it is resistant to chemicals, heat, gas and water retention. The limitation of the membrane is that it cannot be used at the temperature higher than water's boiling point since the water content in the membrane strongly affects the proton-conducting capacity. On the other hand, excessive amount of water content lead to the cell submerges and causes a drop in efficiency.

3.1.2 Catalyst is the part which uses to increase the rate of fuel-fed or chemical-fed reaction. Platinum is one of the most widely used as catalyst for oxidation and reduction. Nevertheless, the high price of platinum triggers researchers to search for cheaper metal alternatives or way to reduce platinum use. The efficiency of a catalyst depends on the particle arrangement in the catalytic layer. An ideal

catalyst structure should contain high level of three phase boundaries in which catalyst, fuel molecule and electrolyte meet.

3.2 Gas diffusion layer (GDL)

GDL conveys the starting material to a catalyst. It also controls the water level inside the membrane by transporting the water by-product out. A good GDL will maintain a good balance of water level in electrolyte such that the fuel cell is moist but does not trap water inside (Vielstich *et al.*, 2003).

3.3 Bipolar plate

Normally, metallic plate and graphite plate are put into fuel cell to reduce and to distribute gas pressure. The form, the width and the depth of a plate affect the gas distribution significantly. Moreover, a good design can improve the passage of fuel to membrane and the drainage of water from cathode (Heinzel *et al.*, 2009).

3.4 Current collector

Electrons from oxidation reaction pass through the current collectors to produce electricity. It acts as a receiver and an emitter of electrons that can be classified as anode and cathode, respectively. Electrons travel through the gas diffusion layer to the current collector, to external circuit and finally to the cathode collector. The external circuit is connected to electrical appliances such as light bulbs to complete the electric cycle.

3.5 End Plates

The end plates are put on two sides of a fuel cell to keep all components together. It is impermeable to gaseous elements but is a good electron conductor. Endplates are made of normally graphite or metallic material to avoid leakage problems.

The component of single cell is shown in Figure 1 (Lucy, 2003)

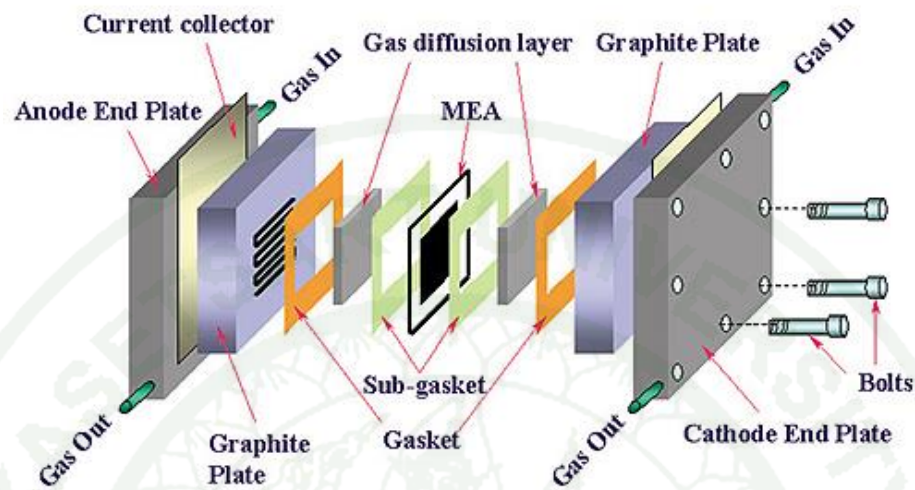


Figure 1 The component of single cell in fuel cells.

Source: Lucy (2003)

4. Types of Fuel Cell

The fuel cell has several types which are different depending on electrolyte and fuel used. They can be classified into 6 types as follows: alkaline fuel cells (AFCs), molten carbonate fuel cell (MCFCs), phosphoric acid fuel cell (PAFCs), solid oxide fuel cells (SOFCs), proton exchange membrane fuel cell (PEMFC) and direct methanol fuel cell (DMFCs) and direct ethanol fuel cell (DEFCs). The schematics of reactant flow in each type of fuel cells are shown in Figure 2 (Rose *et al.*, 2014) and the details are given in Table 1. The platinum catalyst and combination catalyst such as nickel and others metal catalysts were used on anode electrode. DMFCs produce electricity by using methanol fuel. The operating temperature is 50-120 °C and the cell efficiency can be over 40 %. The fuel cell stack can produce electricity between <1-5 kW. This cell exhibits good performance at low temperature with additional benefits such as high durability, small size and light weight which is suitable for home power and automotive. In addition, DMFCs are suitable for small appliances such as

computer notebook, sound portable, and mobile phone. The working principle of DMFC is also shown in Figure 2. Methanol reacts with water and converted to carbon dioxide, protons and electrons. The electrons pass through an external load to cathode. The protons pass through the electrolyte membrane. The oxygen receives electrons and protons and then generates water as shown in equation (1), (2) and (3). In DEFC, ethanol is used instead of methanol. The anode reaction changes to ethanol oxidation (Achmad *et al.*, 2011).

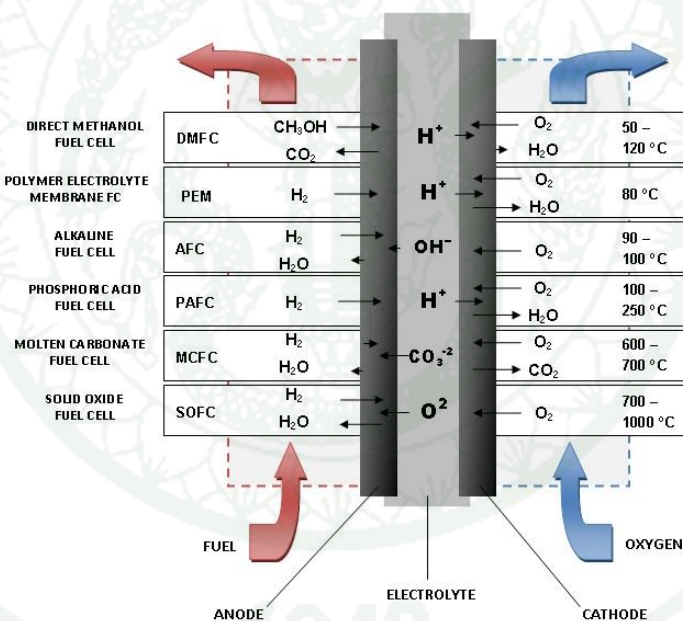


Figure 2 The schematic of reactant flow for each type of fuel cells.

Source: Rose *et al.* (2014)

Table 1 Comparison of fuel cell technologies.

Fuel cell Type	Common Electrolyte	Operating Temperature	Efficiency	Advantages	Disadvantages	References
Alkaline Fuel Cells (AFCs)	Aqueous solution of potassium hydroxide soaked in a matrix	90-100 °C	60%	-Fast cathode reaction in alkaline electrolyte, leads to high performance -Low cost of components	-Sensitive to CO ₂ in fuel cell -Electrolyte management	(Geeter <i>et al.</i> , 1999)
Molten Carbonate Fuel Cells (MCFCs)	Solution of lithium, sodium, and/or potassium carbonates soaked in a matrix	600-700 °C	45-50%	-High efficiency -Fuel flexibility -A variety of catalysts -Suitable for CHP	-High temperature corrosion and breakdown of cell components -Long start up time -Low power density	(Mekhilef <i>et al.</i> , 2012)

Table 1 (Continued).

Fuel cell Type	Common Electrolyte	Operating Temperature	Efficiency	Advantages	Disadvantages	References
Phosphoric Acid Fuel Cells (PAFC)	Phosphoric acid soaked in a matrix	150-200 °C	40%	-Higher temperature enables CHP -High tolerance to fuel impurities	-Pt catalyst -Long start up time -Low current densities	(Andújar and Segura, 2009)
Solid Oxide Fuel Cells (SOFC)	Yttria stabilized zirconia	700-1000 °C	60%	-High cell efficiency -Fuel cell flexibility -A variety of catalysts -Suitable for CHP&CHHP -Hybrid/GT cycle	-High temperature corrosion and breakdown of cell components -High temperature operation requires long start up time and limits	(Qi <i>et al.</i> , 2008)

Note: CHP is stand for combined heat and power
 CHHP is stand for combined heat, hydrogen and power

Table 1 (Continued).

Fuel cell Type	Common Electrolyte	Operating Temperature	Efficiency	Advantages	Disadvantages	References
Proton Exchange Membrane Fuel Cells (PEMFC)	Perfluoro sulfonic acid	50-100 °C	60% transportation, 35% stationary	-Solid electrolyte reduce corrosion & electrolyte management problems -Low temperature -Quick start up	-Expensive catalyst -Sensitive to impurities -Low temperature waste heat -Hydrogen storage problem	(Peighambardou <i>et al.</i> , 2010)
Direct Methanol and Direct Ethanol Fuel Cells (DMFCs & DEFCs)	Perfluoro sulfonic acid (nafion), Polybenzimidazoe (PBI)	50-120 °C	Up to 40%	-Simpler system design -Working atmosphere -Long membrane lifetime	-Low cell voltage and low current density -Fuel efficiency -Methanol/alcohol crossover	(Achmad <i>et al.</i> , 2011)

5. Components of catalyst formation

5.1 Active agent

Active agent is a substance that changes the speed for a chemical reaction to take place without taking part in the reaction itself. It causes a reduction in the free energy of the transition complex. It is usually made of transition metal and/or its oxides, sulfides, carbides, nitrides and semiconductors (e.g. Pt, Pd, Ni, Ru, Ir and Rh etc.). Most of catalysts for normal direct alcohol fuel cells are Pt but for in direct ethanol fuel cells in alkali media Pd is usually replaced (An *et al.*, 2013b; An *et al.*, 2013a; Cai *et al.*, 2013; Castro *et al.*, 2012; Jin *et al.*, 2012; Liu *et al.*, 2009; Merino-Jimenez *et al.*, 2014; Modibedi *et al.*, 2011; Neto *et al.*, 2011; Nie *et al.*, 2007; Qi *et al.*, 2011; Tarasevich *et al.*, 2009; Wang *et al.*, 2008; Xu *et al.*, 2010).

5.2 Promoter

Promoter is a substance that provides good activity, selectivity or stability when added in small amounts into the catalyst. It can be divided into 2 types:

5.2.1 Textural promoter: it is used to facilitate the good dispersion of catalyst, to reduce the formation of large particle, to prevent the loss of active site during the reaction by sintering, and to increase thermal stability of catalyst.

5.2.2 Chemical promoter: it is used to enhance activity, selectivity and stability of catalyst by preventing the poisoning on the catalyst surface.

5.3 Carbon supports

According to literature of Serp and Figueiredo (2009) (Serp and Figueiredo, 2009), The ideal characteristics of carbon supports are well support of catalyst deposition and well dispersion of active metal catalyst in nanoscale. It is needed to find the suitable support for catalyst preparation. It can be divided as followed:

5.3.1 Carbon blacks, the most widely used as supports for PEMFCs and DAFCs are carbon soot or carbon blacks. Carbon blacks are obtained from pyrolysis or incomplete combustion of carbon compounds. The ways to produce are furnace, channel, thermal, and lamp blacks. The physical properties for carbon blacks were detailed in Table 2. The average size of primary particle investigated by high-resolution TEM was ranging from 10-50 nm. The absorptive capacity of carbon black for liquid (dibutyl phthalate, DBP) related to the aggregate shape between primary particle and graphite layer. The DBP absorption is varying between 0.3 and 4 cm³ g⁻¹. High and low DBP values represent high and low structure, respectively. The BET surface area (S_{BET}) is in the range to 10-1500 m² g⁻¹ depending on the method to produce carbon blacks. The types of carbon blacks such as acetylene black, Vulcan XC-72R, and Ketjenblack have been widely developed in PEMFCs and DAFCs (McBreen *et al.*, 1981; Uchida *et al.*, 1995).

Table 2 The characterization of carbon blacks.

	Property	Acetylene Black	Vulcan XC-72R	Ketjenblack DJ-600	Black Pearls 2000
Textural characteristics	BET surface area (m ² g ⁻¹)	64	252	1300	1500
	Area of mesopores (m ² g ⁻¹)	64	177	1230	1020
	Total pore volume (cm ³ g ⁻¹)	0.20	0.63	2.68	2.56
	Average pore diameter (nm)	14.4	15.9	9.45	20.6
Morphology	Primary particle diameter (nm)	42	20-30	35-40	10-15

Source: Serp and Figueiredo (2009)

5.3.2 Carbon nanotubes and nanofibers is carbon which has tubular structure of their filament that makes them unique among various forms of carbon. Carbon filaments are formed by thermal decomposition of gaseous hydrocarbons which was first discovered in 1989. The carbon filaments consist 2 main types such as carbon nanotubes (CNTs) and carbon nanofibers (CNFs). CNTs can be divided into 2 categories: single-walled and multi-walled carbon nanotubes (SWCNTs and MWCNTs). The wide variability of the CNFs and CNTs structures, mesoporosity and high degree of ordered (crystalline) structure makes them very attractive for catalyst supports. The characteristics of CNTs and CNFs are shown in Table 3 (Bessel *et al.*, 2001; Li *et al.*, 2002; Maiyalagan *et al.*, 2005).

Table 3 The characterization of CNTs and CNFs.

Property	SWCNTs	MWCNTs	CNFs
Diameter (nm)	0.5-2 ($D_{ave}=1-1.5$)	5-200 ($D_{ave}=10-40$)	10-500 ($D_{ave}=50-100$)
Length	Few μm up to 20 cm	Few μm to hundreds μm	Few μm to hundreds μm
Apparent density (g cm^{-3})	0.5-1(film)	0.02-0.3	0.3-1.4
S_{BET} ($\text{m}^2 \text{g}^{-1}$)	400-900	150-450	10-250
Pore diameter (nm)		5-50	
Porosity (cm^3/g)	Microporous $V_{micro} : 0.15-0.3$	Mesoporous $V_{meso} : 0.5-0.2$	Mesoporous $V_{meso} : 0.2-2$
Young's modulus (TPa)	1.05-1.3	0.5-1.2	0.3-0.7
Tensile strength (GPa)	45-150	3-30 to 150	3-12
Electrical resistivity ($\Omega \text{ cm}$)	6×10^{-4}	$0.6 - 2 \times 10^{-4}$	1.5-3
Electrical conductivity (S cm^{-1})	550	80-1000	300

Source: Serp and Figueiredo (2009)

5.3.3 Active or activated carbons can be produced from pyrolysis process of various vegetative residues, for example, wood chip, peat, coal, nutshells, pits at high temperature about 773 to 1273 K. Activated carbons have high BET surface area of about 400 to 2500 m² g⁻¹ and micro volume of up to 1.2 cm³ g⁻¹ which was usually used as adsorbents (de Miguel *et al.*, 2002; Huang *et al.*, 2008a). They also have been used in heterogeneous catalysts and sometimes have been used as electrocatalysts.

5.4.4 Carbon of the Sibunit family is considered as a composite material which consists of 2 main carbons: carbon blacks and pyrolytic carbon. They were produced by pyrolysis of hydrocarbons containing propane and butane. Sibunit carbons are similar to graphite which have high mechanical stiffness of up to 300 kg cm⁻², electron conductivity of about 10 S cm⁻¹, high thermal stability, very low ash content (below 0.3 wt%) and high concentration of surface functional groups. They have high crystallinity, high surface area of up to 500 m² g⁻¹ and pore volume of 1.0 m³ g⁻¹. Sibunit carbons have been used as catalyst for phosgene synthesis and liquid-phase oxidation of sulfur-containing substance and as support for heterogeneous catalysts. Recently, Sibunit carbons have also shown promising properties for using as supports for fuel cell electrocatalysts (Gribov *et al.*, 2012; Rao *et al.*, 2005).

5.3.5 Ordered mesoporous carbons are synthesized either by nanocasting ordered mesoporous silica or zeolite template, or synthesized directly by templating triblock copolymer structure-directing species. The resulting materials have uniform mesoporous structure of periodically arranged interconnected mesopores with BET surface area of 400 to 1000 m² g⁻¹ and pore volume from 0.7 to 3.8 cm³ g⁻¹. Their structures are strongly affected by nature of carbon precursors and the conditions applied during the polymerization and pyrolysis steps. This type of carbon was used as a support for electrocatalytic reaction in fuel cells (Chang *et al.*, 2007; Jun *et al.*, 2000). The advantage of this carbon is its core and graphitic carbon shell that can increase the durability of fuel cells.

5.3.6 Carbon aerogels were first synthesized by Pekala in 1989 through pyrolysis of organic aerogels. They display 3D random close-packed monolithic

structure of slightly overlapping carbon sphere (3 to 30 nm) with small interstitial pores (< 50 nm) connected to each other by covalent bonds. This structure shows unique physical properties, such as high conductivity (1 to 15 S cm⁻¹), high mesoporosity and high surface area. The carbon aerogels is usually used in fuel cell which is believed that the monolithic and tunable structures of carbon aerogels help enabling better control of carbon layer morphology (Fung *et al.*, 1995; Moreno-Castilla and Maldonado-Hódar, 2005).

6. Preparation of carbon- supported electrocatalysts

According to literature of Serp and Figueiredo (2009) (Serp and Figueiredo, 2009), Noble metal such as Pt, Pd, Ru, Au etc., is normally used with carbon support for low temperature fuel cells (such as DAFCs and PEMFCs). In order to reduce cost, some research study utilized non-noble metal catalysts such as Ni-based catalyst instead of these noble metals. The catalyst composition can up to contain 20-80 wt% metal but in contrast the conventional catalyst loading is usually below 1-5 wt%. Good catalyst preparation is one of the key factors to yield well-dispersed and distributed nanoparticles of electrocatalyst for use in fuel cells. Several methods of catalyst preparation for low temperature fuel cell applications are listed as follows:

6.1 Impregnation method

The aim of impregnation process is to increase the amount of catalyst nanoparticles deposited on support. It is common technique for the synthesis. Normally, the metal precursor complexes (e.g., PdCl₂, H₂PtCl₆, RuNO(NO₃)_x) are dissolved in an aqueous or organic solution. Then the carbon is added to the metal-containing solution followed by solvent evaporation, drying, calcination and simple reduction. The desired characteristics of catalyst obtained from impregnation method depend on solubility of precursor complexes, drying conditions, pore structure and the surface properties of carbon support. Most widely used impregnation method was impregnation-reduction of active components on the carbon support. The reaction can be under (1) the strong reducing agents (Na₂S₂O₄, N₂H₄, HCOOH, NaBH₄), (2) alkali

agents (e.g. NaOH, KOH) followed by the reduction reaction and (3) an alkali reducing agent simultaneously (e.g. NaOH + H₂CO, NaOH + ethylene glycol, NaCO₃ + NaOOH). The resulting catalyst obtained from impregnation-reduction method is affected by the temperature, pH and the nature and concentration of the reductants (Neto *et al.*, 2011; Nie *et al.*, 2007; Rao and Viswanathan, 2010).

6.2 Colloid synthesis method

In this technique, a metal precursor is reduced by chemical or electrochemical technique. The growth of metal nanoparticles in the well-dispersed colloidal solution is limited by a surfactant adsorbed at the metal solution interface which helps minimize fraction of agglomerated particle. If the surfactant is a polymer or an organic compound, the removal of the protective shell is the key step affecting the electrocatalyst activity. The metal particles are adsorbed in the pore by the interaction between pore wall and the metal particles that are stronger than the interaction with plane surfaces. After adsorption step the thermal and/or oxidative treatment is required for the surfactant degradation. This step can be cause metal agglomeration. The size of colloidal particle can be controlled by varying (Huang *et al.*, 2008b).

6.3 Electrodeposition method

In the electrodecomposition method, the metal can be deposited directly onto the carbon support from a solution containing metal species. The nature of the electrolyte and the current-potential programmed are the parameters which limit the mean particle size and the size distribution. Pulsed electrochemical deposition has proven to be useful for independent control of nucleation and growth steps. This method can be used for the deposition of metal fraction up to 40 wt%. The drawbacks of this technique include the waste of unreduced metal, the poisoning of catalyst from the presence of counter ions (usually Cl), and the hydrogen evolution reaction subsequently causing the loss of faradic yield (Ahn *et al.*, 2012; Lu *et al.*, 2009).

6.4 Other methods

Other methods are such as water-in-oil microemulsions. In this method, the particle preparation consists two microemulsions containing appropriate reactants (metal salt and reducing agent) to yield desired metal particles. The reaction takes place during the collisions between water droplets and particles and it is controlled by the size of droplets (Rao and Viswanathan, 2010). Other methods include sonochemical that is the application of ultrasound to chemical reactions and processes. The mechanism causing sonochemical effects in liquids is the phenomenon of acoustic cavitation and radiation-chemical that is the electron beam irradiation method from an aqueous solution containing of precursors and support powder dispersed in it.

7. Functionalization of carbon support

In general there are two types of functionalization of carbon support: covalent and non-covalent functionalization (Meng *et al.*, 2009). Covalent functionalization is based on the formation of a covalent bond between functional entities and the carbon structure using a strong acid. It can be divided into direct covalent sidewall functionalization and indirect covalent functionalization with carboxylic groups on its surface. Direct covalent sidewall functionalization is associated with a change in hybridization from sp^2 to sp^3 and a simultaneous loss of conjugation. Indirect covalent functionalization takes advantage of chemical transformations of carboxylic groups at the open ends and holes in the sidewalls. These carboxylic groups might have existed on the as-grown carbon support and can be further generated during oxidative purification. The drawback of covalent functionalization is that the perfect structure of support has to be destroyed, resulting in significant changes in their physical properties. Non-covalent functionalization is mainly based on supramolecular complexation using various adsorption forces, such as Van der Waals force, hydrogen bonds, electrostatic force and π -stacking interactions. Compared to the chemical functionalization, non-covalent functionalization has an advantage that it can be

operated under relatively mild reaction conditions while the perfect graphitic structure of carbon support could be maintained.

8. Cyclic voltammetry

Cyclic voltammetry (CV) is an electrochemical technique used to measure the current generated in an electrochemical cell under conditions where potential is in excess of that predicted by the Nernst equation. CV is performed by cycling the potential of a working electrode, and measuring the resulting current. The potential of the working electrode is measured against a reference electrode which is maintained as a constant applied potential. The resulting applied potential produces an excitation signal as shown in Figure 3. In the forward scan, the potential is initially scanned negatively, starting from a higher potential (a) towards a lower potential (d). The potential extreme (d) is called the switching potential where the potential is high enough to cause an oxidation or a reduction of the catalyst. The reverse scan occurs from (d) to (g) where the potential is scanned positively. Figure 3 shows a typical reduction occurring from (a) to (d) and an oxidation occurring from (d) to (g). It is important to note that some analysts obtain oxidation peak first when the potential is initially scanned positively. This cycle can be repeated and the scan rate can be varied. The slope of the excitation signal represents the scan rate used.

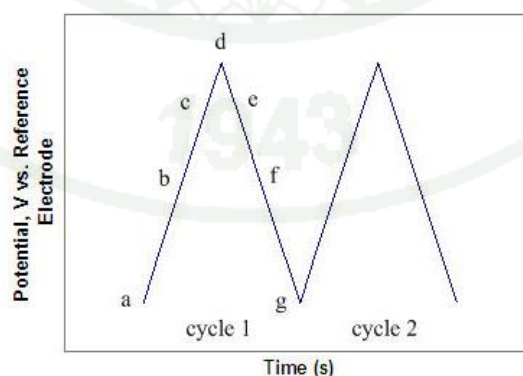


Figure 3 CV excitation signal.

Source: Douglas *et al.* (2007)

A cyclic voltammogram is obtained by measuring the current at the working electrode during the potential scans (Douglas A. *et al.*, 2007). Figure 4 shows a cyclic voltammogram resulting from a single electron reduction and oxidation according to the following reversible reaction equation (4)

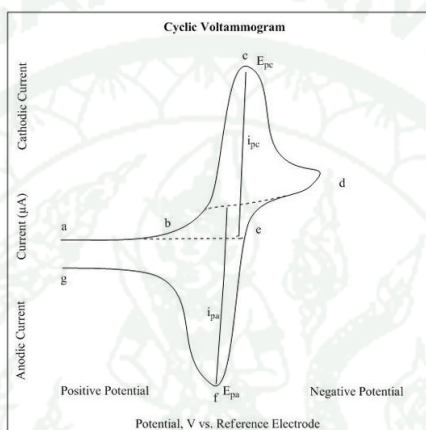
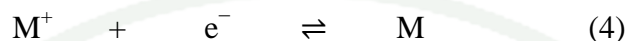


Figure 4 A cyclic voltammogram of single electron oxidation-reduction reaction.

Source: Douglas *et al.* (2007)

In Figure 4, the reduction process starts from (a) the initial potential to (d) the switching potential. In this region the potential is scanned negatively to cause a reduction process. The resulting current is called cathodic current (i_{pc}). The corresponding peak potential occurs at (c), and is called the cathodic peak potential (E_{pc}). The E_{pc} is obtained when the electrode surface is completely reduced. After the switching potential is reached (d), the potential is scanned positively from (d) to (g). This results in anodic current (i_{pa}) produced from oxidation reaction. The peak potential at (f) is called the anodic peak potential (E_{pa}) where electrode surface is oxidized (Kissinger and Heineman, 1983). The equations for reversible systems are listed in Appendix H.

9. Chronoamperometry

Chronoamperometry (CA) is an electrochemical technique in which the potential of the working electrode is stepped and the resulting current from faradic processes occurring at the electrode is monitored as a function of time. The identity of the electrolyzed species can be obtained from the ratio of the peak oxidation current versus the peak reduction current. However, chronoamperometry generates high charging currents which decay exponentially with time. The Faradaic current generated from electron transfer processes, is the major component of the decays as described in the Cottrell equation as shown in equation (5). In most electrochemical cells this decay is much slower than the charging decay cells in three electrode system. Since the current is integrated over relatively longer time intervals, chronoamperometry gives a better signal to noise ratio in comparison to other amperometric techniques. The analysis of chronoamperometry (CA) data is based on the Cottrell equation, which defines the current-time dependence for linear diffusion control (Anonymous, 2007; Bard and Faulkner, 2000; Peter and William R., 1996):

$$i = nFACD^{-0.5} \pi^{-0.5} t^{-0.5} \quad (5)$$

where

- n = number of electrons transferred/molecule
- F = Faraday's constant (96,500 C mol⁻¹)
- A = electrode area (cm²)
- D = diffusion coefficient (cm² s⁻¹)
- C = concentration of solution (mol cm⁻³)
- i = current density (A cm⁻²)

10. X-ray diffraction technique

X-ray diffraction is a unique method in determination of crystallinity of a compound. XRD is primarily used for identification of crystalline material and different polymorphic forms, distinguishing between amorphous and crystalline material and quantification of the percent crystallinity of a sample.

From the XRD result, can be used to calculate the parameter such as the crystalline size, lattice parameter and d-spacing

The d-spacing is calculated from Bragg's law as shown in equation (6):

$$\lambda = 2d \sin \theta \quad (6)$$

where λ is the wavelength of Cu/K α (1.54056 Å)
 θ is diffraction angle of the reflection (degree)
 d is d-spacing (nm)

The Bragg's Law is derived to Scherrer equation for calculation of the crystalline size as shown in equation (7):

$$L = \frac{K\lambda}{\beta \cos \theta} \quad (7)$$

where L is crystallite size (Å)
 K is crystallite-shape factor = 0.9
 λ is the wavelength of Cu/K α (1.54056 Å)
 θ is observed peak angle (degree)
 β is X-ray diffraction broadening, (radian)

The β is determined from equation (8):

$$\beta = \sqrt{B_M^2 - B_S^2} \quad (8)$$

where B_M is the measured peak width at half peak height (radian)
 B_S is beak broadening due to the machine (radian)

The lattice parameter of Pd (2 2 0) FCC can be calculated from equation (9) which is a relationship between d-spacing and hkl.

$$d_{hkl} = \left[\frac{1}{a^2} (h^2 + k^2 + l^2) \right]^{-1/2} \quad (9)$$

where d_{hkl} is d-spacing of the plane (nm)
 $(h k l)$ is the number of each dimension of plane
 a is lattice parameter of FCC

11. Chemisorption technique

Chemisorption is a kind of adsorption which involves a chemical reaction between the surface and the adsorbate. For Pt and Pd based catalysts used CO adsorbed on the metal surface to investigate number of active sites and metal dispersion.

The metal dispersion was calculated using equation (10)-(14). Equation (10) presents the amount of adsorption per unit (amount of adsorption per 1g of sample), $V_m / \text{cm}^3 \text{ g}^{-1}$:

$$V_m = V_{COchem} \cdot m \quad (10)$$

where V_{COchem} is amount of CO adsorption / cm^3
 m is sample weight / g

The volume of CO adsorption (V_{COchem}) can be calculated by equation (11):

$$V_{COchem} = V_{pulse} \left(n - \sum_i^n \frac{S_i}{S_{max}} \right) \quad (11)$$

where n is the number of pulse injected
 V_{pulse} is the CO pulse volume / cm^3
 S_i is the peak area for each pulse / count
 S_{max} is the peak area of non-adsorbed pulse / count

Metal dispersion (percentage of metal surface exposed) (D_m / %) can be calculated by equation (12) as followed:

$$D_m = \frac{V_{COchem} \cdot SF \cdot MW}{22414 \cdot c} \times 100 \quad (12)$$

where MW is atomic weight of metal / g mol^{-1}
 SF is stoichiometry factor (Pd:CO = 1)
 c is weight of metal loading on support / g

Metal weight (c / g) which is defined as weight of metal loading on support) can be calculated by equation (13) as followed:

$$c = m \times \frac{p}{100} \quad (13)$$

where p is weight percentage of metal content / % wt

Number of active site N_s can be calculated by equation (14) as followed:

$$N_s = \frac{V_m \cdot N_A \cdot SF}{22414} \quad (14)$$

where N_A is Avogadro's number (6.02×10^{23} atoms)

12. CO tolerance

In the CO stripping process, the reactions of CO oxidation are shown in the following equations:



Where, the MtO_x is metal oxide. The reactions that enhance CO tolerance mechanism of Pd catalyst are schematically demonstrated in Figure 5 (Aranda and Schmal, 1997; Marques *et al.*, 2006).

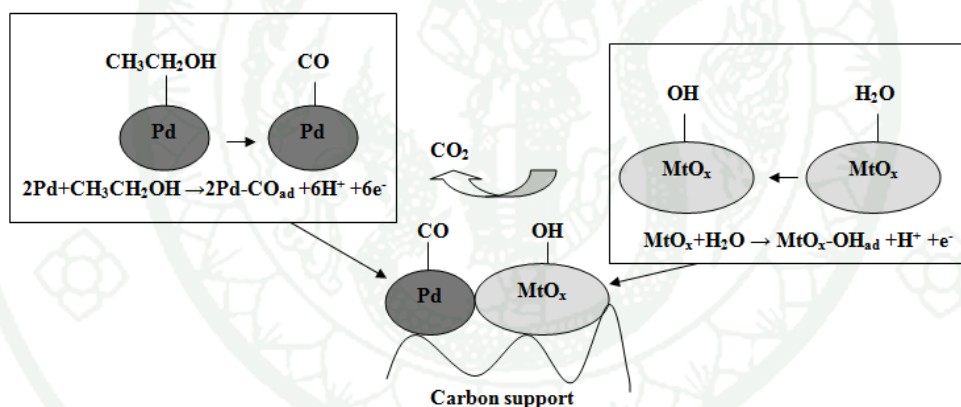


Figure 5 The mechanism of Pd catalyst with MtO_x promoter.

The reduction reaction of the Pd oxide to Pd can be used to calculate the charge (Q_s) by integrating the area under the peak and finding the real electrochemical surface area (ESA) of Pd. The ESA equation is shown in equation (18).

$$\text{ESA} = \frac{Q_s}{m \cdot Q_{th}} \quad (18)$$

where Q_s is the charge of electron from area under the peak (mC cm^{-2})

- m is the weight of Pd on the electrode (Pd loading = 0.0952 mg cm⁻²)
- Q_{th} is the charge of the reduction reaction of Pd oxide in theory (0.405 mC cm⁻²)

Literature review

Shen *et al.* (2010) synthesized PdNi catalysts by varying atomic ratio of Pd:Ni when fixed Pd at 20% wt loading. The Pd:Ni atomic ratios were Pd₁Ni₁/C, Pd₂Ni₃/C, Pd₁Ni₂/C and Pd₂Ni₅/C. The preparation method was sodium borohydride (NaBH₄) reduction method. The first step was dissolving precursors in DI water until homogeneous. The carbon blacks were then added the into precursor solution and stirred until homogenous suspension was obtained. After that 2 wt% NaBH₄ was added. Finally, the catalysts were precipitated, followed by filtration to separate solid and liquid. The wet solid was washed several times and was dried in air at 70°C. The transmission electron microscopy image showed a good dispersion and the particle size was in nano-size. The X-ray photoelectron spectroscopy result also showed that Ni in form consist of Ni, NiO, NiOOH and Ni(OH)₂ as shown in Figure 6. The nickel hydroxide (Ni(OH)₂) was the main component of Ni reduced by NaBH₄ reduction method which helped promoting electro oxidation reaction as shown in equation (19).



The cyclic voltammetry results showed that the Pd₂Ni₃ yielded the highest ethanol oxidation and the current density of about 217 mA cm⁻² in 1 M KOH and Ethanol solution. The chronopotentiometric constant current density of about 20 mA cm⁻² was detected after 12 hr. The Pd₂Ni₃/C catalyst was more stable than Pd/C catalyst. The Pd₂Ni₃/C catalyst showed power density of about 90 mW cm⁻² by in a single cell operating at 60°C using 3.0 M ethanol fuel and 5 M KOH (Shen *et al.*, 2010).

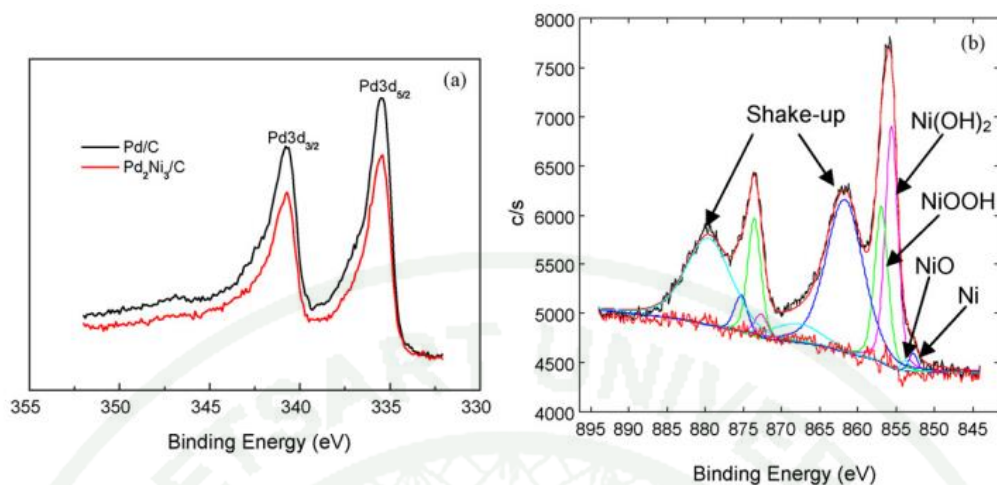


Figure 6 XPS spectra of (a) Pd₂Ni₃/C (b) Ni 2p XPS spectrum of Pd₂Ni₃/C.

Source: Shen *et al.* (2010)

Modibedi *et al.* (2011) studied Pd–Sn and Pd–Ru–Sn catalysts using 2 synthesis methods (Figure 7). Both methods were co-reduction method but they were different in the addition step for Pd precursor. The co-reduction agents were sodium borohydride and ethylene glycol. In the first method, all precursors were added at the beginning of the synthesis followed by co-reduction at the temperature of 80 °C. In the second method Ru–Sn was synthesized by co-reduction at 80 °C to obtain catalyst powder. It was then co-reduced again at room temperature. The CV results showed that higher ethanol oxidation in a mixture of 0.5 M NaOH and ethanol solution was obtained in the second method (reduction Pd after Ru+Sn) when compared to the first method. The results showed that Pd–Sn and Pd–Ru–Sn catalysts were more active to ethanol oxidation than that of Pd/C and Pt–Ru/C (E-tek). In addition, the Pd–Sn binary catalyst showed higher CO tolerance than that of the ternary catalyst. The concentrations of ethanol were also varied. It was found that 3 M ethanol can adsorb ethoxy (CH₃CO_{ads}) better than other concentrations (Modibedi *et al.*, 2011).

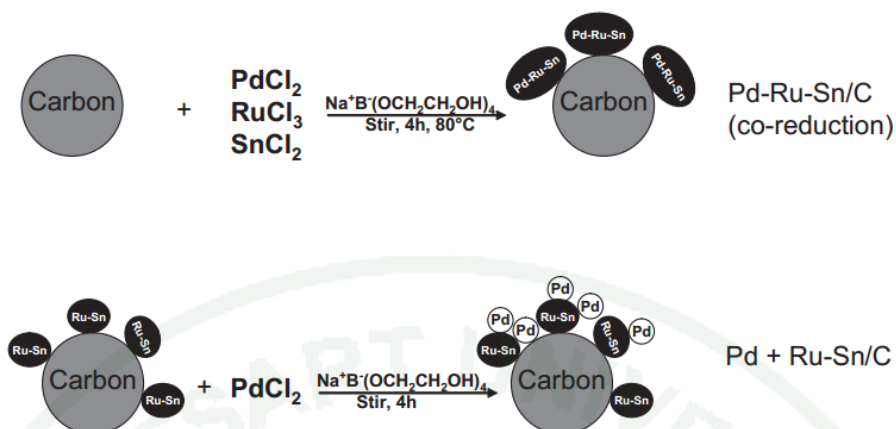


Figure 7 Different synthesis pathways for co-reduction process.

Source: Modibedi et al. (2011)

Ramulifho *et al.* (2012) prepared Pd, PdNi and PdSn catalysts on sulfonated multi-walled carbon nanotubes (SF-MWCNTs) by rapid microwave-assisted solvothermal method as shown in Figure 8. The catalyst support was initially treated with acid via 2 steps and then dried overnight. The ethylene glycol (EG) was used to prepare a precursor solution with the adjusted pH at 7.4 by using KOH. The SF-MWCNTs were added into the resulting solution and sonicated for 1 hr. The solution was transferred to liner-rotor 16 F100 TFM vessel and heated in microwave at 1000 W 170°C for 60 s 13 times. After that, the reduction process was finished. The catalyst was cooled down and washed with acetone and DI water. Finally, it was heated to remove water and acetone at 110°C overnight in oven. The electrochemistry result showed that the PdNi catalyst toward ethanol oxidation in alkaline media was more active than the PdSn catalyst. The mechanisms of ethanol reaction on Pd catalyst in alkaline media are shown in the following equations:

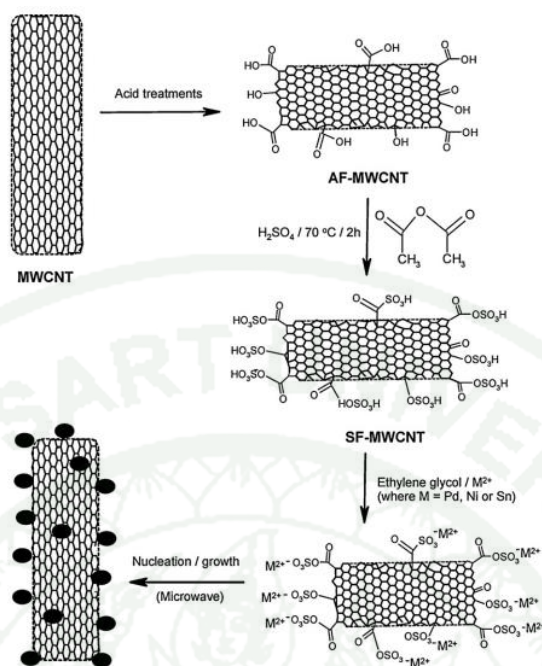


Figure 8 The treatment of MWCNTs with acid and followed by rapid microwave-assisted solvothermal.

Source: Ramulifho *et al.* (2012)



Equation (21) and (22) explain the adsorption of ethanol on catalyst surface. Equation (24) is the rate determination step where the oxidation reaction depends on the $\text{CH}_3\text{CO}_{\text{ads}}$ and OH_{ads} adsorption on catalyst surface (Ramulifho *et al.*, 2012).

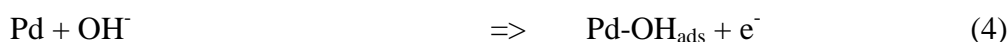
Note: \rightleftharpoons is refer to reversible reaction and \Rightarrow is refer to irreversible reaction.

Rao and Viswanathan (2010) synthesized Pd-Co-Mo on carbon black (CDX975) by hydrazine reduction in reverse microemulsion method (REM). The microemulsion was prepared by mixing 10% surfactant (Tioton-X-100) with 35% cyclohexane, 40% popanol-2 and 15% aqueous phase by volume. The excess amount of hydrazine was added to the precursor solution and the mixture was then turned into microemulsion. It was mixed in ultrasonic bath for 2 hrs. The reactions are as follow:

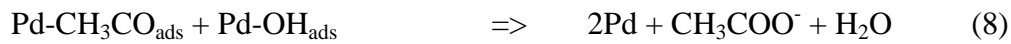


Carbon black was added into the solution and then stirred for 2 hr. After that the suspended solution was filtrated and washed with acetone and DI water, respectively. The wet solid was dried in an oven at 348 K for 2 hr. Finally heat treatment at 973, 1073 and 1173 K in 10 % H₂-90% Ar for 1 hr was required. It was found that the catalyst which was thermally heated at 973 K showed the highest activity for oxygen reduction reaction (ORR). Moreover all resulting catalyst exhibited good durability to ethanol (Rao and Viswanathan, 2010).

Yi *et al.* (2011) synthesized the porous Pd particles by using hydrothermal method using different reducing agents such as PEG, PEG-EDTA, HCHO-EDTA, EG, and HCHO. The titanium sheet was first added into autoclave together a mixture of precursor and reduction agents. Then it was heated for 10 hr at 180 °C and was air cooled to room temperature. Finally the porous Pd was dried in air at 100°C for 30 min. The maximum current density of the porous Pd-HCHO-EDTA for EOR in alkaline media was about 151 mA cm⁻². The reactions are as follow (Yi *et al.*, 2011):



The EtOH+ NaOH can adsorb on Pd surface as follow:



An and Zhao (2011) studied about direct ethanol fuel cell in alkaline media by comparing with anion exchange membrane (AEM) and cation exchange membrane (CEM) as seen in Figure 9. They demonstrated only the reaction in AEM-DEFC as shown in equations. Moreover, the result of single cell performance test at an operating temperature as high as 90 °C, the CEM-DEFC can stably discharge with a high power density (An and Zhao, 2011).

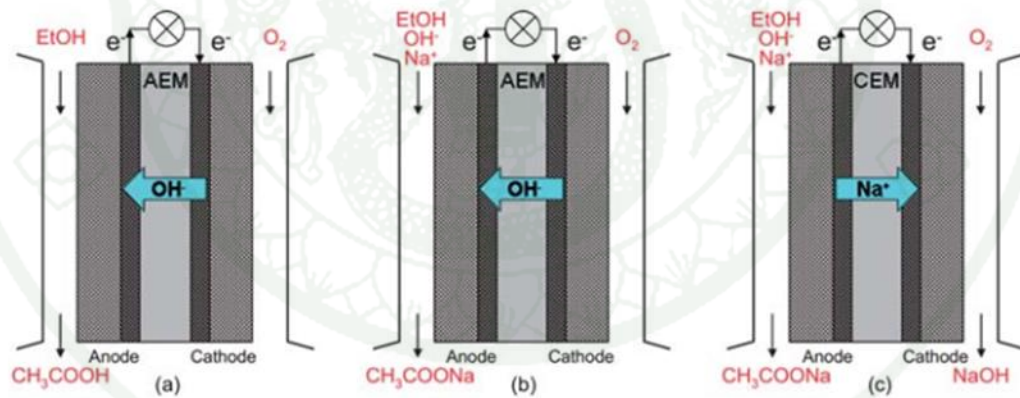
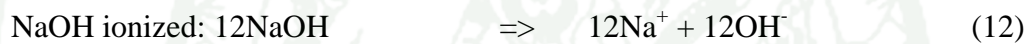
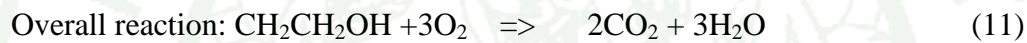
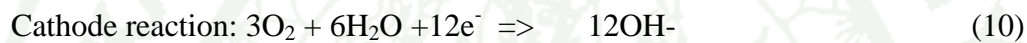
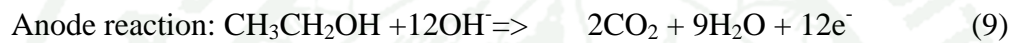


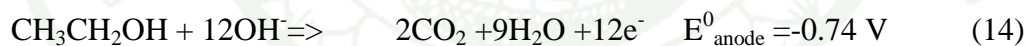
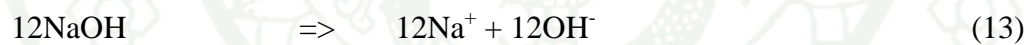
Figure 9 Schematic of anion and cation exchange membrane direct ethanol fuel cells.

Source: An and Zhao (2011)

An and Zhao (2011) studied the performance of direct ethanol fuel cell in alkaline-acid (DEFC-AA using ethanol+NaOH solution as the anode feed and $\text{H}_2\text{O}_2 + \text{H}_2\text{SO}_4$ solution as the cathode feed. The anode electrocatalyst (PdNi/C) was homemade with the loading of 1.0 mg cm^{-2} whereas the cathode catalyst was 60%Pt

(commercial) on nickel foam. (An and Zhao, 2011). An *et al.* (2011) studied the theoretical voltage of a new type of DEFC. Figure 13a (blue chart) is a conventional PEM-DEFC (anode feed ethanol solution and cathode feed O₂) while Figure 13a (green chart) is AEM-DEFC (anode feed ethanol + NaOH solution and cathode feed O₂). Both system produced equal of E⁰_{cell} of 1.14 V but the kinetics for both EOR and ORR in the alkaline media (AEM-DEFC) was faster than PEM-DEFC. In Figure 13b, the cathode feed was changed to H₂O₂ but the anode feed was unchanged. In this case, E⁰_{cell} of AEM-DEFC was lower than that of PEM-DEFC and E_{cathode} of PEM-DEFC was higher than that of AEM-DEFC. Figure 13c combined these 2 systems in Figure 13b; the E⁰_{cell} was up to 2.52 V. The reactions of new fuel cell system are shown below. NaOH is ionized to sodium ions and hydroxyl ions. The hydroxyl ions react with ethanol and are converted to carbon dioxide, water and electrons. The electrons pass through load and Na⁺ migrates through a cation membrane to cathode. The hydrogen peroxide receives electrons and is converted to water and Na⁺ reacts with SO²⁻₄ and is converted to Na₂SO₄ (E⁰_{cell} = 2.52 V) (An *et al.*, 2011b)

Anode reaction



Cathode reaction



Over all reaction



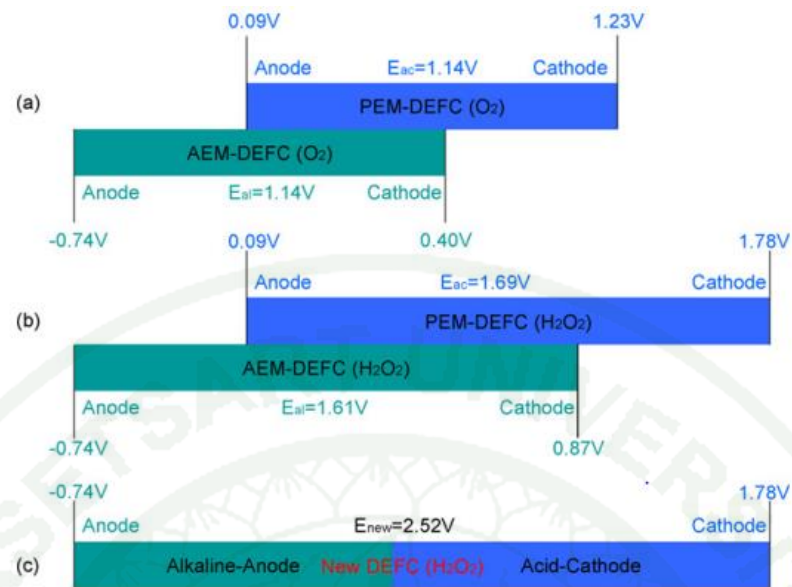


Figure 10 Different DEFC systems.

Source: An *et al.* (2011)

MATERIALS AND METHODS

Materials

All materials and instruments in this work are summarized in Table 4.

Table 4 Summary of all materials and instruments.

No.	Chemical/Instrument name	Purchased from	Grade/model
1	Palladium (II) chloride anhydrate, 59% Pd (PdCl ₂)	Merck	Synthesis
2	Nickel (II) chloride anhydrate (NiCl ₂)	Merck	Synthesis
3	Tin (II) chloride anhydrate (SnCl ₂)	Merck	Synthesis
4	Sodium borohydride (NaBH ₄)	HIMEDIA	Analytical reagent
5	Carbon black (CB)	Carbot	Vulcan XC-72R
6	Multi-walled carbon nanotubes (MWCNT) diameter 10-30 nm and length 5-15 μm	Nanostructure & Amorphous Materials	
7	95-97 % Sulfuric (H ₂ SO ₄)	Merck	Analytical reagent
8	69.0-70.0 % Nitric acid (HNO ₃)	J.T.Backer	Analytical reagent
9	Potassium hydroxide (KOH)	Ajex Finechem	Analytical reagent
10	Absolute ethanol (C ₂ H ₅ OH)	ACI Labscan	Analytical reagent
11	5% Nafion [®] 117 solution	Sigma-Aldrich	
12	99.99 % Nitrogen gas	TIG	Commercial
13	1 % Carbonmonoxide in nitrogen gas	TIG	Commercial
14	Potassium chloride (KCl)	Ajex Finechem	Analytical reagent
15	Centrifuge	HETTICH	Universal 320

Table 4 (Continued).

No.	Chemical/Instrument name	Purchased from	Grade/Model
15	Cellulose nitrate filter paper $\phi = 0.45 \mu\text{m}$	Whatman [®]	
16	Ultrasonic bath	Elmasonic	E30 H
17	Oven	Binder	redLINE
18	Vacuum pump	SPARMAX	TC-501v
19	Ag/AgCl in 3 M KCl reference electrode	MetrohmAutolab	6.0726.107
20	Platinum counter electrode rod	Metrohm Autolab	6.1248.000
21	5-neck flask		
22	Aluminum tape		
23	Glassy carbon paper	Fuel cell store	Toray H-60
24	Bubbling tube		
25	Potentiostat-galvanostat	Metrohm Autolab	PGSTAT100

Methods

1. Catalyst preparation

The catalyst preparation used in this work was based on the sodium borohydride reduction method which is a simple and versatile method. The metal precursors were PdCl₂, NiCl₂ and SnCl₂. Those metal precursors were impregnated on Vulcan XC-72R carbon black. Several compositions of metal precursors (as detailed in Table 5) were prepared using 80 ml DI water and were then homogenized at the speed of 750 rpm for 30 min at room temperature. It is noted that the calculation for catalyst preparation is detailed in Appendix A. 1 g of Vulcan XC-72R carbon black was added into the precursor solution and then suspended by sonication for 5 min. And then 20 ml of 0.12 M sodium borohydride reducing agent was prepared. at room temperature. After sonication, the colloid was homogenized for another 6 hr while the NaBH₄ aqueous solution was slowly added to the solution, drop by drop, to avoid a

violent reaction caused by the strong reducing agent. The colloidal catalyst was washed and separated using a centrifuge at the speed of 9000 rpm. The process was carried out repeatedly until pH 7 was achieved. The solid particles were dried in an oven at atmospheric pressure and temperature of 70 °C for 20 hr. Finally, the resulting catalyst was ground to a fine powder in a mortar and then kept in a vial sealed with parafilm. Finally they were stored in a desiccator (Shen *et al.*, 2010).

Table 5 The details of metal compositions synthesized in this research work along with their abbreviations.

Abbreviation	Catalyst composition (% wt)			
	Pd	Ni	Sn	CB
20%Pd/CB	20	-	-	80
20%Pd20%Ni/CB	20	20	-	60
20%Pd20%Sn/CB	20	-	20	60
20%Pd5%Ni15%Sn/CB	20	15	5	60
20%Pd10%Ni10%Sn/CB	20	10	10	60
20%Pd15%Ni5%Sn/CB	20	5	15	60

After the evaluation of catalyst compositions, the composition which showed the maximum current density for EOR was selected to be deposited on different carbon-based supports including Vulcan XC-72R carbon black support and multi-walled carbon nanotubes support with and without functionalization. The catalyst preparation method was similar to the details given in previous paragraph. The functionalization was detailed in the next section

2. Functionalization of carbon-based supports

First, 1 g of Vulcan XC-72R carbon black powder or multi-walled carbon nanotubes was dispersed in 50 ml of a mixed concentrated H₂SO₄:HNO₃ (3:1 volume ratio) solution in a closed vessel under sonication at room temperature for 2 hr. The reaction was left undisturbed for another 15 hr. And then the suspension was washed

with deionized water until the effluent had a pH of 4-5. Finally, the catalyst support was dried in a convection oven at 100°C overnight (Osorio *et al.*, 2008).

3. Characterizations

3.1 Electrochemical characterizations

The preparation of electrode materials for all electrochemical test are described as follows: 5 mg of the synthesized catalyst was weighted in a 20 ml vial. 50 μ l of 5% Nafion[®] 117 solution and 1 ml of 5 M ethanol were then added into the 20 ml vial. The lid was put on tightly and sealed with parafilm before putting the vial in an ultrasonic bath. After that it was sonicated for 1 hr to obtain a homogeneous colloid (This was so called catalyst ink).

The further step was the coating of catalyst ink on electrode surface. The glassy carbon paper was cut into 1.5 \times 2 cm² rectangular shape with a confined exposed area using an invisible tape. The exposed areas were 0.28 mm² for the study of catalytic activity and catalytic durability or 0.40 mm² for the characterizations of CO tolerance and electrochemical surface area (ESA). 10 μ l of catalyst ink was dropped onto the exposed area of prepared glassy carbon paper and then was dried in a vacuum oven at 40 °C for 5-10 min. In order to ensure the homogeneous coating surface, the coating process was repeatedly carried out for 2 times (the weight of Pd was loaded on electrode of about 0.0680 mg cm⁻²) in the case of catalytic activity and durability or 4 times (the weight of Pd was loaded on electrode of about 0.0952 mg cm⁻²) in the case of CO tolerance and electrochemical surface area studied.

The electrochemical properties of various catalyst compositions were investigated using potentiostat-galvanostat to perform the following measurements: catalytic activity, catalyst durability, CO tolerance and electrochemical surface area. All methods were carried out at room temperature a three-electrode system.

3.1.1 Catalytic activity

The activity of catalysts toward oxidation and reduction reaction was tested by using CV method. A mixture of 1 M KOH and 1M ethanol electrolyte solution used was firstly prepared. Then the catalyst sample was employed as the working electrode (WE). The Ag/AgCl in 3 M KCl was connected to the reference electrode (RE) whereas the platinum electrode was connected to the counter electrode (CE). The electrolyte reservoir was closed with its lid tightly. Then, the working electrode, reference electrode, counter electrode and purge/vent gas tube were connected to all joints of the reservoir. Nitrogen gas was purged continuously for 10 min to remove dissolved oxygen. Finally, the CV measurement was exploited at the scan rate of 50 mV s⁻¹. The potential across the working and counter electrodes was scanned from -0.75 to 0.25 V.

3.1.2 Durability of catalysts

The catalyst durability was tested in a mixture of 1 M KOH and 1 M ethanol solution. The experimental step was similar to the test of catalytic activity. However, CA was employed by using an interval time > .1 s and duration for 1000 seconds at a fixed voltage of -0.3 V.

3.1.3 Electrochemical surface area of catalysts

The electrochemical surface area was tested in 1 M KOH solution. The procedure was similar to the test of catalytic activity. The scanned rate was used at 100 mV s⁻¹ and the potential across a working electrode and counter electrode was scanned from -1.2 to 0.5 V.

3.1.4 CO tolerance of catalysts

The 1 M of KOH solution was first filled into an electrolyte reservoir. The lid was close tightly. And, the working electrode, reference electrode, counter electrode

and purge and vent gas tube were connected to all joints of reservoir. Then nitrogen gas was purged into electrolyte solution for 10 min and then carbon monoxide was purged for 15 min. The CA method was employed with the duration of 300 seconds at fixed a voltage of -0.3 V.

After the CO adsorption, nitrogen was purged again to remove CO gas. For CO-stripping, the test was altered to CV method. The scan rate was set to 100 mV s^{-1} and the potential across a working electrode and counter electrode was scanned from -1.2 to 0.5 V.

3.2 Analytical techniques

3.2.1 Characterization of catalyst

1) X-ray diffraction (XRD), Philips X' pert, was used to investigate crystallization and phase of different catalyst compositions. The XRD patterns of catalysts were obtained using a Cu K_{α} source operating at 45 kV and 30 mA with a scan rate of $0.04^{\circ} \text{ s}^{-1}$.

2) Transmission electron microscopy (TEM), TEM, JEOL 2010, was used to investigate the particle size and the dispersion of metal catalysts using a LaB₆ filament at 200 kV.

3) Scanning electron microscopy (SEM) and energy dispersive X-ray spectrometer (EDX), FEI Quanta 400 & EDAX, was used to find the morphology of catalyst surface and metal loading ratio, respectively.

4) X-ray photoelectron spectroscopy (XPS), AXIS Ultra DLD, was used to investigate the forms of metal catalysts using Al monochromatic X-rays at a power of 150 W. The survey and regional spectra were obtained by passing energy of 1200 and 0 eV, respectively.

5) Chemisorption, BELCAT-B, with temperature programmed reduction (TPR) was initially used to investigate the temperature range of catalysts for hydrogen reduction with a supply of 5% H₂/Ar at 50 ml s⁻¹, at a scanned temperature of 0-650 °C. And CO-pulse method was used to investigate number of active sites and the dispersion of Pd. The co pulse steps were as follows: (i) preheated at 400 °C for 25 min, (ii) oxidized with 99.999% O₂ for 15 min, (iii) purged with He for 15 min, (iv) reduced with pure H₂ for 15 min, (v) purged with He for 15 min, (vi) cooled down to 50 °C, and (vii) injected 0.89 cm³ of 10% CO-He until the change in the peak area was less than 2%.

3.2.2 Carbon based support characterization

1) Surface area and porosity analyzer, Autosorp-I, the samples were degassed in vacuum at 300°C for 2 hr prior to the N₂ adsorption measurement. This technique was used to explore the surface area and pore size distribution of various supports.

2) Raman spectroscopy, Renishaw Raman spectroscopy system 2000, was used to investigate the effect of functionalization and the defect of carbon supports after functionalization. Raman spectra are obtained at ambient temperature with the green laser wavelength of 532 nm, and radiated from a helium neon laser at the power of 2 mW.

3) Fourier transform infrared spectroscopy (FTIR), Thermo Nicolet 6700, was used to investigate the function groups attached on functionalized supports. The sample powder was mixed with KBr and was then analyzed with a wave number of 400-4000 cm⁻¹

4) Thermogravimetric analysis (TGA), Mettler Toledo TGA/SDTA 851^c, was operated at 70-850 °C and ramp rate of 5 °C min⁻¹ under air flow in order to analyze the amount of functionalized group on the supports.

5) Scanning electron microscopy (SEM), FEI Quanta 400, was used to investigate the surface morphology of support.



RESULTS AND DISCUSSION

Results and discussion was divided into 3 parts including the evaluation of catalyst compositions, the functionalization of carbon-based supports and the evaluation of catalyst on various supports.

1. Evaluation of catalyst compositions

Various catalyst compositions were synthesized by impregnation- NaBH_4 reduction method including 20%Pd/CB, 20%Pd20%Ni/CB, 20%Pd20%Sn/CB, 20%Pd15%Ni5%Sn/CB, 20%Pd10%Ni10%Sn/CB and 20%Pd5%Ni15%Sn/CB. The physical properties of those catalysts were analyzed by XRD, SEM-EDX, TEM and chemisorption (CO pulse method). Their electrochemical properties were evaluated by electrochemical activity, durability, CO-tolerance and electrochemical surface area of catalyst.

1.1 Physical properties of various catalysts

1.1.1 X-ray diffraction

X-ray diffraction was used to investigate the bulk structure of the electrocatalysts. The XRD patterns of 20%Pd/CB, 20%Pd20%Ni/CB, 20%Pd20%Sn/CB, 20%Pd15%Ni5%Sn/CB, 20%Pd10%Ni10%Sn/CB and 20%Pd5%Ni15%Sn/CB catalysts are shown in Figure 11. The first peak was observed at around 25-30° which was (0 0 2) plane of hexagonal structure of Vulcan XC-72R carbon black (Tayal *et al.*, 2011). The characteristic peaks of Pd included five peaks at 39.901°, 46.209°, 67.618°, 81.364° and 86.342° which referred to (1 1 1), (2 0 0), (2 2 0), (3 1 1) and (2 2 2) planes, respectively. All of those peaks represented crystalline with face centered cubic (FCC) (Zhang *et al.*, 2011). The Ni content can be extracted from the characteristic peaks of Ni(OH)_2 at 33.193° and 59.303° on (1 0 0) and (1 1 0) planes, respectively (Xiao *et al.*, 2005). The Sn content can be found from the characteristic peaks of SnO_2 at 26.511°, 33.769°, 51.612° and 65.752° which referred to (1 1 0), (1

0 1), (2 1 1) and (3 0 1) planes, respectively. However, only (2 1 1) plane of SnO₂ can be distinguished from other catalyst components. The first peak at 26.511° overlapped with the carbon support peak; hence, the peak intensity was increased with the presence of SnO₂ in the electrocatalysts. The second peak of Sn at 33.769° overlapped with Ni(OH)₂ at 33.193° so the Ni(OH)₂ peak have a little shift because of the existence of Ni-Sn alloy in the catalysts (Watanabe, 2004). The last peak of SnO₂ at 65.752° was located close to the Pd peak at 67.618°. The change in the peak position of (1 1 1) plane was observed in Pd containing Ni catalysts: 20%Pd20%Ni/CB, 20%Pd15%-Ni5%Sn/CB, 20Pd10%-Ni10%Sn/CB and 20%Pd5%Ni15%Sn/CB from 39.901° (20%Pd/CB) to 39.976°, 40.003°, 39.955° and 39.953°, respectively. The small magnitude of upward peak shifts was due to the extensive formation of Ni(OH)₂ which was not able to alloy with Pd completely (Shen *et al.*, 2010; Zhao *et al.*, 2010). On the other hand, Sn could combine with Pd due to their relatively similar atomic radius (Modibedi *et al.*, 2011). As a result, the Pd (1 1 1) peak of 20%Pd20%Sn/C shifted toward lower 2θ.

The maximum intensity of Pd (1 1 1) was used to calculate d-spacing, lattice parameter and crystalline size according to the equations given in XRD theory. The results are shown in Table 6. The lattice parameter is the physical dimension of unit cells in a crystal lattice and d-spacing is the space between the planes. The d-spacing and lattice parameter of 20%Pd were 0.22575 nm and 0.39101 nm, respectively. When Ni was introduced to the catalysts, smaller lattice parameter was obtained. On the other hand, increasing lattice parameter of Sn was found. It was found that 20%Pd15%Ni5%Sn/CB has the lowest d-spacing and lattice parameter with a maximum magnitude of peak shift. Both parameters affected the crystalline size of catalyst; the less value of d-spacing and lattice parameter indicated the smaller crystalline size obtained which mainly contributed to an enhanced catalytic activity. The 20%Pd20%Sn/CB exhibited the highest d-spacing and lattice parameter as its main component was Pd-Sn alloy which was likely to cause the peak shift in comparison with other catalyst compositions. The crystallite size of Pd (1 1 1) was in the range of 8.0-9.4 nm. However, XRD pattern of only carbon support had another peak of carbon between (1 1 1) and (2 0 0) plane at around 43.69 ° shown in

Appendix Figure B1. The Pd peak of (1 1 1) plane was not suitable for calculation of parameters because it could be a lot of errors.

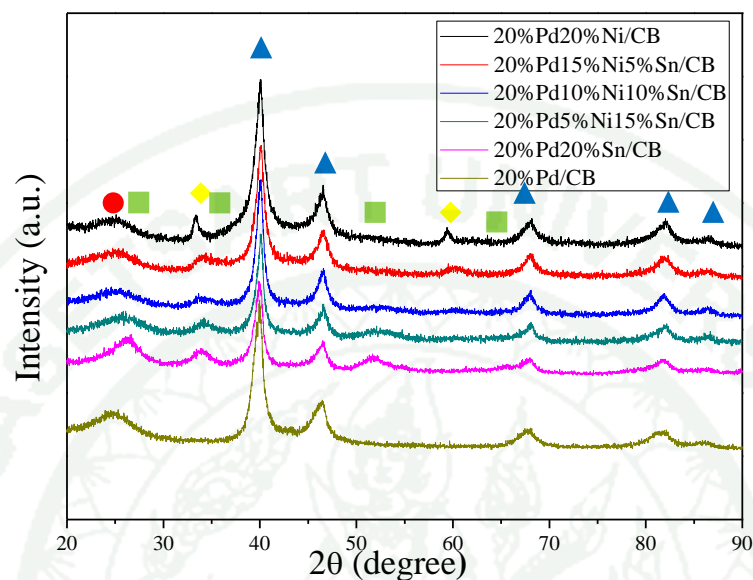


Figure 11 XRD patterns of prepared electro-catalysts compositions, $2\theta = 10-90^\circ$.

● Carbon black ◆ Ni(OH)_2 ■ SnO_2 ▲ Pd

Table 6 A summary of XRD parameters extracted from Pd (1 1 1) peak at 39.901° .

Catalyst	2θ	d-spacing (nm)	Lattice parameter (nm)	Crystallite size (nm)
20%Pd/CB	39.901	0.22575	0.39101	8.8
20%Pd20%Ni/CB	39.976	0.22535	0.39032	8.5
20%Pd20%Sn/CB	39.832	0.22612	0.39165	8.9
20%Pd5%Ni15%Sn/CB	39.953	0.22547	0.39053	8.0
20%Pd10%Ni10%Sn/CB	39.955	0.22546	0.39051	9.4
20%Pd15%Ni5%Sn/CB	40.003	0.22520	0.39006	8.3

However, the crystallite size could not be accurately defined using this Pd (1 1 1) peak since it was a combination of several peaks. Consequently, the Pd (2 2 0) peak was selected to provide the more accurate values of crystallite size as given in Table

7. The 20%Pd/CB had the maximum d-spacing and lattice parameter. It was found that Ni-contained catalysts had lower values of d-spacing and lattice parameter when compared to Sn-contained catalysts. The crystallite size tended to sequentially increase from the smallest (20%Pd/CB) to the larger size with the introduction of Ni and Sn to the Pd catalysts, respectively. The 20%Pd20%Sn/C showed the biggest crystallite size.

Table 7 A summary of XRD parameters extracted from Pd (2 2 0) peak at 67.618°.

Composition	2 θ	d-spacing (nm)	lattice parameter (nm)	Crystalline size (nm)
20%Pd/CB	67.618	0.13843	0.39154	4.5
20%Pd20%Ni/CB	67.901	0.13793	0.39012	5.2
20%Pd20%Sn/CB	67.783	0.13814	0.39071	8.1
20%Pd5%Ni15%Sn/CB	67.818	0.13807	0.39052	6.7
20%Pd10%Ni10%Sn/CB	67.845	0.13802	0.39038	6.8
20%Pd15%Ni5%Sn/CB	67.904	0.13792	0.39009	6.0

1.1.2 Scanning electron microscopy

Scanning electron microscopy was carried out in this study to investigate the surface morphology of supports and catalysts. The SEM images of these catalysts are shown in Figure 12. The particles of metal catalysts were dispersed uniformly on carbon support for all compositions and all supports. Higher magnification of these SEM images (60,000 \times and 80,000 \times) is shown in Appendix Figure C5 to Appendix Figure C10.

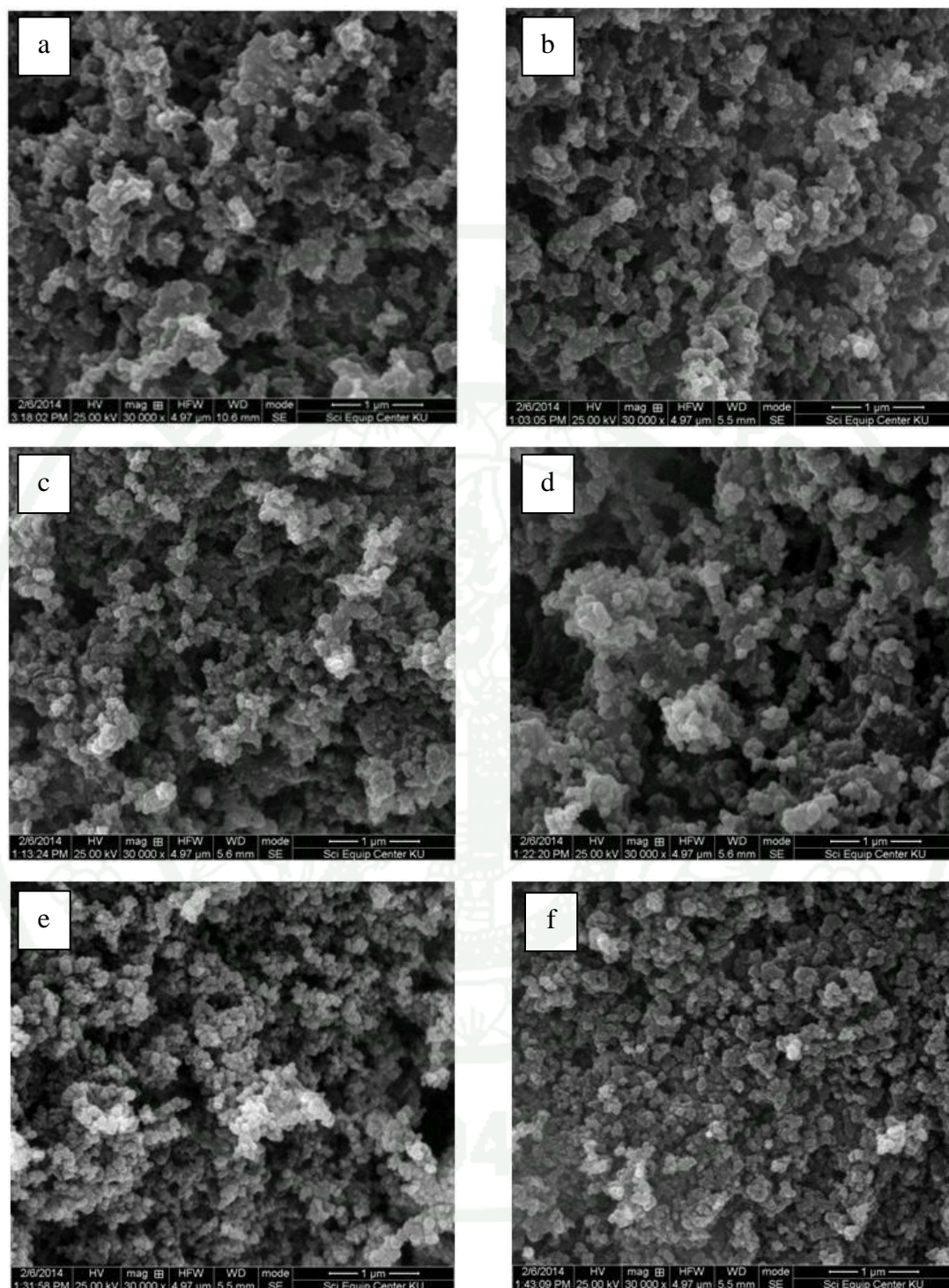


Figure 12 SEM images (taken at the magnification of 30,000 \times) of (a) 20%Pd/CB, (b) 20%Pd20%Sn/CB, (c) 20%Pd20%Ni/CB, (d) 20%Pd5%Ni15%Sn/CB, (e) 20%Pd10%Ni-10%Sn/CB and (f) 20%Pd15%Ni5%Sn/CB.

1.1.3 Energy dispersive x-ray spectrometer

The actual compositions of as-prepared electrocatalysts were analyzed from five sampling points using SEM-EDX. They were relatively similar to the desired compositions as shown in Table 8.

Table 8 A comparison between the desired and actual compositions of as-prepared electrocatalytic using SEM-EDX technique.

Catalyst	Desired composition (% wt)			Actual composition using EDX (% wt)		
	Pd	Ni	Sn	Pd	Ni	Sn
	20%Pd/CB	100	0	0	100.0±0.0	0.0±0.0
20%Pd20%Sn/CB	50	0	50	43.6±0.7	0.0±0.0	56.4±1.0
20%Pd20%Ni/CB	50	50	0	53.9±4.5	46.1±4.3	0.0±0.0
20%Pd5%Ni15%Sn/CB	50	12.5	37.5	43.9±1.2	12.8±1.2	43.3±1.0
20%Pd10%Ni10%Sn/CB	50	25	25	51.0±1.2	17.5±1.2	31.5±1.3
20%Pd15% Ni5%Sn/CB	50	37.5	12.5	45.6±8.0	39.0±9.3	15.4±1.5

1.1.4 Transmission electron microscopy

Transmission electron microscopy was used to investigate the particle size distribution and the dispersion of nanoparticles. The TEM images of all catalyst compositions are shown in Figure 13. It was found that the higher quantity of Sn addition resulted in larger particle size. This indicates the agglomeration occurring at the higher weight percentage of Sn (i.e. 20%Pd20%Sn/CB and 20Pd5%Ni15%Sn/CB) due to the fast reaction of Sn precursors (Zhou *et al.*, 2005). Moreover, Figure 14 shows the well dispersion in case of high Ni or low Sn content. The particle size distribution was shown in histograms (Figure 14). The particle size was ranged between 2-25 nm. The average particle size of 20%Pd/CB, 20%Pd20%Ni/CB,

20%Pd10%Ni10%Sn/CB, 20%Pd15%Ni5%Sn/CB, 20%Pd5%Ni15%Sn/CB and 20%Pd20%Sn/CB were 5.46, 6.14, 6.56, 6.62, 7.56 and 10.56 nm, respectively.

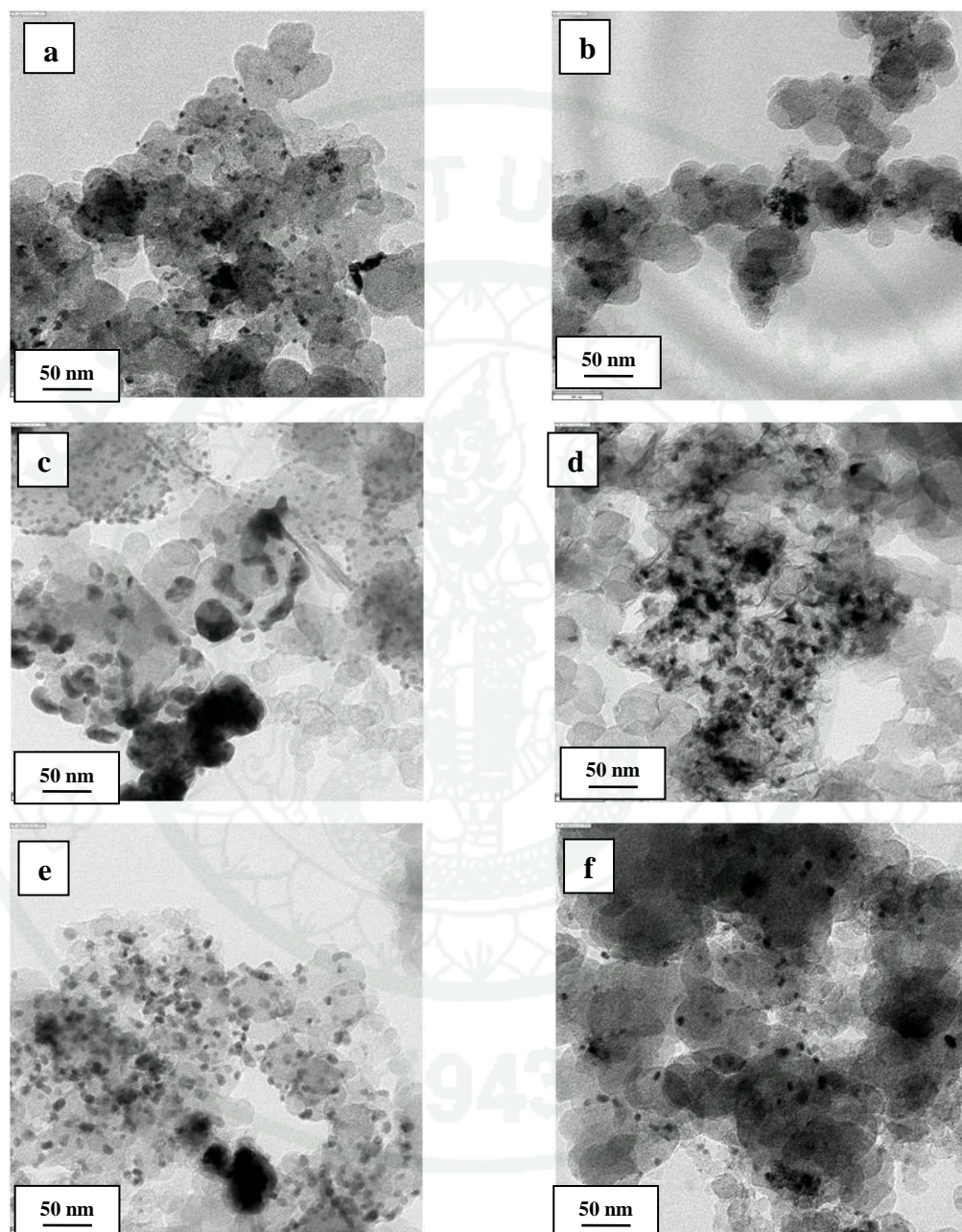


Figure 13 TEM images at 50,000 \times magnification of (a) 20%Pd/CB, (b) 20%Pd20%Sn/CB, (c) 20%Pd20%Ni/CB, 20%Pd5%Ni15%Sn/CB, (e) 20%Pd10%Ni10%Sn/CB and (f) 20%Pd15%Ni5%Sn/CB

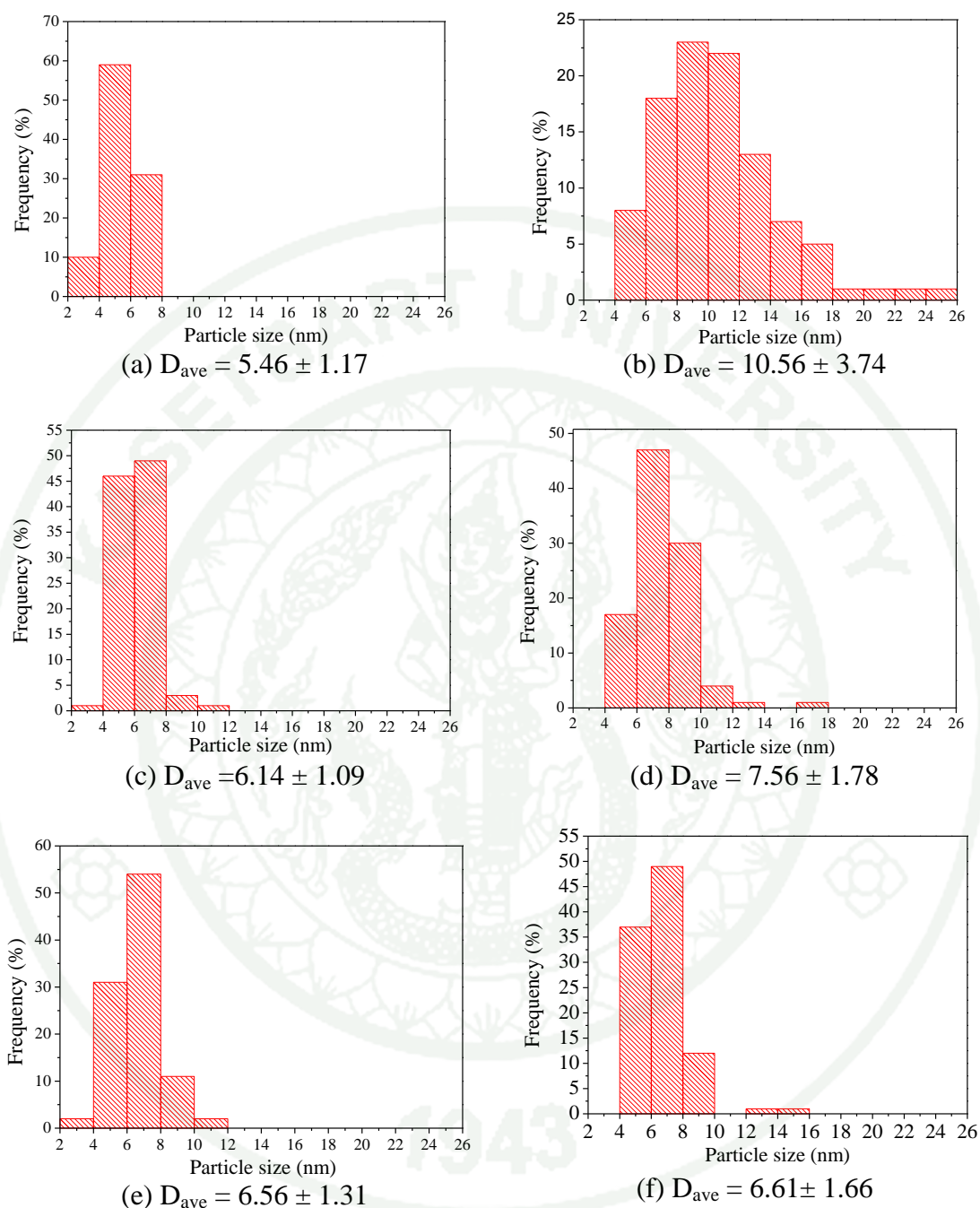


Figure 14 Particle size distribution histograms of (a) 20%Pd/CB, (b) 20%Pd20%Sn/CB, (c) 20%Pd20%Ni/CB, (d) 20%Pd5%Ni15%Sn/CB, (e) 20%Pd10%Ni10-%Sn/CB and (f) 20%Pd15%Ni5%Sn/CB.

1.1.5 Temperature programmed reduction and chemisorption

The TPR was initially used to make sure that the Pd metal was completely reduced by H₂ reduction. The temperature at which the Pd metal was completely reduced was found by TPR test and was used with chemisorption on a dynamic pulse method in a reduction step. The TPR profile of 20%Pd/CB is shown in Figure 15 which was tested at 0-650 °C. However, there were no peaks appearing at the temperature below 100 °C. The reduction temperature was located between 192 °C and 301 °C. Therefore, in the dynamic pulse method, the reduction temperature at 400 °C was used to sure that the H₂ reduction was complete.

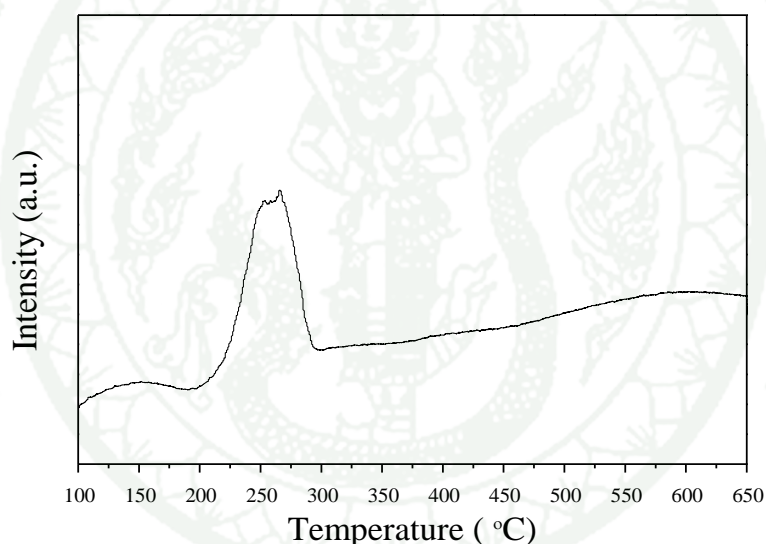


Figure 15 TPR profile of 20%Pd/CB catalyst

The dynamic CO pulse was then used to investigate metal dispersion and the numbers of active sites. The more percentage metal dispersion and numbers of active sites, the higher activity of catalysts obtained. The metal dispersion and the numbers of active sites of all catalyst compositions are shown in Table 9. The metal dispersion and numbers of active sites depends on V_m as shown in equation (10). The catalysts with low weight percentage of Sn exhibited a good metal dispersion and a large number of active sites. The 20%Pd10%Ni10%Sn/CB showed the highest metal

dispersion. It may be because this suitable composition enabled the precursors to undergo reduction reaction at an appropriate rate (Zhou *et al.*, 2005) and the number of active site which were 1.4474% and 1.64×10^{19} , respectively. And the 20%Pd20%Sn/CB showed the lowest metal dispersion because of the high reaction rate of SnCl₂ precursor reduction and the number of active site among all compositions which were 0.0733 % and 8.30×10^{17} , respectively. The CO pulse data is demonstrated in Appendix D.

Table 9 The metal dispersion and numbers of active sites of different catalyst compositions.

Catalyst	D_m (%)	N_s (site)
20%Pd/CB	0.5207	5.89E+18
20%Pd20%Sn/CB	0.0733	8.30E+17
20%Pd20%Ni/CB	0.8217	9.30E+18
20%Pd5%Ni15%Sn/CB	0.2836	3.21E+18
20%Pd10%Ni10%Sn/CB	1.4474	1.64E+19
20%Pd15%Ni5%Sn/CB	0.7448	8.43E+18

1.2 Electrochemical characterization

1.2.1 Catalytic activity

The cyclic voltammograms of EOR (shown in Figure 17) were measured in a mixture of 1 M KOH and 1 M ethanol aqueous solution. The forward scan anodic peak was associated to EOR while the backward anodic peak was corresponding to the removal of CO intermediate (Wei *et al.*, 2011). The pathway of the EOR reaction in alkaline solution consists 2 possible pathways as shown in Figure 16. In the C₁ pathway, the C-C bond of ethanol was broken and converted to the poisoning species (CO_{ads}) which is adsorbed on the Pd surface. This resulted in a loss of active sites. However, only small amount of CO_{ads} can be converted to carbonate ion. For the C₂ pathway, C-C bond of ethanol was not broken and ionized. On the other hand, it was

desorbed and adsorbed on the surface Pd catalyst, yielding the final product, CH_3COO^- product (Ribadeneira and Hoyos, 2008; Shen *et al.*, 2012). The mechanism of C_2 pathway was shown in the following equation:

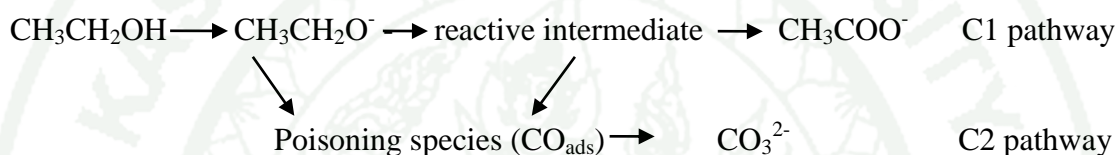
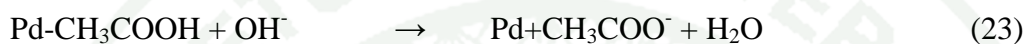
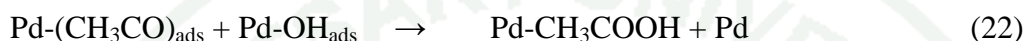
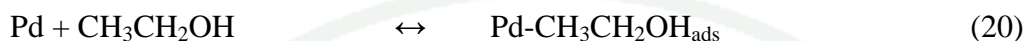


Figure 16 Pathways of electrooxidation reaction of ethanol in alkaline media.

Generally, the anodic peak current of Ni-contained catalysts was found to be higher than those of Sn-contained catalysts as Ni catalyst is known to increase catalyst activity whereas Sn is beneficial to CO tolerance. The Sn precursor was also reported to provide fast reduction reaction that caused the catalyst agglomeration (Shen *et al.*, 2010; Zhou *et al.*, 2005). The onset potential of 20%Pd10%Ni10%Sn/CB (as given in Table 10) was located at the highest negative potential of -0.738 V. This was contrary to the Sn-contained catalysts in which the onset potentials shifted to the highest positive value of about -0.57 V. The results therefore suggested that the anodic peak positions were greatly affected by Ni and Sn contents in the Pd catalysts. The shift in anodic peak position to more negative values was found to increase with Ni content and was greatly increased with Sn content in the Pd catalyst. The highest anodic peak current of approximately 146 mA cm^{-2} was obtained with 20%Pd10%Ni10%Sn. And in the backward scan, the anodic peaks of all catalyst compositions appeared at similar position of $\sim -0.313 \text{ V}$ which associated to the removal of CO-like intermediates (carbonaceous species) which are not completely oxidized during the positive-going sweep (Ksar *et al.*, 2009).

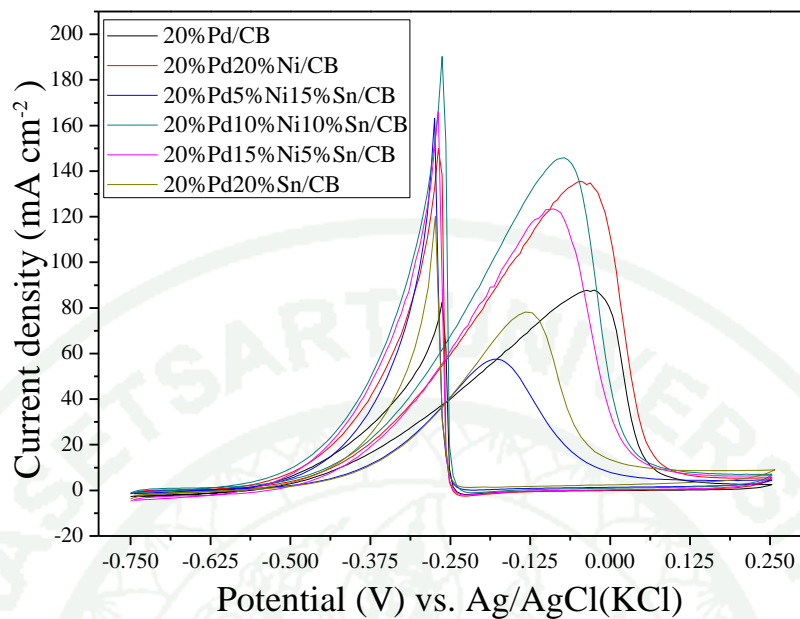


Figure 17 Cyclic voltammograms of different catalyst compositions for EOR in a mixture of 1 M KOH and 1 M ethanol at a scan rate of 50 mV s^{-1}

Table 10 The data extracted from cyclic voltammograms of different catalyst compositions for EOR in a mixture of 1M KOH and 1M ethanol at a scan rate of 50 mV s^{-1} corresponding to Figure 17

Catalyst	Onset potential (V)	Anodic peak voltage (V)	Anodic peak current density (mA cm^{-2})
20%Pd/CB	-0.559	-0.03	88
20%Pd20%Sn/CB	-0.576	-0.13	78
20%Pd20%Ni/CB	-0.715	-0.04	135
20%Pd5%Ni15%Sn/CB	-0.675	-0.18	57
20%Pd10%Ni10%Sn/CB	-0.733	-0.07	146
20%Pd15%Ni5%Sn /CB	-0.530	-0.09	124

1.2.2 Durability of catalysts

The chronoamperometric technique was employed to study the activity behaviors of various catalysts for EOR as a function of time at an applied potential of -0.3 V (vs. Ag/AgCl in 3 M KCl). Figure 18 shows the current response generated from different catalyst compositions in 1 M ethanol containing 1 M KOH solution. In general, the current density was found to decrease rapidly due to the mass transport limitations and then reach its plateau within 100 s. The 20%Pd/CB catalyst was quickly poisoned by CO intermediate. Hence, the current density dropped to approximately ~ 1 mA cm⁻² after 480 s. Ni and Sn in the form of oxide species such as NiO and SnO. The metal form was confirmed by XRD and XPS. It was found that NiO and SnO could convert CO intermediate to CO₂ (An *et al.*, 2013a; Zhang *et al.*, 2011). The catalyst containing high Ni content was able to promote the long-term EOR activity which was found to be more effective than that of high Sn content. Accordingly, 20%Pd20%Ni/CB exhibited an excellent catalytic activity as well as its stability when compared to other catalyst compositions. However, the excessive Ni content can lead to a decrease in the catalytic activity of Pd.

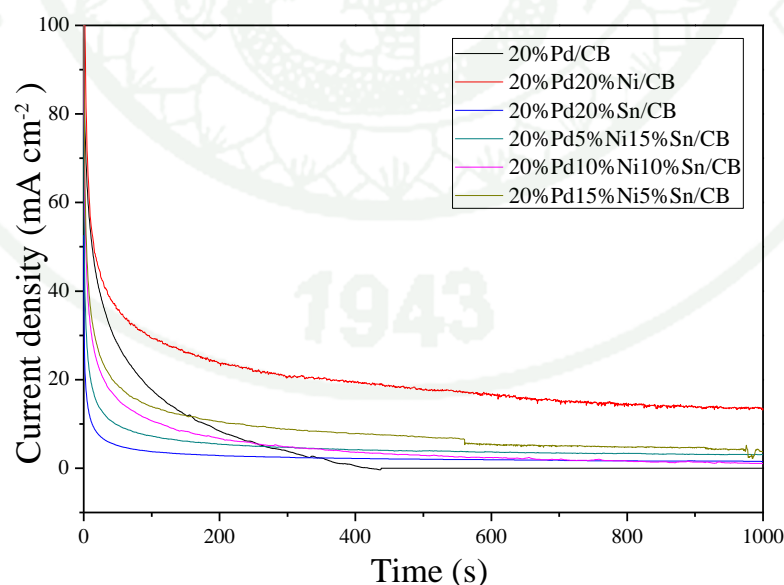
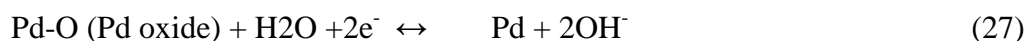


Figure 18 Chronoamperometric curves of different catalyst compositions in 1 M ethanol containing 1M KOH solution at -0.3 V.

1.2.3 CO tolerance

The CO tolerance of various electrocatalyst compositions was studied using CO stripping technique. The CO-stripping voltammograms in 1 M KOH solution (see Figure 19) demonstrated the catalytic activity towards the electrooxidation of CO_{ads} species. The CO oxidation peak appeared in forward scan at the potential of around -0.15 V. The CV profile of catalysts showed anodic and cathodic current density on forward and backward scans, respectively. There was the oxidation peak at about -0.65 V (peak A) in the forward scan which associated to the formation of the adsorbed hydroxyl group (OH_{ads}) on the Pd surface. It became Pd-OH_{ads} and reduced the electron that was electrodesorption as seen in equation (48). The peak potential at approximately -0.25 V (peak B) in the forward scan was associated to CO oxidation. And at higher potential, the peaks C involved to the formation of Pd oxide as shown in equation (49). For 20%Pd/CB and 20%Pd20%Sn/CB that showed only one peak of formation of Pd oxide. For the Ni containing catalyst, it was found that the oxidation peaks of Pd oxide (peak C) and the oxidation of Ni(OH)₂ to NiOOH (peak D) at regional potential were at approximately 0.4-0.5 V. For the backward scan of Ni-containing catalysts, the peak E is associated to the reduction reaction of NiOOH to Ni(OH)₂ at about 0.4-0.2 V as showed in equation (50) (Bagchi and Bhattacharya, 2007, 2008; Simões *et al.*, 2010). And it was also found the peak F involving to the reduction of Pd oxide at approximately -0.3 to -0.5 V as shown in equation (51) (Liu *et al.*, 2007; Takamura and Minamiyama, 2004).



The inset graph in Figure 19 represents the CO adsorption peaks in a potential range -0.6 and 0.1 V. Interestingly, the pre-oxidation peak of SnO₂ can be observed at around -0.4 V in all Sn-containing catalysts which was attributed to the formation of Pd-Sn species on the surface of catalyst which also served as active sites for CO

oxidation. Wang *et al.* (2010) also studied about Pd-Co species. He claimed that the Pd-Co catalyst could pre-oxidize and promote CO tolerance (Wang *et al.*, 2010). The onset potential is the important parameter generally used to consider the catalytic activity for CO oxidation. The 20%Pd15%Ni5%Sn/CB exhibited the lowest onset potential so it was more favorable toward the CO oxidation than the other catalyst compositions. Moreover, the peak width and height of 20%Pd15%Ni5%Sn/CB as well as the peak area was the highest indicating that 20%Pd15%Ni5%Sn/CB has an excellent performance for CO oxidation. The onset and the peak potentials of all catalyst compositions for CO stripping are given in Table 11. The CO oxidation peaks of all catalysts were in the range of -0.104 and -0.185 V. The 20%Pd15%Ni5%Sn/CB showed the lowest on set potential for CO oxidation at about -0.525 V. On the other hand, 20%Pd/CB has the highest onset potential indicating that which meant it exhibited low efficiency in CO oxidation.

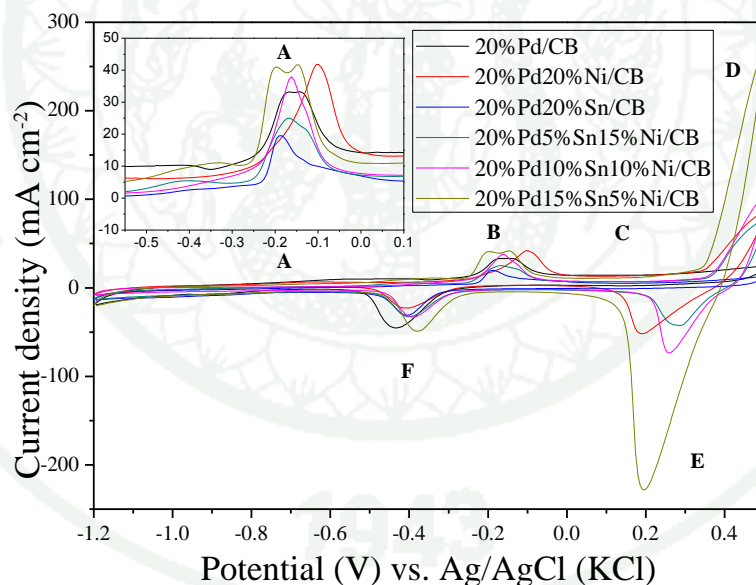


Figure 19 CO stripping voltammograms of all catalyst compositions in 1 M KOH solution.

Table 11 The onset potential and peak potential of all catalyst compositions for CO oxidation activity corresponding to the voltammograms in Figure 19.

Catalyst	CO stripping onset potential (V)	CO stripping peak potential (V)
20%Pd/CB	-0.350	-0.138
20%Pd20%Ni/CB	-0.385	-0.104
20%Pd20%Sn/CB	-0.485	-0.185
20%Pd5%Ni15%Sn/CB	-0.498	-0.168
20%Pd10%Ni10%Sn/CB	-0.478	-0.162
20%Pd15%Ni5%Sn/CB	-0.525	-0.145

1.2.4 Electrochemical surface area

Figure 20 shows the cyclic voltammograms of various catalyst compositions in 1 M KOH at scanned potential between -1.2 and 0.5 V. The CV profiles of all catalysts are similar to Figure 19. However, the peak potential of approximately -0.5 to -0.3 V in the forward scan was related to a non-reaction region and so-called “double layer”. The area under the OH⁻ desorbed peak (shown in Table 12) was substituted in equation (18) to obtain the ESAs given in Table 12. The 20%Pd10%Ni10%Sn/CB showed the highest ESA of 59.255 m² g⁻¹ Pd which is consistent with the TEM and SEM results in which small particle size and uniform dispersion of metal particles was obtained on CB support (Anonymous, 2013) and 20%Pd20%Sn/CB showed the lowest ESA of 24.650 m² g⁻¹ Pd as a result of metal agglomeration caused by the fast reduction of Sn precursor (Zhou *et al.*, 2005). The trend of ESAs was increased with the Ni content; however, 15 wt% Ni content reduced small magnitude of ESA that probably due to the excess quantity of Ni content which led to metal agglomeration and hence a decreased surface area (Shen *et al.*, 2010).

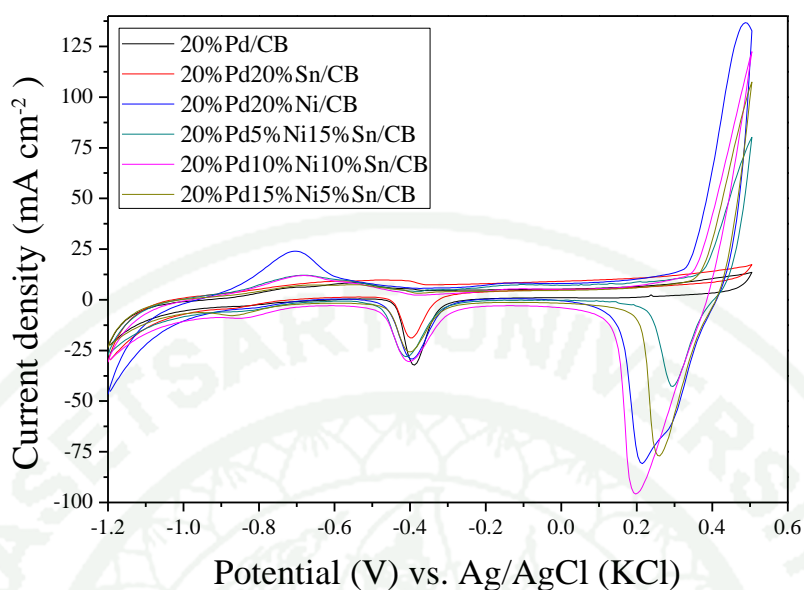


Figure 20 Cyclic voltamograms for different catalyst compositions in 1 M KOH solution.

Table 12 The area under the desorbed OH^- peak (Q_s) and ESA of different catalyst compositions.

Catalyst	Q_s (mC cm^{-2})	ESA ($\text{m}^2 \text{g}^{-1} \text{Pd}$)
20%Pd/CB	10.865	28.170
20%Pd20%Sn/CB	9.509	24.650
20%Pd20%Ni/CB	15.269	39.585
20%Pd5%Ni15%Sn/CB	11.191	29.015
20%Pd10%Ni10%Sn/CB	22.856	59.255
20%Pd15%Ni5%Sn/CB	13.324	34.545

The best composition which exhibited the maximum current density for EOR was 20%Pd10%Ni10%Sn/CB. In the next section, the effect of carbon support on catalytic activity was carried out based on the best catalyst composition which is 20%Pd10%Ni10%Sn/CB. It was prepared on various carbon supports.

2. Functionalization of carbon-based supports

The carbon supports were used including carbon blacks (denoted as CB), functionalized carbon blacks (denoted as CB_{sn}), multi-walled carbon nanotubes (denoted as MWCNT) and functionalized multi-walled carbon nanotubes (denoted as MWCNT_{sn}). The physical characterization was used to investigate the success of support functionalization including scanning electron microscopy, thermogravimetric analysis, Raman spectroscopy, Fourier transform infrared spectroscopy (FTIR), surface area and porosity analyzer.

2.1 Scanning electron microscopy

The acid functionalization is known to be a process of removing impurities and inserting acid functional group on the surface of carbon supports. The hydroxyl group (-OH) of carbon supports was replaced herein by carboxylic group (-COOH) (Rike Y. *et al.*, 2011; Zaiton *et al.*, 2010). Figure 21-24 showed the SEM images of CB and MWCNTs before and after functionalization. The modified surface can be observed as rougher surface when compared to the non-functionalized ones. Furthermore, it was found that MWCNT_{sn} was agglomerated after acid-functionalization. The particle size of both CB_{sn} and MWCNT_{sn} was found to decrease after acid functionalization because some impurities were removed from the support surface. The average particle size of CB_{sn} was smaller than that CB of about 17.34 %. The average tube diameters of MWCNT_{sn} were smaller than MWCNT for about 28.64 %. The histograms of average particle and average tube diameter size of carbon-based supports are shown in Appendix Figure C1-C4. It was found that the average particle size of CB and CB_{sn} 102.6 nm and 84.8 nm, respectively and average tube diameters of MWCNT and MWCNT_{sn} 76.8 nm and 56.6 nm, respectively.

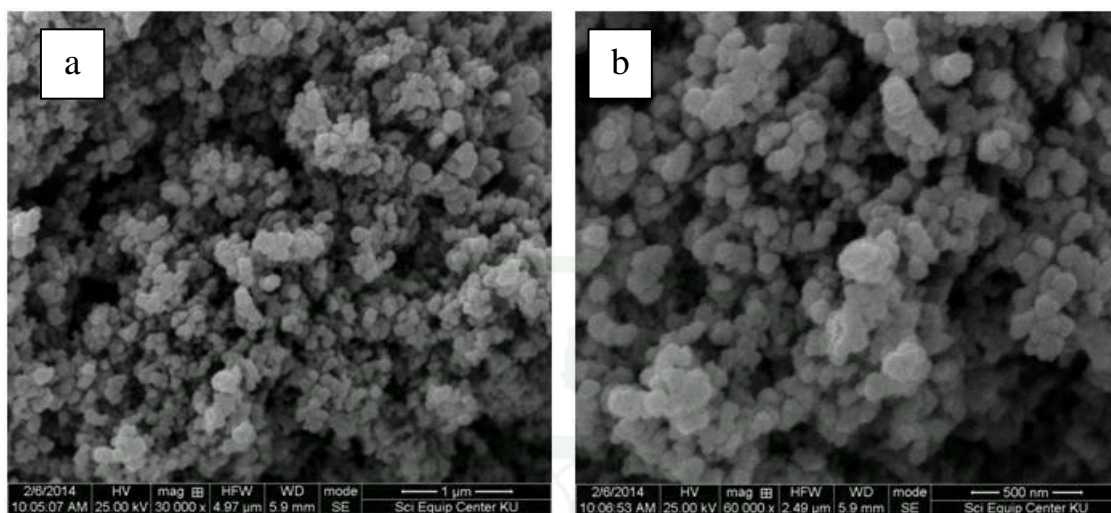


Figure 21 SEM images of CB with magnifications of (a) 30,000 \times and (b) 60,000 \times

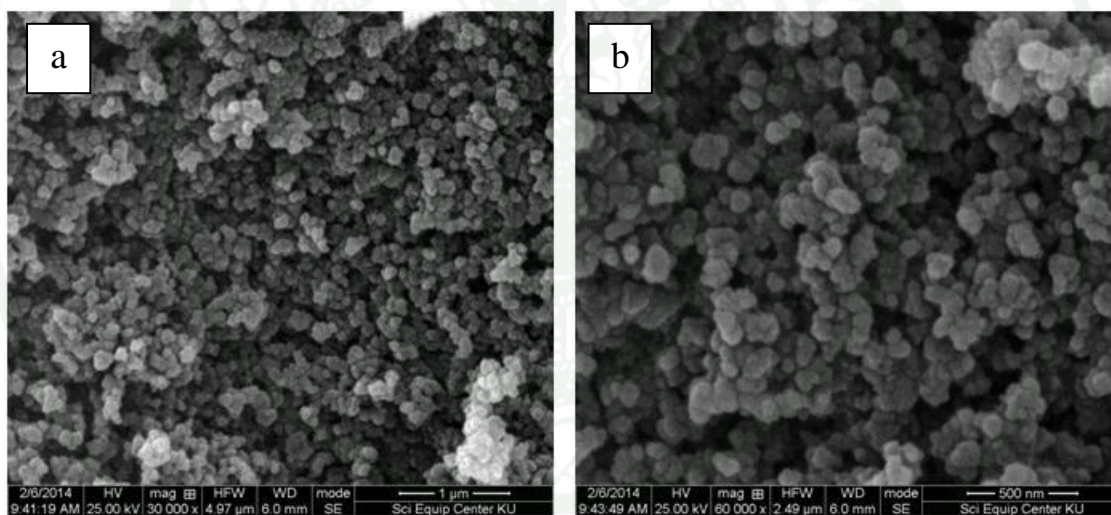


Figure 22 SEM images of CB_{sn} with magnifications of (a) 30,000 \times and (b) 60,000 \times .

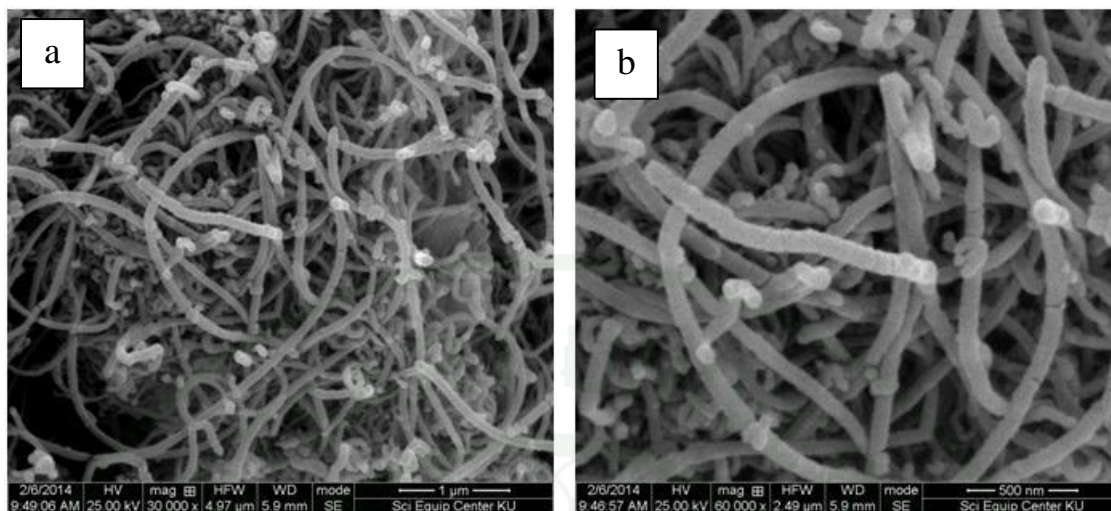


Figure 23 SEM images of MWCNT with magnifications of (a) 30,000 \times and (b) 60,000 \times .

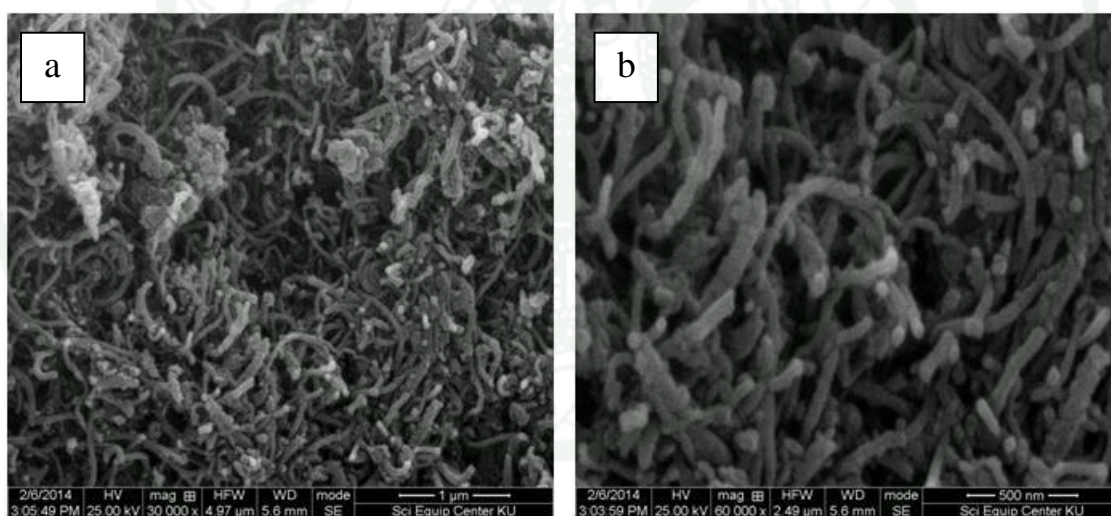


Figure 24 SEM images of MWCNT_{sn} with magnifications of (a) 30,000 \times and (b) 60,000 \times .

2.2 Raman spectroscopy

Raman spectroscopy was used to verify the existence of -COOH functional groups with the change of bond structure among functionalized carbon supports. Figure 25 and Figure 26 demonstrates Raman spectrum of all carbon supports.

The D and G band were observed around 1350 and 1580 cm^{-1} , respectively. The D band was found as a shoulder of G band at around 1622 cm^{-1} generating from a double resonance process similar to the D-band. It is suggested that the D band was originated from hybridized vibration associated with graphene edges which was usually used to indicate the presence of disorder in the graphene structure. The higher intensity of D band in CB_{sn} referred to the higher defect or disorder in graphene structure as compared to that of CB. The high intensity of G band indicated less carbon amorphous and high crystalline of the untreated MWCNTs as the carbon structure may be changed from amorphous to crystalline after the treatment. G' band (the overtone of D band at 2D) was corresponding to the stacking order of the graphitic walls and the crystalline of the graphitic planes (Dang *et al.*, 2006; Pimenta *et al.*, 2007; Romanos *et al.*, 2011). The ratios of D band and G band intensity ($I_{\text{D}}/I_{\text{G}}$) are given in Table 13. If this ratio increases it can be implied that there is the defect of carbon structure caused by the acid functionalization. According to the results, the ratio was not changed but the peak is narrower indicating the removal of impurities from carbon support. The ratio of MWCNT_{sn} was relatively higher than that of MWCNTs as a result of covalent functionalization of the MWCNT sidewall was increased after acid treatment (Daugaard *et al.*, 2012).

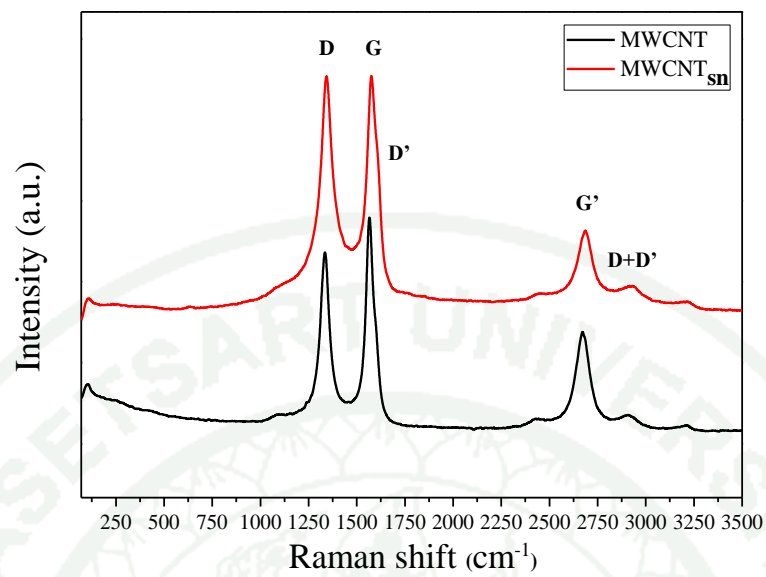


Figure 25 The Raman spectrum of MWCNT and MWCNT_{sn}.

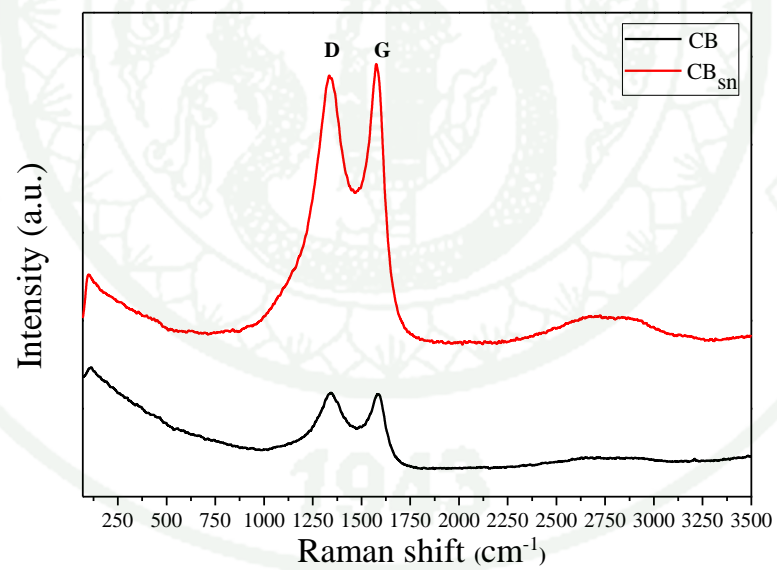


Figure 26 The Raman spectrum of CB and CB_{sn}.

Table 13 The I_D/I_G ratio of carbon supports.

Support	I_D/I_G ratio
CB	0.837
CB _{sn}	0.828
MWCNT	0.803
MWCNT _{sn}	0.970

2.3 Thermogravimetric analysis

TGA results are shown in Figure 27. The differential graphs in Appendix E were clearly used to identify the degradation of different functional groups at around 230-380 °C. The decomposition temperature of carbon-based supports was in a range between 400 and 700°C. It can be seen that both functionalized supports started to decompose at lower temperature of about 100 °C when compared to the non-functionalized (i.e. untreated samples) ones. This indicated that the existence of acid functional groups in the supports caused a decrease in their thermal stability since -COOH has lower degradation temperature than -OH. The weight loss of those functionalized supports was located at approximately 230°C associated with the decomposition of carboxylic groups (Osorio *et al.*, 2008). It was also found that the decomposition temperature of MWCNT_{sn} was higher than that of CB_{sn} as a consequence of high crystallinity of MWCNT_{sn} support according to the XRD result. The residues obtained at the end of TGA measurement, indicated the impurity level of the samples (Osorio *et al.*, 2008). Both functionalized supports contained fewer residues than that of the non-functionalized ones after the thermal decomposition as the acid functionalization helped to remove some impurities despite causing the reduction of thermal stability. The weight percents of acid functional groups were 5.85% and 5.42% for CB_{sn} and MWCNT_{sn}, respectively.

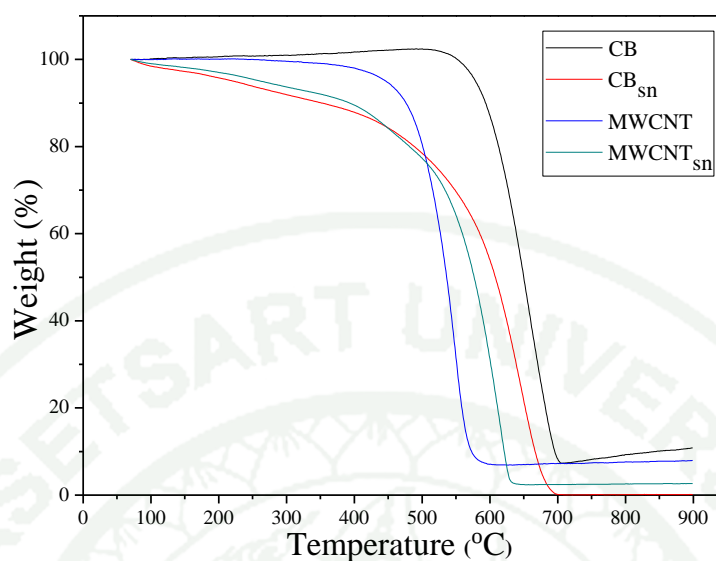


Figure 27 TGA thermograms of different carbon supports.

2.4 Fourier transform infrared spectroscopy

FTIR was used to confirm the functional group attached to the support structures as shown in Figure 28 and 29. The stretch and bending vibrations of atoms were used to determine the functional groups in the structure. It could be seen that characteristic peaks of CB_{sn} and $MWCNT_{sn}$ were located at the same positions but the peak intensity of CB_{sn} was weaker than that of $MWCNT_{sn}$. The fingerprint region below 1400 cm^{-1} hardly identified compounds because of its complexity. The peak at around 3400 cm^{-1} and 1640 cm^{-1} referred to H-bond of hydroxyl groups and H-bond of carboxyl groups ($C=O$) respectively that conjugated with $C=C$ bonds (i.e. approximately 1600 cm^{-1}) in the graphene wall of $MWCNT_{sn}$ (Shieh *et al.*, 2007). In addition, the peaks at approximately 2900 cm^{-1} and 620 cm^{-1} corresponding to C-H bond were also obtained which also undergo oxidation reaction due to the presence of C-O bonds at approximately 1475 cm^{-1} . Moreover, the peak at around 1100 cm^{-1} can be observed indicating the formation of sulfonated groups and C-O vibration. According to the results obtained, the acid treatment enabled the purification and/or functionalization of carbon supports to occur based on the oxidation reaction of the double bond in the graphene wall which yielded sulfonated group ($-SO_3$), carboxylic

group (-COOH), and hydroxyl group (-OH) on the carbon surface (Hu *et al.*, 2003; Marshall *et al.*, 2006).

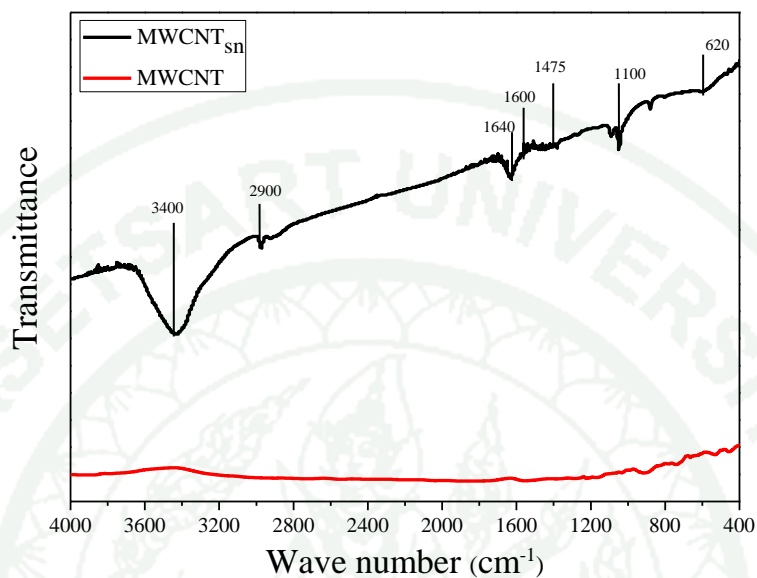


Figure 28 The FTIR spectrum of MWCNT and MWCNT_{sn}.

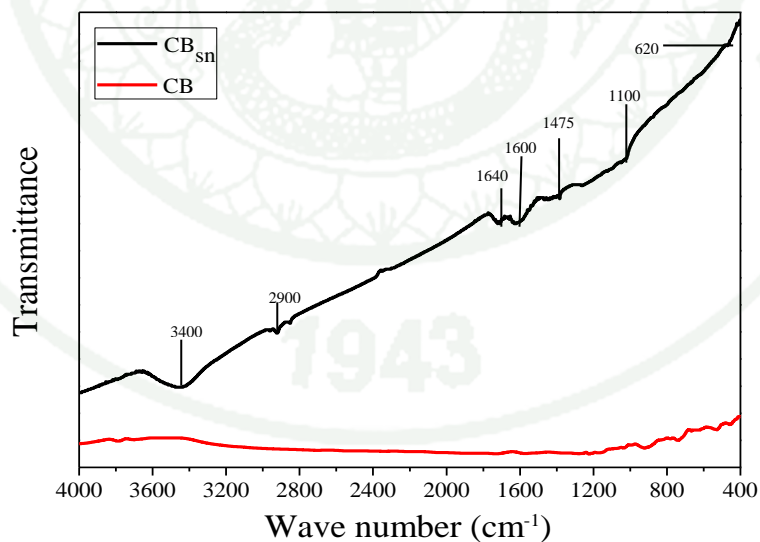


Figure 29 The FTIR spectrum of CB and CB_{sn}.

2.5 Surface area and pore size distribution

For electrochemical properties, the surface area is important. The specific surface areas (SSAs) of supports reflect the catalytic activity. The multilayer adsorption model or the Brauner, Emmet and Teller (BET) method was also used to analyze the surface area of the supports. According to IUPAC isotherms, all supports showed the type-II adsorption isotherms which a normal form of isotherm obtained from an unrestricted monolayer-multilayer adsorption on finely divided non-porous adsorbent. The Type-II isotherm represents. In all samples, the adsorption and desorption loops (or hysteresis loop) referred to the pore shape of supports which is a typical H₃ type (Sing *et al.*, 2008): bottle-shaped-contained broad capillaries with a narrow and short neck (Komarow, 1997). The Appendix Figure F1-F5 show the isotherm of supports and the isotherm of IUPAC. Figure 30 showed the BET plot of functionalized and non-functionalized supports. From the BET plot, the S_{BET} values were calculated and listed in Table 14 (The S_{BET} calculation as shown in Appendix F). The S_{BET} of the MWCNT was 221 m² g⁻¹ which was in the range of 150-450 m² g⁻¹ reported by literatures (Inoue *et al.*, 1998; Yang *et al.*, 2001) while that of non-functionalized CB was 427.4 m² g⁻¹ which was in the range of 10-1500 m² g⁻¹ reported by literatures (Ferdinand, 1988). The S_{BET} of MWCNT_{sn} and CB_{sn} was found to decrease by 42% and 62%, respectively which was similar to the findings reported Cañete-Rosales *et al* (2012)'s study. The BET surface area shows a decrease of two functionalised supports due to the increasing functional group content. The decrease in BET surface area by introducing the –COOH functional group to both MWCNTsn and CBsn was caused by the blocking of the inter-bundle galleries and intra-bundle interstitial channels with the presence of –COOH functional group (Jha *et al.*, 2013). Moreover, total pore volume was decreased after functionalization.

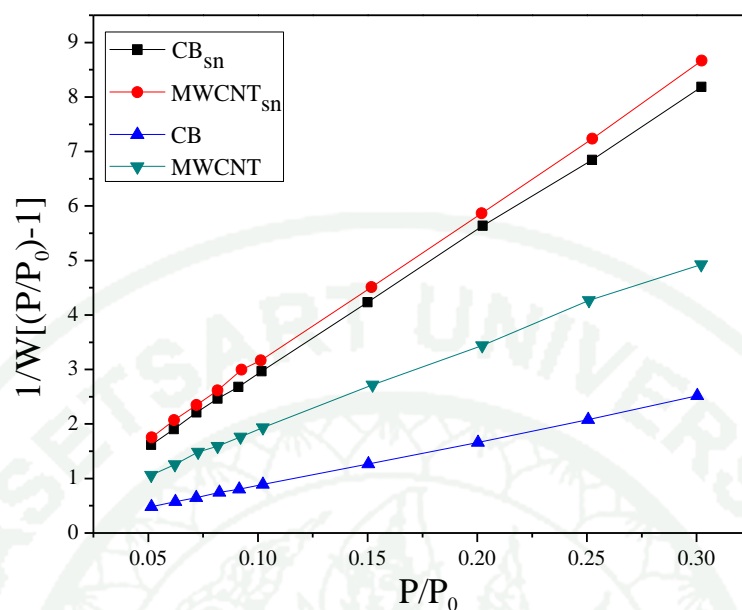


Figure 30 BET plots of functionalized and non-functionalized supports

Table 14 Summary of BET surface area, average pore size and total pore volume.

Type of supports	BET surface area S_{BET} (m ² /g)	Average pore size (nm)	Total pore volume (cm ³ /g)
CB	427.4	12.3	1.3
MWCNT	221.0	27.3	1.5
CB _{sn}	132.1	16.1	0.5
MWCNT _{sn}	126.0	11.9	0.4

Additionally, the BET method was used to calculate the pore size distributions from desorption of nitrogen isotherms. The plot was size distribution was shown in Figure 31. The pore size as shown in Table 14 was less than 250 Å or 25 nm (greater 2 nm but less than 50 nm) in all samples which were in the range of mesopore as same reported by Puskás *et al* (2012). results (Puskás *et al.*, 2012).

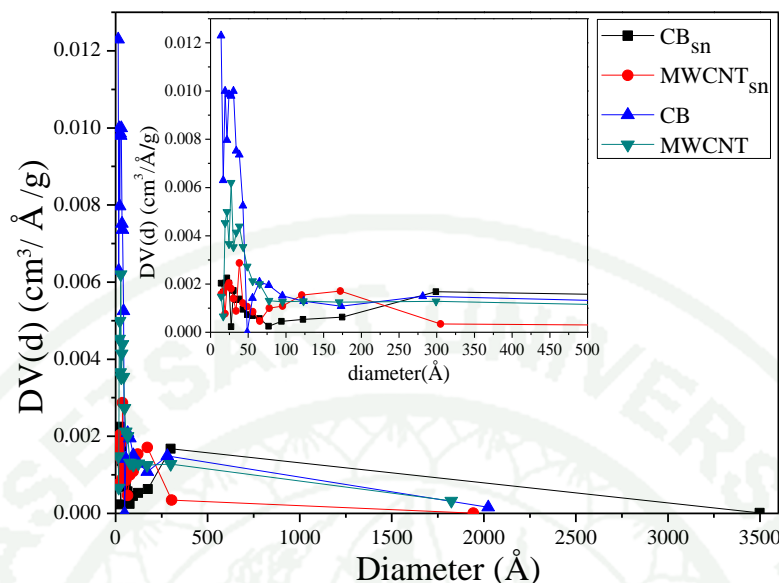


Figure 31 The pore size distribution of different carbon supports and inset graph of the micropore and mesopore size distributions of carbon supports.

Different catalyst supports were then used to support 20%Pd10%Ni10%Sn catalyst for further investigations.

3. Evaluation of catalyst on various carbon-based supports

20%Pd10%Ni10%Sn was impregnated on four different carbon supports: CB, CB_{sn} , MWCNT and $MWCNT_{sn}$. The selected catalyst composition showed the maximum current density for EOR as reported in our previous study. The physical properties of 20%Pd10%Ni10%Sn deposited on various carbon supports were analyzed using XRD, SEM-EDX, TEM, CO-pulse chemisorption and XPS. Then, the electrochemical properties were characterized using a potentiostat/galvanostat to explore the activity, durability, CO tolerance and electrochemical surface area of those samples.

3.1 Physical characterization

3.1.1 X-ray diffraction

All catalysts reveal the similar peak positions indicating the identical forms of metal catalysts deposited on different supports as shown in Figure 32. The first peak at around 25-30° was (0 0 2) plane of carbon structure in CB or MWCNTs. The characteristic peaks of Pd included the peaks at 39.901°, 46.209°, 67.618°, 81.364° and 86.342° which referred to (1 1 1), (2 0 0), (2 2 0), (3 1 1) and (2 2 2) planes, respectively. All of the Pd represented face centred cubic (FCC) structure. The peaks at 33.193° and 59.303° referred to (1 0 0) and (1 1 0) planes of Ni(OH)₂ respectively whereas the peaks at 26.511°, 33.769°, 51.612° and 65.752° referred to (1 1 0), (1 0 1), (2 1 1) and (3 0 1) planes of SnO₂ respectively. The SnO₂ peaks were overlapped with the peaks of carbon (25-30°), Ni(OH)₂ (33.193°) and Pd (67.618°) so they were hardly observed.

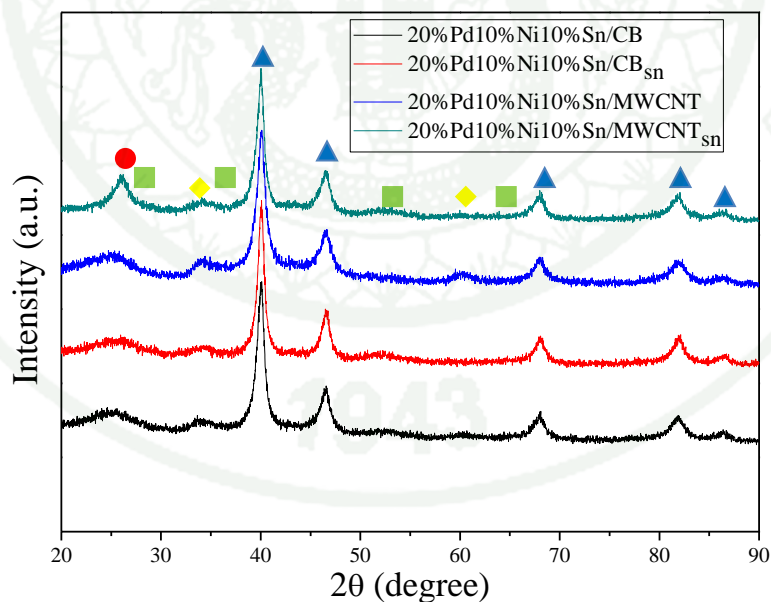


Figure 32 XRD patterns of the as-prepared 20%Pd10%Ni10%Sn electro-catalyst on various carbon supports, $2\theta = 20-90^\circ$ ● Carbon ◆ Ni(OH)₂ ■ SnO₂ ▲ Pd.

The peak of Pd (2 2 0) at 67.618° was used to calculate spacing, lattice parameter and crystalline size in all samples. The values of both parameters were explained in detail and the effect of them which were accorded in the first part of the XRD result. The results are given in Table 15. It was found that the crystalline size of 20%Pd10%Ni10%Sn catalyst on various supports was in the range of 6.4 – 7.4 nm with similar values of d-spacing and lattice parameter.

Table 15 Summary of XRD calculation of peak Pd (2 2 0).

Composition	2 θ	d-spacing (nm)	lattice parameter (nm)	Crystalline size (nm)
20%Pd10%Ni10%Sn/CB	67.845	0.13802	0.39038	6.8
20%Pd10%Ni10%Sn/CB _{sn}	67.911	0.13791	0.39007	6.6
20%Pd10%Ni10%Sn/MWCNT	67.916	0.13790	0.39004	6.4
20%Pd10%Ni10%Sn/MWCNT _{sn}	67.813	0.13808	0.39054	7.4

3.1.2 Scanning electron microscopy

The SEM images of all samples are demonstrated in Figure 33. The metal particles were dispersed uniformly on the surface of carbon supports. More SEM images are shown in Appendix Figure C5 to C14.

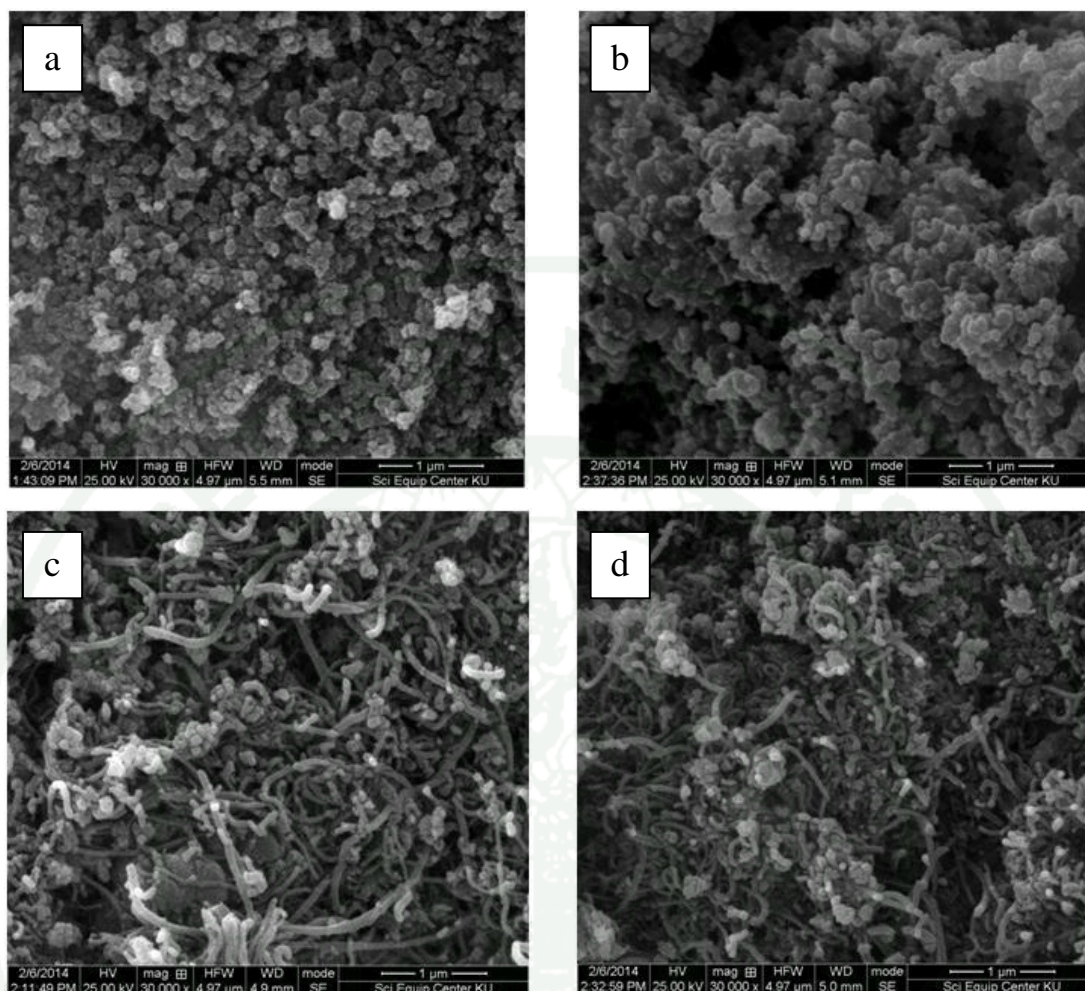


Figure 33 SEM images of (a) 20%Pd10%Ni10%Sn/CB, (b) 20%Pd10%Ni10%Sn/CB_{sn}, (c) 20%Pd10%Ni10%Sn/MWCNT and (d) 20%Pd10%Ni10%Sn/MWCNT_{sn}.

3.1.3 Energy dispersive X-ray spectrometer

The actual compositions of as-prepared catalyst samples were examined using SEM-EDX with 5 sampling points. It was found that the actual compositions were relatively similar to the desired compositions for all samples as shown in Table 16.

Table 16 A comparison between the desired and actual compositions of as-prepared electrocatalysts deposited on various supports

Catalyst	Desired composition (% wt)			Actual composition using EDX (% wt)		
	Pd	Ni	Sn	Pd	Ni	Sn
	20%Pd10%Ni10%Sn/CB	50	25	25	49.2 ±2.9	23.6 ±5.5
20%Pd10%Ni10%Sn/CB _{sn}	50	25	25	52.1 ±4.7	16.5 ±2.0	31.4 ±3.34
20%Pd10%Ni10%Sn/MWCN T	50	25	25	53.8 ±4.0	16.8 ±2.4	29.4 ±2.1
20%Pd10%Ni10%Sn/MWCN T _{sn}	50	25	25	45.4 ±6.5	29.2 ±6.3	25.4 ±1.8

3.1.4 Transmission electron microscopy

TEM images of 20%Pd10%Ni10%Sn on various supports (in Figure 34) show that metal catalysts were well distributed and dispersed on all carbon supports. The histograms of catalyst particle size distribution on various supports (shown in Figure 35) reveal the average particle size of 20%Pd10%Ni10%Sn/MWCNT_{sn}, 20%Pd10%Ni10%Sn/MWCNT, 20%Pd10%Ni10%Sn/CB, 20%Pd10%Ni10%Sn-CB_{sn} were 6.08 ± 1.40 , 6.40 ± 1.87 , 6.56 ± 1.31 and 6.65 ± 1.72 nm, respectively. Accordingly, the catalyst deposited on different supports exhibited similar particle size but the metals on MWCNT_{sn} showed the good dispersion and small size. This is because the MWCNT_{sn} attributed to improved solubility in DI water of catalyst preparation, which was easy to make the small particle size and uniform dispersion of metal particles deposited on the outer walls of the MWCNT_{sn} (Yang *et al.*, 2008).

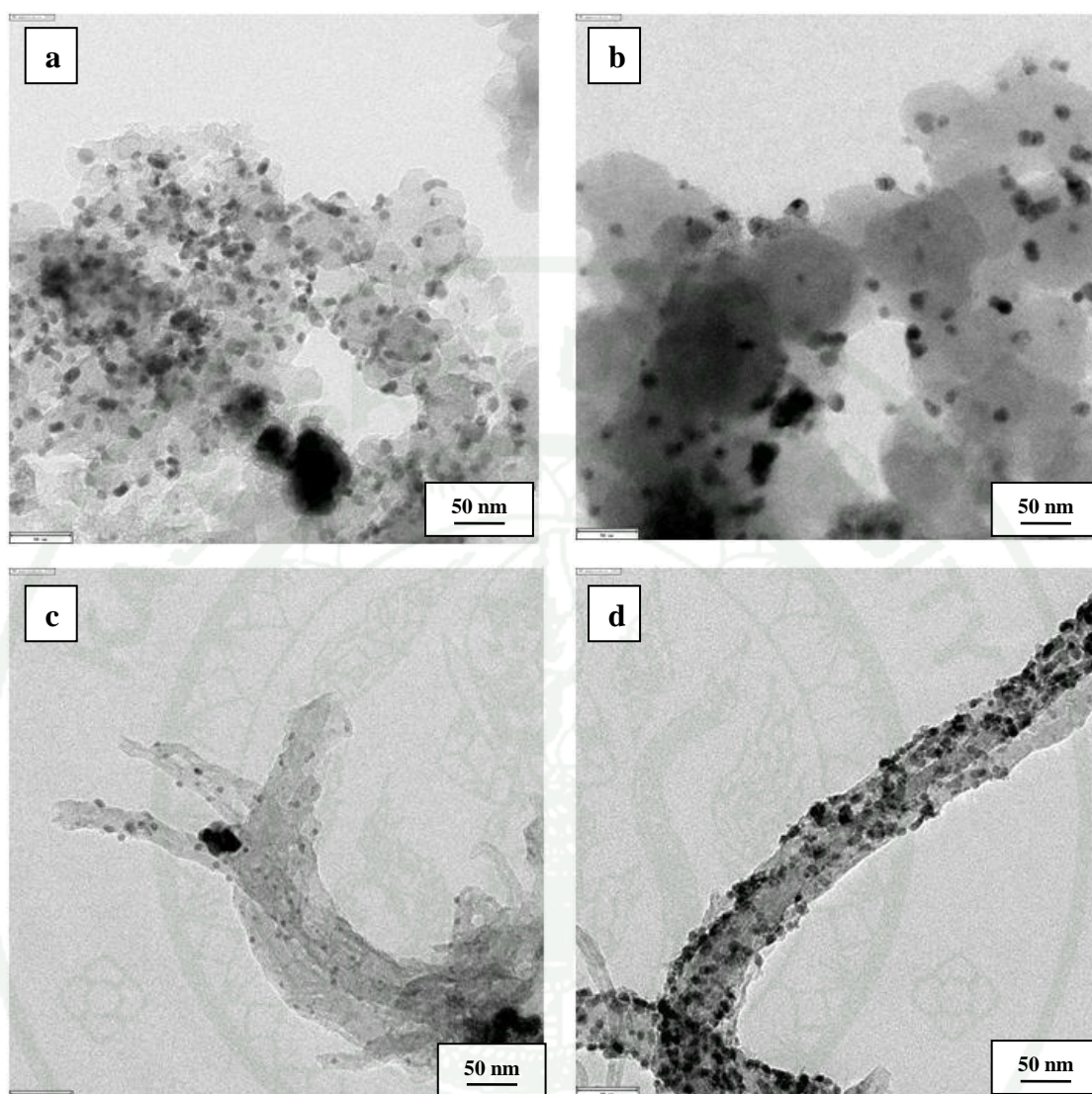


Figure 34 TEM images at $\times 50,000$ magnification of (a) 20%Pd10%Ni10%Sn/CB, (b) 20%Pd10%Ni10%Sn/CB_{sn}, (c) 20%Pd10%Ni10%Sn/MWCNT and (d) 20%Pd10%Ni10%Sn/MWCNT_{sn}.

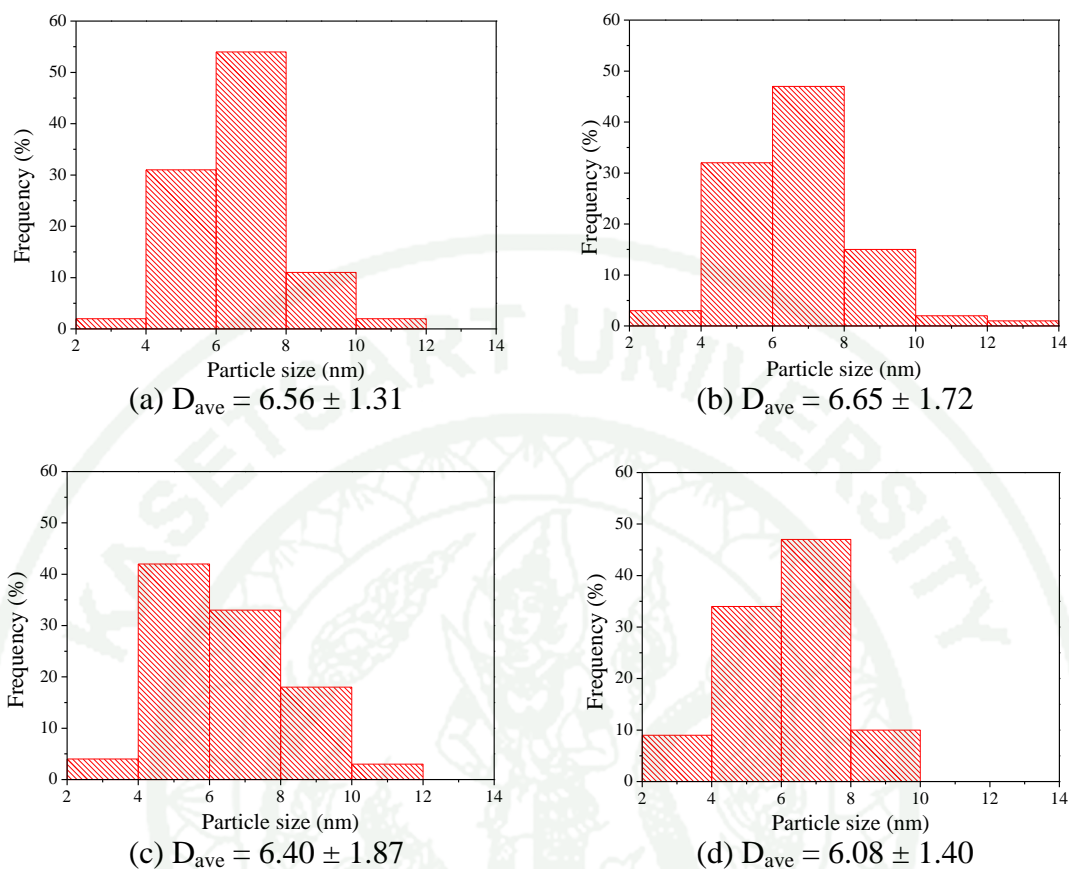


Figure 35 Particle size distributions for (a) 20%Pd10%Ni10%Sn/CB, (b) 20%Pd10%Ni10%Sn/CB_{sn}, (c) 20%Pd10%Ni10%Sn/MWCNT and (d) 20%Pd10%Ni10%Sn/MWCNT_{sn}.

3.1.5 Chemisorption

The metal dispersion (D_m) and the number of active sites (N_s) of 20%Pd10%Ni10%Sn on various supports assessed by chemisorption are given in Table 17. It was found that the catalyst on both MWCNT_{sn} and CB_{sn} exhibited high levels of D_m and N_s which can be implied that well-dispersed and distributed metal particles were obtained with the use of functionalized carbon supports. This was consistent to the results observed in TEM images.

Table 17 The metal dispersion and number of active sites of 20%Pd10%Ni10%Sn on various supports.

Catalyst	D_m (%)	N_s (site)
20%Pd10%Ni10%Sn/CB	1.4474	1.64E+19
20%Pd10%Ni10%Sn/CB _{sn}	2.1705	2.46E+19
20%Pd10%Ni10%Sn/MWCNT	0.9251	1.05E+19
20%Pd10%Ni10%Sn/MWCNT _{sn}	2.8822	3.26E+19

3.1.6 X-ray photoelectron spectroscopy

XPS was carried out in this study to investigate oxidation number of metals which indicates how active metal catalyst can be. Figure 36 show the XPS survey scan for the 20%Pd10%Ni10%Sn on CB_{sn} and MWCNT_{sn} supports. The 20Pd10%Ni10%Sn catalyst showed the maximum current density for EOR which was utilized to characterize the effect of support surface on its catalytic activity and the oxidation state of metal catalysts. The XPS spectra were used to study in detail in the interaction among Pd, Ni, and Sn. The survey scan revealed the atom peaks of carbon (C 1s), oxygen (O 1s), nickel (Ni 2p), tin (Sn 3d) and palladium (Pd 3d). The XPS spectrum of Pd 3d peak consisted of two main peaks that were a high-energy (Pd 3d_{3/2}) and a low-energy (Pd 3d_{5/2}). The binding energy of Pd 3d_{3/2} and Pd 3d_{5/2} peaks were located at 341.0 and 335.7 eV for both CB_{sn} and MWCNT_{sn} supports. The Pd 3d_{5/2} peak included 3 sub-peaks with binding energies of 335.7, 336.5 and 337.2 eV associated to Pd metal (Pd⁰) and PdO (Pd²⁺) forms (Li *et al.*, 2011; Shen *et al.*, 2010). Those detailed XPS spectrum of Pd 3d peak are shown in Figure 37 for 20%Pd10%Ni10%Sn/CB_{sn} and 20%Pd10%Ni10%Sn/MWCNT_{sn}, respectively. The XPS area ratio of the chemical state of Pd species is given in Table 18. It was found that the ratio of Pd and PdO on both CB_{sn} and MWCNT_{sn} supports were relatively similar. The high Pd content indicated higher catalytic activity obtained. The XPS spectrum of Ni 2p peak are demonstrated in Figure 38 for 20%Pd10%Ni10%Sn/CB_{sn} and 20%Pd10%Ni10%Sn/MWCNT_{sn}. The XPS spectrum of Ni 2p peak contained the 2 main peaks: Ni 2p_{3/2} and Ni 2p_{1/2}. The Ni 2p_{3/2} normally consisted of 4 sub-peaks

observed in Ni 2p_{3/2} referred to Ni, NiO, Ni(OH)₂ and NiOOH with the binding energies appeared at 852.8, 855.1, 856.2 and 857.6 eV, respectively. The oxidation state of Ni, NiO, Ni(OH)₂ and NiOOH was Ni⁰, Ni²⁺, Ni²⁺, and Ni³⁺, respectively (Park *et al.*, 2004; Shen *et al.*, 2010). The XPS area ratio of chemical state of Ni species is also shown in Table 18. For both catalyst the Ni(OH)₂ showed the highest ratio which was favorable of EOR. This was consistent with the XRD results. The XPS spectrum of Sn 3d included Sn 3d_{5/2} and Sn 3d_{3/2} peaks (see Figure 39). The Sn 3d_{5/2} peak was consisted of 3 peaks with the binding energy at 485.5, 487.6, 488 eV which were associated to Sn-SnO (Sn⁰ Sn²⁺) and SnO₂ (Sn⁴⁺) (An *et al.*, 2013b; An *et al.*, 2013a). The XPS area ratio of chemical state of Sn species is showed in Table 18. The XPS spectrum of C 1s peak was found at the binding energy of 285.0 eV in both CB_{sn} and MWCNT_{sn}. More details regarding their spectrum are given in Appendix Figure G1-G4.

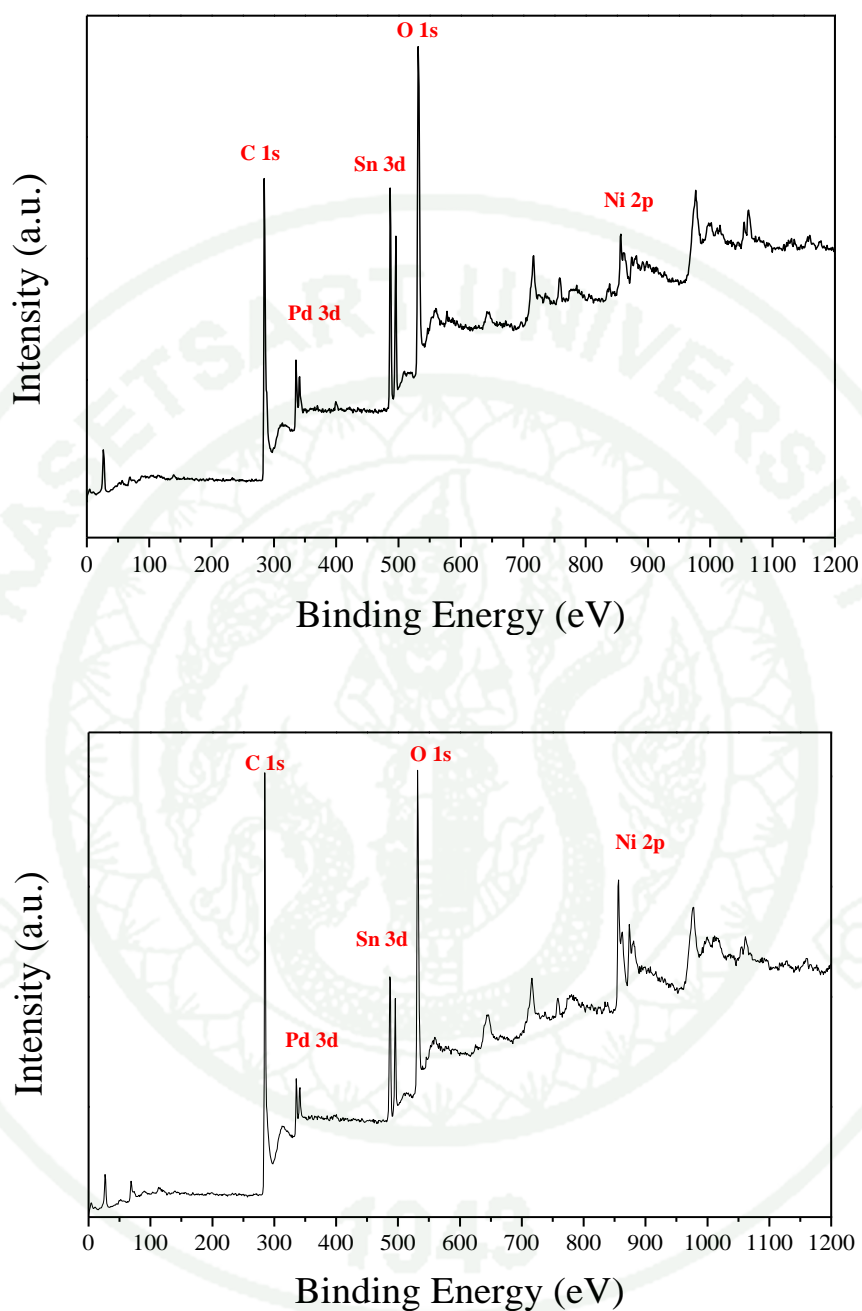


Figure 36 The survey XPS spectrum of (a) 20%Pd10%Ni10%Ni/CB_{sn} and (b) 20%Pd10%Ni10%Sn/MWCNT_{sn}.

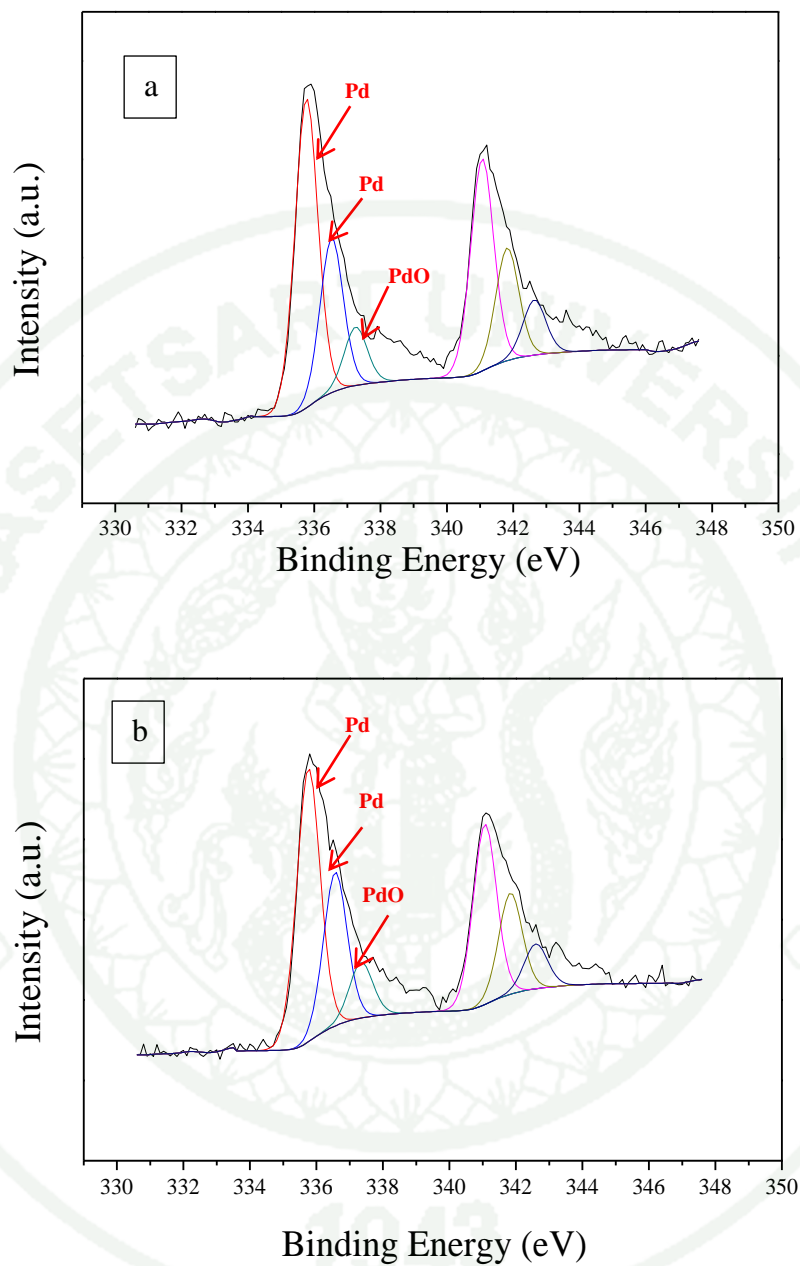


Figure 37 The detailed XPS spectrum of Pd for (a) 20%Pd10%Ni10%Sn/CB_{sn} and (b) 20%Pd10%Ni10%Sn/MWCNT_{sn}.

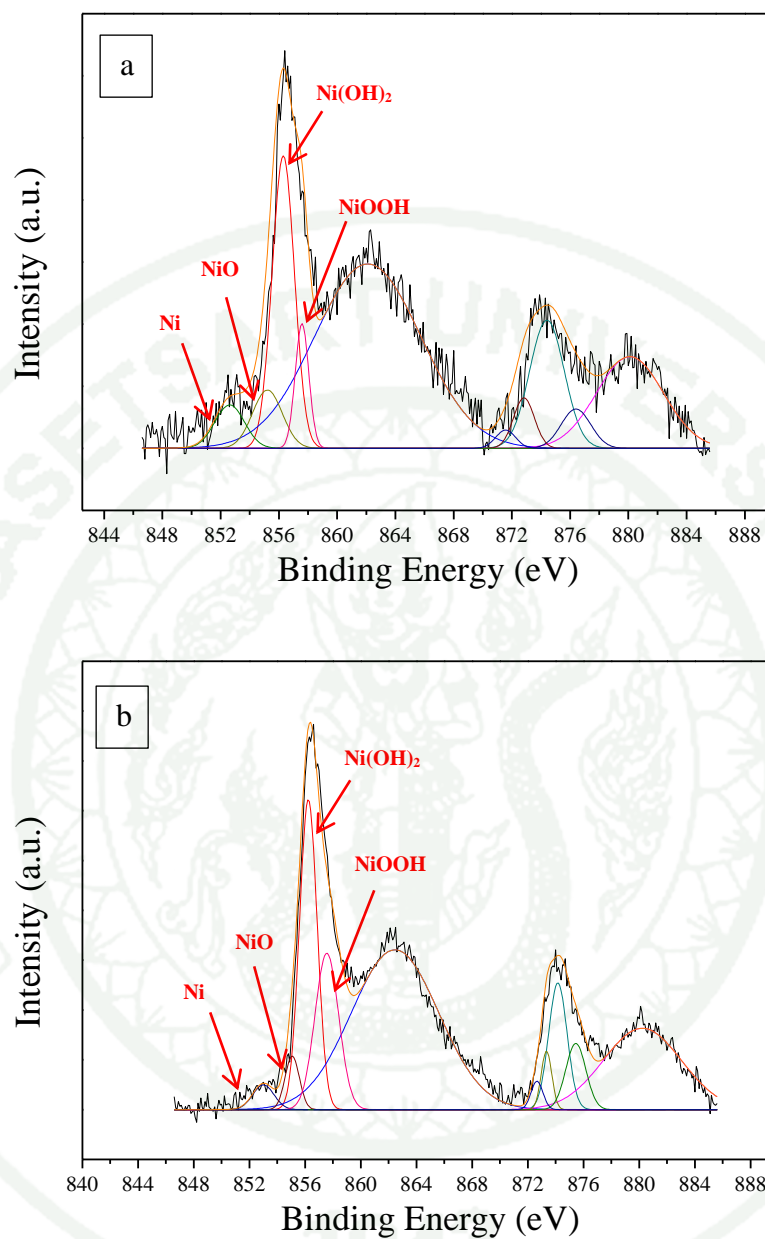


Figure 38 The detailed XPS spectrum of Ni for (a) 20%Pd10%Ni10%Sn/CB_{sn} (b) 20%Pd10%Ni10%Sn/MWCNT_{sn}.

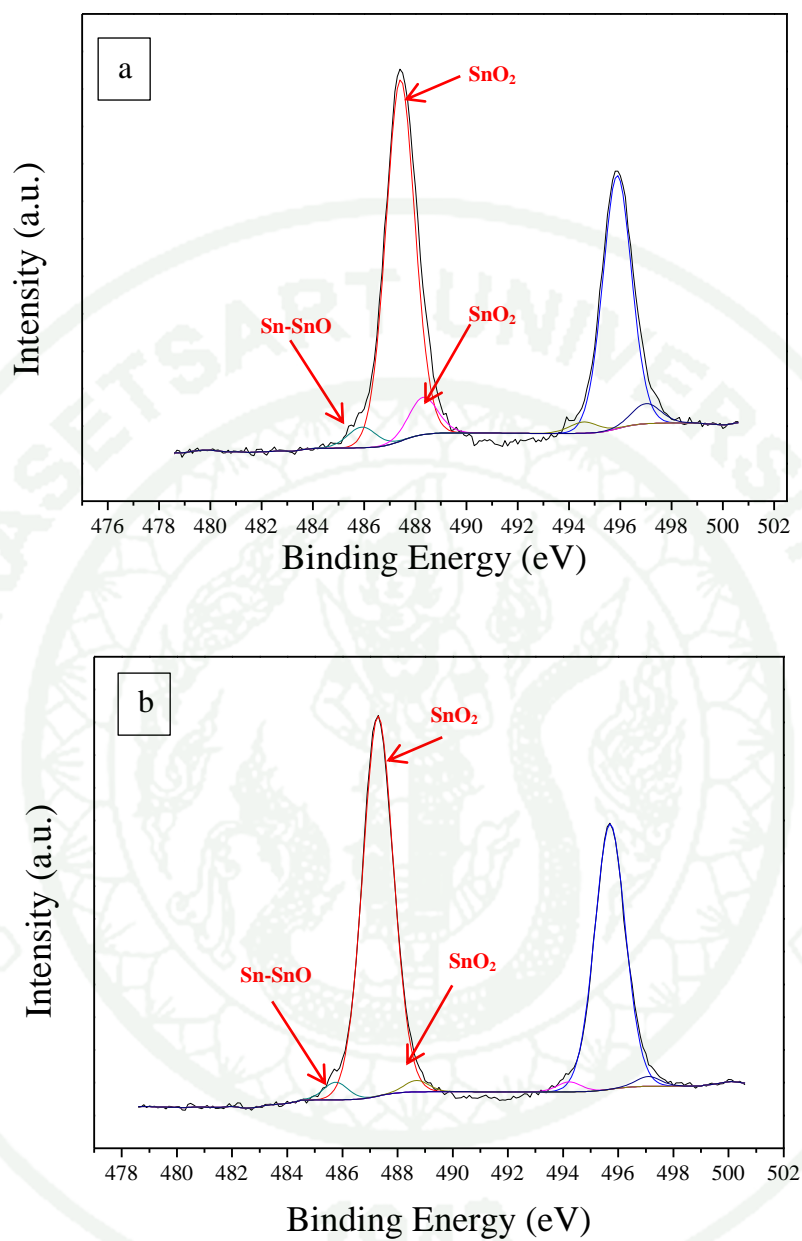


Figure 39 The detailed XPS spectra XPS of Sn for (a) 20%Pd10%Ni10%Sn/CB_{sn} (b) 20%Pd10%Ni10%Sn/MWCNT_{sn}.

Table 18 XPS area ratios of chemical state of Pd, Ni and Sn species.

Form of metal	XPS area ratio (%)	
	20%Pd10%Ni10%Sn/CB _{sn}	20%Pd10%Ni10%Sn/MWCNT _{sn}
Pd (Pd ⁰)	87.5	12.5
PdO (Pd ²⁺)	87.5	12.5
Ni (Ni ⁰)	9.0	5.7
NiO (Ni ²⁺)	15.3	9.2
Ni(OH) ₂ (Ni ²⁺)	60.0	51.8
NiOOH (Ni ³⁺)	15.7	33.3
Sn-SnO (Sn ⁰ ,Sn ²⁺)	4.5	95.5
SnO ₂ (4+)	3.3	96.7

3.2 Electrochemical characterizations

3.2.1 Catalytic activity

The cyclic voltammograms of the catalyst for EOR were recorded in a mixture of 1 M ethanol and 1 M KOH aqueous solution as shown in Figure 40. The EOR can be observed on the anodic peak which was located between -0.2 and 0.1 V. It can be seen that the onset potential were relatively similar in all samples. Table 19 shows the corresponding anodic peak potentials and current densities for EOR. The 20%Pd10%Ni10%Sn/MWCNT_{sn} exhibited the maximum current density of 291 mA cm⁻². It was suggested that the catalytic activity towards EOR was more favourable when the catalyst exhibited higher magnitude of anodic current density but lower value of the onset potential (Qingfeng Yi, 2011). The results confirmed that the 20%Pd10%Ni10%Sn deposited on functionalized supports generated higher current density than those on non-functionalized supports. In terms of catalyst activity, MWCNT_{sn} was found to be a promising catalyst support for EOR in DEFC.

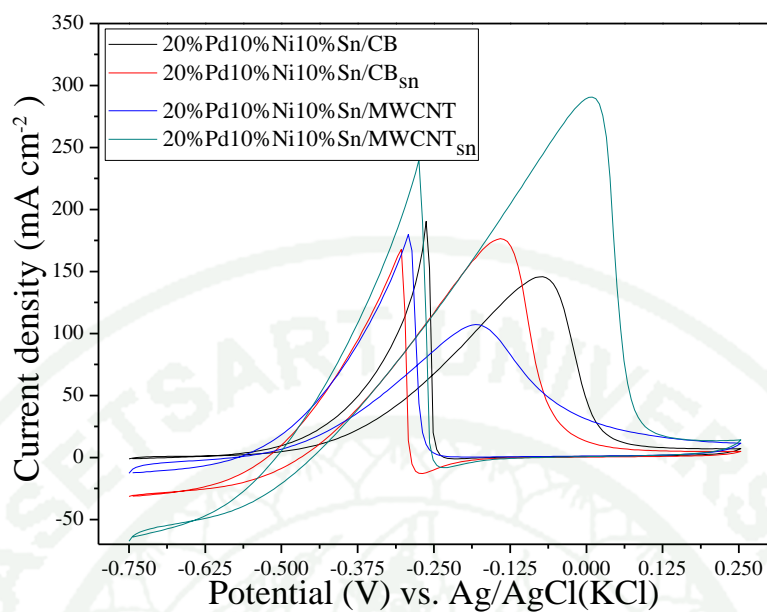


Figure 40 The voltammograms of 20%Pd10%Ni10%Sn on different types of catalyst supports with/with no functionalization in a mixture of 1 Methanol and 1 M KOH.

Table 19 The data extracted from cyclic voltammograms of 20%Pd10%Ni10%Sn using different types of catalyst supports with/with no functionalization in a mixture of 1 M KOH and 1M ethanol at a scan rate of 50 mA s^{-1} corresponding to Figure 40.

Catalyst	Onset potential (V)	Anodic peak voltage (V)	Anodic peak current density (mA cm^{-2})
20%Pd10%Ni10%Sn/CB	-0.738	-0.077	146
20%Pd10%Ni10%Sn/CB _{sn}	-0.744	-0.141	177
20%Pd10%Ni10%Sn/WMCNT	-0.733	-0.182	107
20%Pd10%Ni10%Sn/WMCNT _{sn}	-0.744	0.096	291

3.2.2 Durability of catalysts

The catalyst durability of 20%Pd10%Ni10%Sn deposited on different catalyst supports was determined by chronoamperometry and the results are demonstrated in Figure 41. The percentage of current drop of MWCNT_{sn}, MWCNT, CB and CB_{sn} were 97.42, 98.85, 99.24 and 100%, respectively. Thus, 20%Pd10%Ni10%-Sn/MWCNT_{sn} exhibited the greatest catalyst stability. The reason for that was because the covalent bonds of carboxylic functional groups attached to the MWCNT_{sn} surface enabled a good interaction among metals and support (Liu *et al.*, 2013) and the high degree of crystallinity of the MWCNT_{sn} support resulted in a good electrical connection in molecular level as showed in XRD data in Appendix Figure B1.

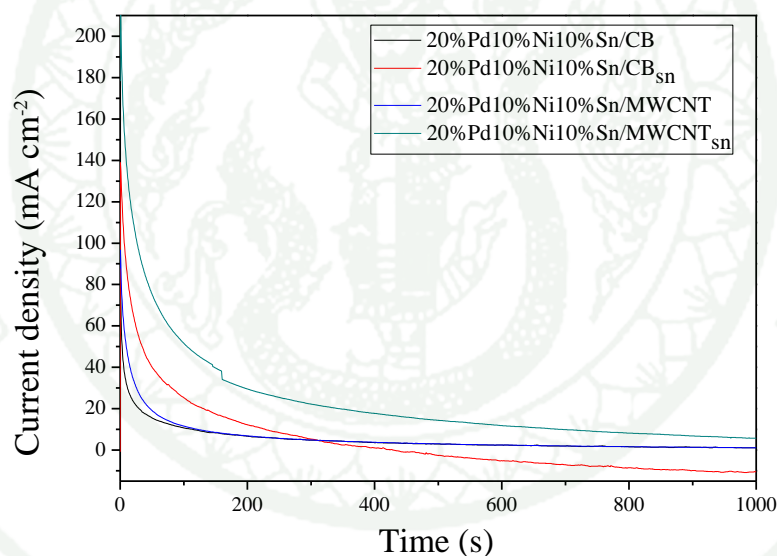


Figure 41 Chronoamperometric curve of 20%Pd10%Ni10%Sn catalyst using different catalyst supports in a mixture of 1 M ethanol and 1 M KOH solution at an applied potential of -0.3 V.

3.2.3 CO tolerance

CO-stripping test is also used to indicate the catalyst ability with the presence of CO poisoning. CO-stripping voltammograms of 20%Pd10%Sn10%Ni on various

supports are demonstrated in Figure 42. The inset showed the onset potential and the peak potential for CO oxidation. The peak of CO oxidation occurred at around -0.1 to -0.2 V with the onset potential in a range of -0.368 to -0.480 V. The onset of all peaks was not much different but the height of the peaks could be clearly observed. The maximum peak current for CO oxidation was obtained with the 20%Pd10%Sn10%Ni/CB_{sn} whereas the minimum peak current was observed in the 20%Pd10%Sn10%Ni/MWCNT_{sn}. This indicated that the 20%Pd10%Sn10%Ni/CB_{sn} could uptake the highest amount of CO molecules in comparison with the other catalyst samples. The onset and peak potentials for CO-stripping process extracted from Figure 42 are detailed in Table 20. The peak potential was in the range of -0.162 to -0.179 V. The 20%Pd10%Ni10%Sn/MWCNT and 20%Pd10%Ni10%-Sn/MWCNT_{sn} had the lower onset potentials than those of 20%Pd10%Ni10%Sn/CB and 20%Pd10%Ni10%Sn/CB_{sn}, indicating the high efficiency for CO tolerance obtained by using MWCNT supports.

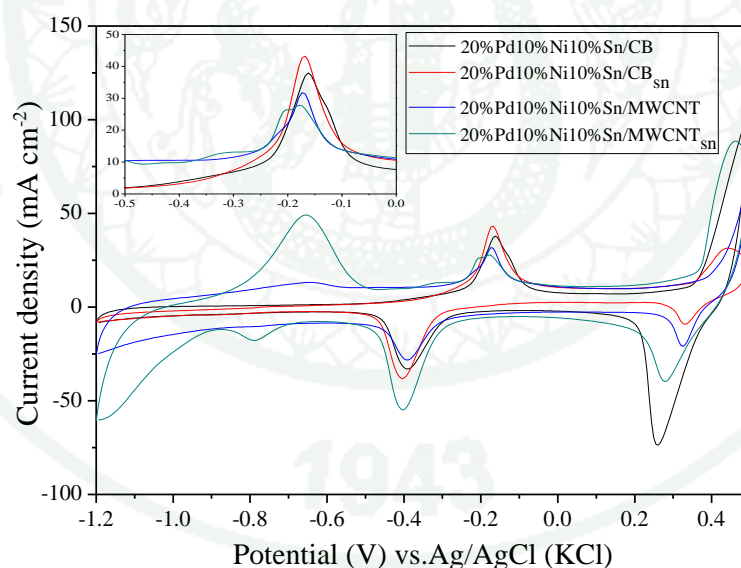


Figure 42 CO stripping voltammograms of 20%Pd10%Ni10%Sn catalyst on various supports.

Table 20 Electrochemical CO oxidation activity of 20%Pd10%Ni10%Sn catalyst on various supports.

Catalyst	CO stripping onset potential (V)	CO stripping peak potential (V)
20%Pd10%Ni10%Sn/CB	-0.478	-0.162
20%Pd10%Ni10%Sn/CB _{sn}	-0.480	-0.168
20%Pd10%Ni10%Sn/MWCNT	-0.415	-0.179
20%Pd10%Ni10%Sn/MWCNT _{sn}	-0.368	-0.174

3.2.4 Electrochemical surface area

ESAs of the 20%Pd10%Ni10%Sn on various supports were determined by hydroxyl (OH⁻) adsorption in 1 M KOH solution. Figure 43 demonstrates the cyclic voltammograms of those catalyst samples. The OH⁻ desorption was used to calculate the ESA values (given in Table 21). The anodic peak appears in forward scan and cathodic peak in backward scan. In the forward scan, the oxidation peak at -0.65 V was associated to the formation of the OH⁻ group adsorption (OH_{ads}) on the Pd surface which was then converted to Pd-OH_{ads}. After that, the backward scan caused the electrodesorption of pre-adsorbed OH_{ads}. It can be seen that the use of functionalized supports exhibited higher ESAs than those of the non-functionalized supports. Among the samples, the MWCNT_{sn} was found to be the most suitable support for the deposition of 20%Pd10%Ni10%Sn as a ternary catalyst in DEFC as it had the excellent catalytic activity and stability, the great performance for CO tolerance and the highest ESA

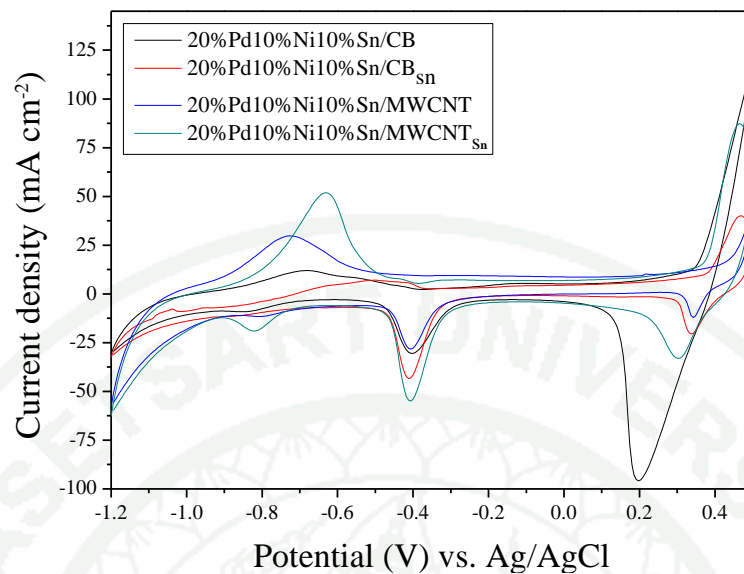


Figure 43 Cyclic voltammograms of 20%Pd10%Ni10%Sn catalyst on various supports in 1M KOH solution

Table 21 The area of desorbed OH⁻ peak and ESA of 20%Pd10%Ni10%Sn catalyst on various supports

Catalyst	Area of desorbed OH ⁻ peak (mC cm ⁻²)	ESA (m ² g ⁻¹ Pd)
20%Pd10%Ni10%Sn/CB	22.856	59.255
20%Pd10%Ni10%Sn/CB _{sn}	23.791	61.680
20%Pd10%Ni10%Sn/MWCNT	19.711	52.615
20%Pd10%Ni10%Sn/MWCNT _{sn}	29.760	77.155

The evaluation the suitable composition of ethanol oxidation for use in direct ethanol fuel cells and support were completed.

CONCLUSION AND RECOMMENDATIONS

Conclusion

This research aimed to synthesis and investigation the most suitable composition of those metals alloy catalyst with Pd main metal compound and effect of type of carbon supports and functionalization on the catalyst performance which also included physical and electrochemical characterization. The preparation of all catalysts was carried out using a NaBH_4 reduction method which was a simple and versatile technique. The characterization of physical properties were x-ray diffraction, scanning electron microscopy, energy dispersive x-ray spectroscopy, transmission electron microscopy, surface area and porosity analyzer, chemisorption, x-ray photoelectron spectroscopy, Raman imaging microscopy, Fourier transform Infrared Spectroscopy, thermogravimetric analysis. The electrochemical characterization consisted of activity, durability, CO-tolerance, and electrochemical surface area (ESA) of catalysts. The conclusion can be divided into 2 parts that were the evaluation of catalyst compositions and the evaluation of catalyst on various carbon based supports.

In case of the evaluation of catalyst compositions, the preparation of different catalyst composition was carried out as followed; 20%Pd/CB, 20%Pd20%Ni/CB, 20%Pd20%Sn/CB, 20%Pd5%Ni15%Sn/CB, 20%Pd10%Ni10%Sn/CB and 20%Pd15%Ni5%Sn/CB. The XRD results of ternary catalytic systems presented that the crystalline of Pd, $\text{Ni}(\text{OH})_2$ and SnO_2 were achieved. The SEM results confirmed the uniformly surface morphology. The EDX results verified the weight percentage of metal content which agreed very nearly with the desired catalyst compositions. The TEM results showed good dispersion for the low Ni content catalysts and the average particle size in the range of 5.46-10.56 nm. Among various ternary catalytic systems, it was found that the activity of 20%Pd10%Ni10%Sn/CB exhibited the maximum current density of 146 mA cm^{-2} in a mixture of 1 M KOH and 1 M ethanol solution system using CV analysis and the maximum ESA of all those catalyst composition.

The durability and CO stripping of catalysts showed that the high Ni containing catalysts showed higher toward durability and CO tolerance than that of low Ni containing catalysts. The CO chemisorption showed well Pd metal dispersion for 20%Pd10%Ni10%Sn/CB and the poor dispersion for 20%Pd20%Sn/CB.

In case of the evaluation of catalyst on various carbon based supports, the preparation of 20%Pd10%Ni10%Sn on CB, CB_{sn}, MWCNT and MWCNT_{sn} was prepared. The TGA results showed that the functional group on the support was achieved. And the all degradation of functionalized support was at the lower temperature than that of the non-functionalized one. This measured that the better chemical stability was achieved after functionalization. The BET results revealed after support functionalization that the S_{BET} was reduced due to the changed of acid treatment the surface morphology and agreeing with the Raman results. The I_D/I_G ratio was increased for MWCNT_{sn} due to it the occurrence of the defect on the surface of support. The TEM results showed good dispersion for catalyst on MWCNT_{sn} support and the average particle size in the range of 6.08-6.65 nm. The CO chemisorption showed the good Pd metal dispersion on CB_{sn} and MWCNT_{sn}. The XRD results presented the crystalline of Pd, Ni(OH)₂ and SnO₂ The EDX results have verified the weight percentage of metal which agreed very nearly with the desired catalyst compositions. Among various ternary catalytic systems, it was found that the activity of 20%Pd10%Ni10%Sn/MWCNT_{sn} exhibited the maximum current density of 291 mA cm⁻² in a mixture of 1 M KOH and 1 M ethanol solution system and the maximum ESA of all those of catalyst on various carbon supports. The types and functionalization of support rarely affected on CO tolerance and durability of catalyst when compared with the compositions changing.

Recommendations

1. Carbon support should be preheated at 110 °C for 4 hr before synthesis in order to remove water and some substances which it may block opportunity the of metal to attach on the supports.

2. The suitable volume of NaBH_4 solution for synthesis should be calculated to obtain pH 8-9. The NaBH_4 solution is important in the reduction process in catalyst synthesis step. If the pH was in the acid range from the acid by-product in the reduction reaction, the reaction can't be completed.

3. The surface area of catalyst on the glassy carbon paper electrode for using as a working electrode in CV test is the most important factor which must be fixed equally in all experiment. If it has some error, it will significantly affect to electrochemical results.

4. The weight of catalyst on working electrode used is small amount so it is difficult to weight. It should be replaced by the calculation of volume dropping and then conversion to weight of catalyst. This is more accurate than weighting.

LITERATURE CITED

- Achmad, F., S.K. Kamarudin, W.R.W. Daud and E.H. Majlan. 2011. Passive Direct Methanol Fuel Cells for Portable Electronic Devices. **Applied Energy**. 88(5): 1681-1689.
- Ahn, S.H., I. Choi, O.J. Kwon and J.J. Kim. 2012. One-Step Co-Electrodeposition of Pt–Ru Electrocatalysts on Carbon Paper for Direct Methanol Fuel Cell. **Chemical Engineering Journal**. 181–182(1): 276-280.
- An, H., L. Pan, H. Cui, B. Li, D. Zhou, J. Zhai and Q. Li. 2013a. Synthesis and Performance of Palladium-Based Catalysts for Methanol and Ethanol Oxidation in Alkaline Fuel Cells. **Electrochimica Acta**. 102(1): 79-87.
- An, H., H. Cui, D. Zhou, D. Tao, B. Li, J. Zhai and Q. Li. 2013b. Synthesis and Performance of Pd/Sno₂–Tio₂/Mwent Catalysts for Direct Formic Acid Fuel Cell Application. **Electrochimica Acta**. 92(1): 176-182.
- An, L. and T.S. Zhao. 2011. An Alkaline Direct Ethanol Fuel Cell with a Cation Exchange Membrane. **Energy & Environmental Science**. 4(6): 2213.
- An, L., T.S. Zhao and J.B. Xu. 2011a. A Bi-Functional Cathode Structure for Alkaline-Acid Direct Ethanol Fuel Cells. **International Journal of Hydrogen Energy**. 36(20): 13089-13095.
- An, L., T.S. Zhao, R. Chen and Q.X. Wu. 2011b. A Novel Direct Ethanol Fuel Cell with High Power Density. **Journal of Power Sources**. 196(15): 6219-6222.
- An, L., T.S. Zhao, Q.X. Wu and L. Zeng. 2012. Comparison of Different Types of Membrane in Alkaline Direct Ethanol Fuel Cells. **International Journal of Hydrogen Energy**. 37(19): 14536-14542.

- Andújar, J.M. and F. Segura. 2009. Fuel Cells: History and Updating. A Walk Along Two Centuries. **Renewable and Sustainable Energy Reviews**. 13(9): 2309-2322.
- Anonymous. 2007. Subject Index, p. 879-892. *In* C. G. Zoski, eds. **Handbook of Electrochemistry**. Elsevier, Amsterdam.
- Anonymous. (2013) **Electrocatalysis in Fuel Cells-a Non- and Low- Platinum Approach**, in: M. Shao (Ed.), Springer-Verlag London South Windsor, CT, USA.
- Antolini, E. and E.R. Gonzalez. 2010. Alkaline Direct Alcohol Fuel Cells. **Journal of Power Sources**. 195(11): 3431-3450.
- Aranda, D.A.G. and M. Schmal. 1997. Ligand and Geometric Effects on Pt/Nb₂O₅ and Pt-Sn/Nb₂O₅ catalysts. **Journal of Catalysis**. 171(2): 398-405.
- Bagchi, J. and S. Bhattacharya. 2007. Electrocatalytic Activity of Binary Palladium Ruthenium Anode Catalyst on Ni-Support for Ethanol Alkaline Fuel Cells. **Transition Metal Chemistry**. 32(1): 47-55.
- Bagchi, J. and S. Bhattacharya. 2008. Studies of the Electrocatalytic Activity of Binary Palladium Ruthenium Anode Catalyst on Ni Support for Ethanol Alkaline Fuel Cells. **Transition Metal Chemistry**. 33(1): 113-120.
- Bambagioni, V., C. Bianchini, A. Marchionni, J. Filippi, F. Vizza, J. Teddy, P. Serp and M. Zhiani. 2009. Pd and Pt-Ru Anode Electrocatalysts Supported on Multi-Walled Carbon Nanotubes and Their Use in Passive and Active Direct Alcohol Fuel Cells with an Anion-Exchange Membrane (Alcohol=Methanol, Ethanol, Glycerol). **Journal of Power Sources**. 190(2): 241-251.

Bard, A.J. and L.R. Faulkner. 2000. **Electrochemical Methods: Fundamentals and Applications**. 2nd. John Wiley & Sons, Inc., New York.

Bessel, C.A., K. Laubernds, N.M. Rodriguez and R.T.K. Baker. 2001. Graphite Nanofibers as an Electrode for Fuel Cell Applications. **The Journal of Physical Chemistry B**. 105(6): 1115-1118.

Cai, J., Y. Huang and Y. Guo. 2013. Bi-Modified Pd/C Catalyst Via Irreversible Adsorption and Its Catalytic Activity for Ethanol Oxidation in Alkaline Medium. **Electrochimica Acta**. 99(22-29).

Castro, J.C., R.M. Antoniassi, R.R. Dias, M. Linardi, E.V. Spinacé and A.O. Neto. 2012. Preparation of Ptsnrh/C-Sb2o5·Sno2 Electrocatalysts by an Alcohol Reduction Process for Direct Ethanol Fuel Cell. **Ionics**. 18(8): 781-786.

Chang, H., S.H. Joo and C. Pak. 2007. Synthesis and Characterization of Mesoporous Carbon for Fuel Cell Applications. **Journal of Materials Chemistry**. 17(30): 3078-3088.

Chu, Y.H. and Y.G. Shul. 2010. Combinatorial Investigation of Pt–Ru–Sn Alloys as an Anode Electrocatalysts for Direct Alcohol Fuel Cells. **International Journal of Hydrogen Energy**. 35(20): 11261-11270.

Corbo, P., F. Migliardini and O. Veneri. 2007. Experimental Analysis and Management Issues of a Hydrogen Fuel Cell System for Stationary and Mobile Application. **Energy Conversion and Management**. 48(8): 2365-2374.

Dang, Z.-M., L. Wang and L.-P. Zhang. 2006. Surface Functionalization of Multiwalled Carbon Nanotube with Trifluorophenyl. **Journal of Nanomaterials**. 2006(1-5).

- Daugaard, A.E., K. Jankova, J.M.R. Marín, J. Bøgelund and S. Hvilsted. 2012. Poly(Ethylene-Co-Butylene) Functionalized Multi Walled Carbon Nanotubes Applied in Polypropylene Nanocomposites. **European Polymer Journal**. 48(4): 743-750.
- David, H., T. Reginald, B. Steve and J. Amanda. 2014. **Hydrogen for Fuel Cell Electric Vehicles**. Available Source: <http://www.renewableenergyfocus.com/blog/2013/9/19/hydrogen-for-fuel-cell-electric-vehicles/1006.aspx>, September 12, 2014.
- de Miguel, S.R., J.I. Vilella, E.L. Jablonski, O.A. Scelza, C. Salinas-Martinez de Lecea and A. Linares-Solano. 2002. Preparation of Pt Catalysts Supported on Activated Carbon Felts (Acf). **Applied Catalysis A: General**. 232(1–2): 237-246.
- Douglas A., S., H. F. James and N. Timothy A. 2007. **Principles of Instrumental Analysis 5th**. Saunders College Publishing, Philadelphia.
- Ferdinand, v.S. 1988. Carbon Materials. Carbon—Electrochemical and Physicochemical Properties. By K. Kinoshita. Wiley, New York 1988. Xiii, 533 Pp., Bound, £ 65.00.—Isbn 0-471-84802-6. **Angewandte Chemie**. 100(9): 1260-1261.
- Fung, A.W.P., G.A.M. Reynolds, Z.H. Wang, M.S. Dresselhaus, G. Dresselhaus and R.W. Pekala. 1995. Relationship between Particle Size and Magnetoresistance in Carbon Aerogels Prepared under Different Catalyst Conditions. **Journal of Non-Crystalline Solids**. 186(0): 200-208.
- Geeter, E.D., M. Mangan, S. Spaepen, W. Stinissen and G. Vennekens. 1999. Alkaline Fuel Cells for Road Traction. **Journal of Power Sources** 80(207-212).

- Gribov, E.N., A.Y. Zinovieva, I.N. Voropaev, P.A. Simonov, A.V. Romanenko and A.G. Okunev. 2012. Activities of Pt/Sibunit-1562 Catalysts in the Orr in Pemfc: Effect of Pt Content and Pt Load at Cathode. **International Journal of Hydrogen Energy**. 37(16): 11894-11903.
- Heinzel, A., F. Mahlendorf and C. Jansen. 2009. Fuel Cells – Proton-Exchange Membrane Fuel Cells | Bipolar Plates, p. 810-816. *In* J. Garche, eds. **Encyclopedia of Electrochemical Power Sources**. Elsevier, Amsterdam.
- Hsieh, C.-T., Y.-Y. Liu, W.-Y. Chen and Y.-H. Hsieh. 2011. Electrochemical Activity and Durability of Pt–Sn Alloys on Carbon-Based Electrodes Prepared by Microwave-Assisted Synthesis. **International Journal of Hydrogen Energy**. 36(24): 15766-15774.
- Hu, H., B. Zhao, M.E. Itkis and R.C. Haddon. 2003. Nitric Acid Purification of Single-Walled Carbon Nanotubes. **The Journal of Physical Chemistry B**. 107(50): 13838-13842.
- Huang, H.X., S.X. Chen and C.e. Yuan. 2008a. Platinum Nanoparticles Supported on Activated Carbon Fiber as Catalyst for Methanol Oxidation. **Journal of Power Sources**. 175(1): 166-174.
- Huang, Y., X. Zhou, J. Liao, C. Liu, T. Lu and W. Xing. 2008b. Preparation of Pd/C Catalyst for Formic Acid Oxidation Using a Novel Colloid Method. **Electrochemistry Communications**. 10(4): 621-624.
- Inoue, S., N. Ichikuni, T. Suzuki, T. Uematsu and K. Kaneko. 1998. Capillary Condensation of N₂ on Multiwall Carbon Nanotubes. **Phys. Chem.** 102(4689-4692).

- Jha, N., P. Ramesh, E. Bekyarova, X. Tian, F. Wang, M.E. Itkis and R.C. Haddon. 2013. Functionalized Single-Walled Carbon Nanotube-Based Fuel Cell Benchmarked against Us Doe 2017 Technical Targets. **Scientific Reports**. 3(2257).
- Jin, C., X. Sun, Z. Chen and R. Dong. 2012. Electrocatalytic Activity of Pd₂Ni/C Catalysts for Allyl Alcohol Oxidation in Alkaline Solution. **Materials Chemistry and Physics**. 135(2–3): 433-437.
- Jun, S., S.H. Joo, R. Ryoo, M. Kruk, M. Jaroniec, Z. Liu, T. Ohsuna and O. Terasaki. 2000. Synthesis of New, Nanoporous Carbon with Hexagonally Ordered Mesoporous Structure. **Journal of the American Chemical Society**. 122(43): 10712-10713.
- Kissinger, P.T. and W.R. Heineman. 1983. Cyclic Voltammetry. **Journal of Chemical Education**. 60(9): 702.
- Komarow, W.S. 1997. Adsorbenty I Ich Svojstva. **Nauka i Technika**. Minsk(
- Ksar, F., L. Ramos, B. Keita, L. Nadjo, P. Beaunier and H. Remita. 2009. Bimetallic Palladium-Gold Nanostructures: Application in Ethanol Oxidation. **Chemistry of Materials**. 21(15): 3677-3683.
- Lee, K.I., S.W. Lee, M.S. Park and C.N. Chu. 2010. The Development of Air-Breathing Proton Exchange Membrane Fuel Cell (Pemfc) with a Cylindrical Configuration. **International Journal of Hydrogen Energy**. 35(21): 11844-11854.
- Li, R., Z. Wei, T. Huang and A. Yu. 2011. Ultrasonic-Assisted Synthesis of Pd–Ni Alloy Catalysts Supported on Multi-Walled Carbon Nanotubes for Formic Acid Electrooxidation. **Electrochimica Acta**. 56(19): 6860-6865.

- Li, W., C. Liang, J. Qiu, W. Zhou, H. Han, Z. Wei, G. Sun and Q. Xin. 2002. Carbon Nanotubes as Support for Cathode Catalyst of a Direct Methanol Fuel Cell. **Carbon**. 40(5): 791-794.
- Liu, J., J. Ye, C. Xu, S.P. Jiang and Y. Tong. 2007. Kinetics of Ethanol Electrooxidation at Pd Electrodeposited on Ti. **Electrochemistry Communications**. 9(9): 2334-2339.
- Liu, Z.-L., R. Huang, Y.-J. Deng, D.-H. Chen, L. Huang, Y.-R. Cai, Q. Wang, S.-P. Chen and S.-G. Sun. 2013. Catalyst of Pt Nanoparticles Loaded on Multi-Walled Carbon Nanotubes with High Activity Prepared by Electrodeposition without Supporting Electrolyte. **Electrochimica Acta**. 112(0): 919-926.
- Liu, Z., X. Zhang and L. Hong. 2009. Physical and Electrochemical Characterizations of Nanostructured Pd/C and PdNi/C Catalysts for Methanol Oxidation. **Electrochemistry Communications**. 11(4): 925-928.
- Lowell, S., J.E. Shields, M.A. Thomas and M. Thommes. (2004) **Characterization of Porous Solids and Powders: Surface Area, Pore Size and Density**, Springer Netherlands.
- Lu, J., S. Lu, D. Wang, M. Yang, Z. Liu, C. Xu and S.P. Jiang. 2009. Nano-Structured Pd_xPt_{1-x}/Ti Anodes Prepared by Electrodeposition for Alcohol Electrooxidation. **Electrochimica Acta**. 54(23): 5486-5491.
- Lucy, F. 2003. **Fuel for Thought on Cars of the Future**. Available Source: http://www.scientific-computing.com/features/feature.php?feature_id=126, September 18, 2014.
- Lutz, A.E., R.S. Larson and J.O. Keller. 2002. Thermodynamic Comparison of Fuel Cells to the Carnot Cycle. **International Journal of Hydrogen Energy**. 27(1103-1111).

- Maiyalagan, T., B. Viswanathan and U.V. Varadaraju. 2005. Nitrogen Containing Carbon Nanotubes as Supports for Pt – Alternate Anodes for Fuel Cell Applications. **Electrochemistry Communications**. 7(9): 905-912.
- Marques, P., N.F.P. Ribeiro, M. Schmal, D.A.G. Aranda and M.M.V.M. Souza. 2006. Selective Co Oxidation in the Presence of H₂ over Pt and Pt-Sn Catalysts Supported on Niobia. **Journal of Power Sources**. 158(1): 504-508.
- Marshall, M.W., S. Popa-Nita and J.G. Shapter. 2006. Measurement of Functionalised Carbon Nanotube Carboxylic Acid Groups Using a Simple Chemical Process. **Carbon**. 44(7): 1137-1141.
- McBreen, J., H. Olender, S. Srinivasan and K.V. Kordesch. 1981. Carbon Supports for Phosphoric Acid Fuel Cell Electrocatalysts: Alternative Materials and Methods of Evaluation. **Journal of Applied Electrochemistry**. 11(6): 787-796.
- Mekhilef, S., R. Saidur and A. Safari. 2012. Comparative Study of Different Fuel Cell Technologies. **Renewable and Sustainable Energy Reviews**. 16(1): 981-989.
- Meng, L., C. Fu and Q. Lu. 2009. Advanced Technology for Functionalization of Carbon Nanotubes. **Progress in Natural Science**. 19(7): 801-810.
- Merino-Jimenez, I., M.J. Janik, C. Ponce de Leon and F.C. Walsh. 2014. Pd–Ir Alloy as an Anode Material for Borohydride Oxidation. **Journal of Power Sources**. 269(0): 498-508.

- Modibedi, R.M., T. Masombuka and M.K. Mathe. 2011. Carbon Supported Pd–Sn and Pd–Ru–Sn Nanocatalysts for Ethanol Electro-Oxidation in Alkaline Medium. **International Journal of Hydrogen Energy**. 36(8): 4664-4672.
- Moreno-Castilla, C. and F.J. Maldonado-Hódar. 2005. Carbon Aerogels for Catalysis Applications: An Overview. **Carbon**. 43(3): 455-465.
- Neto, A.O., M.M. Tusi, N.S. de Oliveira Polanco, S.G. da Silva, M. Coelho dos Santos and E.V. Spinacé. 2011. Pd/C Electrocatalysts for Ethanol Electro-Oxidation in Alkaline Medium. **International Journal of Hydrogen Energy**. 36(17): 10522-10526.
- Nguyen, S.T., D.S. Ling Tan, J.-M. Lee, S.H. Chan, J.Y. Wang and X. Wang. 2011. Tb Promoted Pd/C Catalysts for the Electrooxidation of Ethanol in Alkaline Media. **International Journal of Hydrogen Energy**. 36(16): 9645-9652.
- Nie, M., H. Tang, Z. Wei, S.P. Jiang and P.K. Shen. 2007. Highly Efficient AuPd–W/C Electrocatalyst for Ethanol Oxidation. **Electrochemistry Communications**. 9(9): 2375-2379.
- Osorio, A.G., I.C.L. Silveira, V.L. Bueno and C.P. Bergmann. 2008. H₂SO₄/HNO₃/HCl—Functionalization and Its Effect on Dispersion of Carbon Nanotubes in Aqueous Media. **Applied Surface Science**. 255(5): 2485-2489.
- Park, K.-W., J.-H. Choi, S.-A. Lee, C. Pak, H. Chang and Y.-E. Sung. 2004. PtRu Nanoparticle Electrocatalyst for Methanol Electrooxidation in Direct Methanol Fuel Cell. **Journal of Catalysis**. 224(2): 236-242.
- Peighambaroust, S.J., S. Rowshanzamir and M. Amjadi. 2010. Review of the Proton Exchange Membranes for Fuel Cell Applications. **International Journal of Hydrogen Energy**. 35(17): 9349-9384.

- Peter, T.K. and H. William R. 1996. **Laboratory Techniques in Electroanalytical Chemistry**. 2nd. Marcel Dekker, Inc., New York.
- Pimenta, M.A., G. Dresselhaus, M.S. Dresselhaus, L.G. Cancado, A. Jorio and R. Saito. 2007. Studying Disorder in Graphite-Based Systems by Raman Spectroscopy. **Physical Chemistry Chemical Physics**. 9(11): 1276-1291.
- Puskás, R., A. Sápi, A. Kukovecz and Z. Kónya. 2012. Comparison of Nanoscaled Palladium Catalysts Supported on Various Carbon Allotropes. **Topics in Catalysis**. 55(11-13): 865-872.
- Qi, Y., B. Huang and J. Luo. 2008. 1-D Dynamic Modeling of Sofc with Analytical Solution for Reacting Gas-Flow Problem. **AIChE Journal**. 54(6): 1537-1553.
- Qi, Z., H. Geng, X. Wang, C. Zhao, H. Ji, C. Zhang, J. Xu and Z. Zhang. 2011. Novel Nanocrystalline Pd₉₀Ni₁₀ Alloy Catalyst for Methanol and Ethanol Electro-Oxidation in Alkaline Media. **Journal of Power Sources**. 196(14): 5823-5828.
- Qingfeng Yi, F.N., Lizhi Sun. 2011. Fabrication of Novel Porous Pd Particles and Their Electroactivity Towards Ethanol Oxidation in Alkaline Media. **fuel** 90(2617-2623).
- Ramulifho, T., K.I. Ozoemena, R.M. Modibedi, C.J. Jafta and M.K. Mathe. 2012. Fast Microwave-Assisted Solvothermal Synthesis of Metal Nanoparticles (Pd, Ni, Sn) Supported on Sulfonated Mwcnts: Pd-Based Bimetallic Catalysts for Ethanol Oxidation in Alkaline Medium. **Electrochimica Acta**. 59(310-320).
- Rao, C.V. and B. Viswanathan. 2010. Carbon Supported Pd–Co–Mo Alloy as an Alternative to Pt for Oxygen Reduction in Direct Ethanol Fuel Cells. **Electrochimica Acta**. 55(8): 3002-3007.

- Rao, V., P.A. Simonov, E.R. Savinova, G.V. Plaksin, S.V. Cherepanova, G.N. Kryukova and U. Stimming. 2005. The Influence of Carbon Support Porosity on the Activity of PtRu/Sibunit Anode Catalysts for Methanol Oxidation. **Journal of Power Sources**. 145(2): 178-187.
- Reeve, R.W. 2002. **Update on Status of Direct Methanol Fuel Cells**. Harwell Laboratory, Energy Technology Support Unit, Fuel Cells Programme.
- Ribadeneira, E. and B.A. Hoyos. 2008. Evaluation of Pt–Ru–Ni and Pt–Sn–Ni Catalysts as Anodes in Direct Ethanol Fuel Cells. **Journal of Power Sources**. 180(1): 238-242.
- Rike Y., Holia O.S., Yukie S., Tadahisa I. and J.-i. A. 2011. Analysis of Functional Group Sited on Multi-Wall Carbon Nanotube Surface. **The Open Materials Science**. 5(1): 242-247.
- Robert, R., G. Jennifer and C. Sandra. 2014. **Fuel Cells 2000 Resources**. Available Source: <http://www.fuelcells.org/base.cgim?template=resources>, September 12, 2014.
- Roelofs, K., T. Hirth and T. Schiestel. 2011. Dihydrogenimidazole Modified Silica-Sulfonated Poly(Ether Ether Ketone) Hybrid Materials as Electrolyte Membranes for Direct Ethanol Fuel Cells. **Material Science and Engineering**. 176(9): 727-735.
- Romanos, G.E., V. Likodimos, R.R.N. Marques, T.A. Steriotis, S.K. Papageorgiou, J.L. Faria, J.L. Figueiredo, A.M.T. Silva and P. Falaras. 2011. Controlling and Quantifying Oxygen Functionalities on Hydrothermally and Thermally Treated Single-Wall Carbon Nanotubes. **Journal of Physical Chemistry C**. 115(17): 8534-8546.

- Rose, R., J. Gangi and S. Curtin. 2014. **Types of Fuel Cells**. Available Source: http://www.fuelcells.org/base.cgim?template=types_of_fuel_cells, October 4, 2014.
- Serp, P. and J.L. Figueiredo. 2009. **Carbon Material for Catalyst**. John Wiley & Sons, Inc., New York.
- Shen, S.Y., T.S. Zhao and Q.X. Wu. 2012. Product Analysis of the Ethanol Oxidation Reaction on Palladium-Based Catalysts in an Anion-Exchange Membrane Fuel Cell Environment. **International Journal of Hydrogen Energy**. 37(1): 575-582.
- Shen, S.Y., T.S. Zhao, J.B. Xu and Y.S. Li. 2010. Synthesis of Pd/C Catalysts for the Oxidation of Ethanol in Alkaline Direct Ethanol Fuel Cells. **Journal of Power Sources**. 195(4): 1001-1006.
- Shieh, Y.-T., G.-L. Liu, H.-H. Wu and C.-C. Lee. 2007. Effects of Polarity and pH on the Solubility of Acid-Treated Carbon Nanotubes in Different Media. **Carbon**. 45(9): 1880-1890.
- Simões, M., S. Baranton and C. Coutanceau. 2010. Electro-Oxidation of Glycerol at Pd Based Nano-Catalysts for an Application in Alkaline Fuel Cells for Chemicals and Energy Cogeneration. **Applied Catalysis B: Environmental**. 93(3-4): 354-362.
- Sing, K.S.W., D.H. Everett, R.A.W. Haul, L. Moscou, R.A. Pierotti, J. Rouquerol and T. Siemieniewska. 2008. Reporting Physisorption Data for Gas/Solid Systems with Special Reference to the Determination of Surface Area and Porosity, p. 603-619. **Handbook of Heterogeneous Catalysis**. Wiley-VCH Verlag GmbH & Co. KGaA.

- Takamura, T. and K.i. Minamiyama. 2004. Anodic Oxidation of Methanol at Palladium Electrode in Alkaline Solution. **Journal of Electrochemical Society**. 185(333-335).
- Tarasevich, M.R., V.N. Titova, A.A. Yavich, N.V. Petrova and V.A. Bogdanovskaya. 2009. New Nonplatinum Electrocatalysts Based on Ru for the Direct Oxidation of Ethanol in an Alkaline Fuel Cell. **Russian Journal of Physical Chemistry A**. 83(11): 1850-1854.
- Tayal, J., B. Rawat and S. Basu. 2011. Bi-Metallic and Tri-Metallic Pt–Sn/C, Pt–Ir/C, Pt–Ir–Sn/C Catalysts for Electro-Oxidation of Ethanol in Direct Ethanol Fuel Cell. **International Journal of Hydrogen Energy**. 36(22): 14884-14897.
- Thanasilp, S. and M. Hunsom. 2010. Effect of Mea Fabrication Techniques on the Cell Performance of Pt–Pd/C Electrocatalyst for Oxygen Reduction in Pem Fuel Cell. **Fuel**. 89(12): 3847-3852.
- Uchida, M., Y. Aoyama, M. Tanabe, N. Yanagihara, N. Eda and A. Ohta. 1995. Influences of Both Carbon Supports and Heat-Treatment of Supported Catalyst on Electrochemical Oxidation of Methanol. **Journal of the Electrochemical Society**. 142(8): 2572-2576.
- University of Oxford, D.o.c. 2008. **Basic Operating Principles of the Sorptomatic 1990**. Available Source: <http://www.saf.chem.ox.ac.uk/operating-principles-3.aspx>, May 19, 2014.
- Vielstich, W., A. Lamm and H.A. Gasteiger. 2003. **Handbook of Fuel Cells: Fundamentals, Technology and Applications**. John Wiley and Sons, Inc., New York.

- Wang, X., Y. Tang, Y. Gao and T. Lu. 2008. Carbon-Supported Pd–Ir Catalyst as Anodic Catalyst in Direct Formic Acid Fuel Cell. **Journal of Power Sources**. 175(2): 784-788.
- Wang, Y., X. Wang and C.M. Li. 2010. Electrocatalysis of Pd–Co Supported on Carbon Black or Ball-Milled Carbon Nanotubes Towards Methanol Oxidation in Alkaline Media. **Applied Catalysis B: Environmental**. 99(1–2): 229-234.
- Watanabe, T. 2004. Chapter 7 - Database for the Microstructure of Plated Films, p. 632-633. In T. Watanabe, eds. **Nano Plating - Microstructure Formation Theory of Plated Films and a Database of Plated Films**. Elsevier, Oxford.
- Wei, Y.-C., C.-W. Liu, W.-D. Kang, C.-M. Lai, L.-D. Tsai and K.-W. Wang. 2011. Electro-Catalytic Activity Enhancement of Pd–Ni Electrocatalysts for the Ethanol Electro-Oxidation in Alkaline Medium: The Promotional Effect of CeO₂ Addition. **Journal of Electroanalytical Chemistry**. 660(1): 64-70.
- Wongyao, N., A. Therdthianwong and S. Therdthianwong. 2011. Performance of Direct Alcohol Fuel Cells Fed with Mixed Methanol/Ethanol Solutions. **Energy Conversion and Management**. 52(7): 2676-2681.
- Xiao, L., J.T. Lu, P.F. Liu, L. Zhuang, J.E. Yan, Y.G. Hu, B.W. Mao and C.J. Lin. 2005. Proton Diffusion Determination and Dual Structure Model for Nickel Hydroxide Based on Potential Step Measurements on Single Spherical Beads. **J. Phys. Chem.** B(109): 3860-3867.
- Xu, J.B., T.S. Zhao, S.Y. Shen and Y.S. Li. 2010. Stabilization of the Palladium Electrocatalyst with Alloyed Gold for Ethanol Oxidation. **International Journal of Hydrogen Energy**. 35(13): 6490-6500.

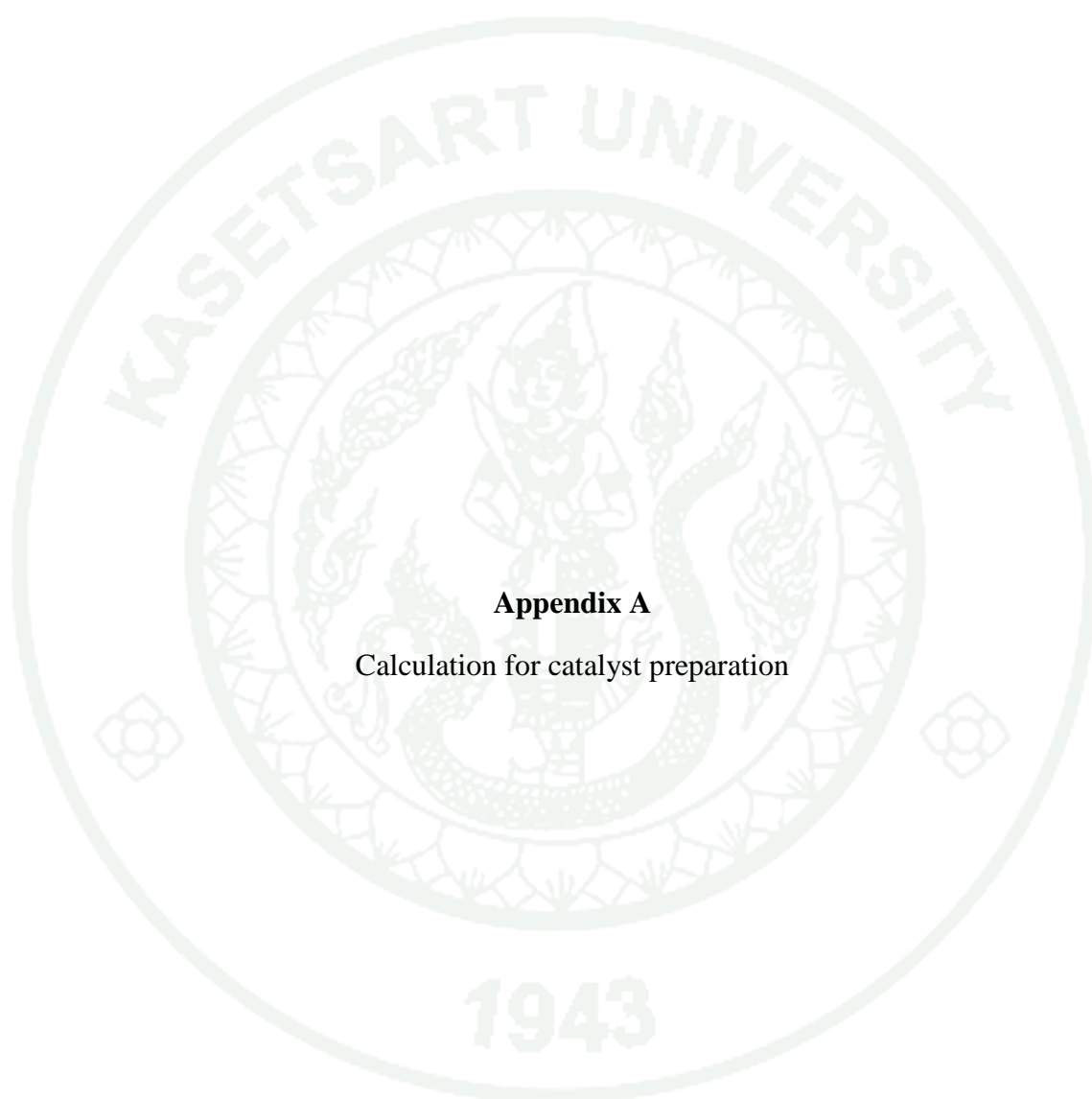
- Yang, Q.-H., P.-X. Hou, S. Bai, M.-Z. Wang and H.-M. Cheng. 2001. Adsorption and Capillarity of Nitrogen in Aggregated Multi-Walled Carbon Nanotubes. **Chemical Physics Letters**. 345(1-2): 18-24.
- Yang, S., X. Zhang, H. Mi and X. Ye. 2008. Pd Nanoparticles Supported on Functionalized Multi-Walled Carbon Nanotubes (Mwcnts) and Electrooxidation for Formic Acid. **Journal of Power Sources**. 175(1): 26-32.
- Yi, Q., F. Niu and L. Sun. 2011. Fabrication of Novel Porous Pd Particles and Their Electroactivity Towards Ethanol Oxidation in Alkaline Media. **Fuel**. 90(8): 2617-2623.
- Yuan, X.-Z., H. Li, S. Zhang, J. Martin and H. Wang. 2011. A Review of Polymer Electrolyte Membrane Fuel Cell Durability Test Protocols. **Journal of Power Sources**. 196(22): 9107-9116.
- Zaiton, A.M., A.M.S. Nur, A.B. Nor and S. Shafinaz. 2010. Role of Oxidant in Surface Modification of Carbon Nanotubes for Tyrosinase Immobilization **Journal of Fundamental Sciences**. 6(1): 51-55.
- Zhang, Z., L. Xin, K. Sun and W. Li. 2011. Pd-Ni Electrocatalysts for Efficient Ethanol Oxidation Reaction in Alkaline Electrolyte. **International Journal of Hydrogen Energy**. 36(20): 12686-12697.
- Zhao, Y., X. Yang, J. Tian, F. Wang and L. Zhan. 2010. Methanol Electro-oxidation on Ni@Pd Core-Shell Nanoparticles Supported on Multi-Walled Carbon Nanotubes in Alkaline Media. **International Journal of Hydrogen Energy**. 35(8): 3249-3257.

Zhou, W.J., S.Q. Song, W.Z. Li, Z.H. Zhou, G.Q. Sun, Q. Xin, S. Douvartzides and P. Tsiakaras. 2005. Direct Ethanol Fuel Cells Based on Ptsn Anodes: The Effect of Sn Content on the Fuel Cell Performance. **Journal of Power Sources**. 140(1): 50-58.





APPENDICES



Appendix A

Calculation for catalyst preparation

Calculation for catalyst preparation

The molecular weight of element

Pd = 106.42, Ni=58.6934, Sn=118.71, C=12.0107 and Cl=35.453

Appendix Table A1 Chemical properties of substance for catalyst synthesis.

Metal or Metal oxide	MW of metal	Metal Precursor	MW of Metal Precursor
Pd	106.42	PdCl ₂	177.326
Ni	58.6934	NiCl ₂	129.6
Sn	118.71	SnCl ₂	189.62
C	12.0107	C	12.0107

Calculation of catalyst prepared by reduction method

Preparation of catalysts by reduction method is shown as follows:

Precursors: PdCl₂, NiCl₂, SnCl₂

Support: Carbon black

Example: The calculation for preparation of 20% Pd, 20% Ni of catalyst with PdCl₂ and NiCl₂ as precursors

Based on 100 g of catalyst used, the composition of the catalyst will be as follows:

Pd	=	20		=	60	g
Ni	=	20				g
C	=	100-40	=	60		g

For 1 g of support

Palladium required = $1 \times (20/60)$ = 0.3333 g

Thus, Pd metal 0.33 g was prepared from PdCl₂

1mol of Pd metal 106.42 g in PdCl₂ 177.32 g

For 0.33 g of Pd metal

$$\text{Palladium chloride required} = 0.3333 \times (177.326/106.42) = 0.5554 \text{ g}$$

$$\text{Nickel required} = 1 \times (20/60) = 0.3333 \text{ g}$$

Thus, Nickel metal 0.3333 g was prepared from NiCl₂

1mol of Ni metal 58.6934 g in NiCl₂ 129.6 g

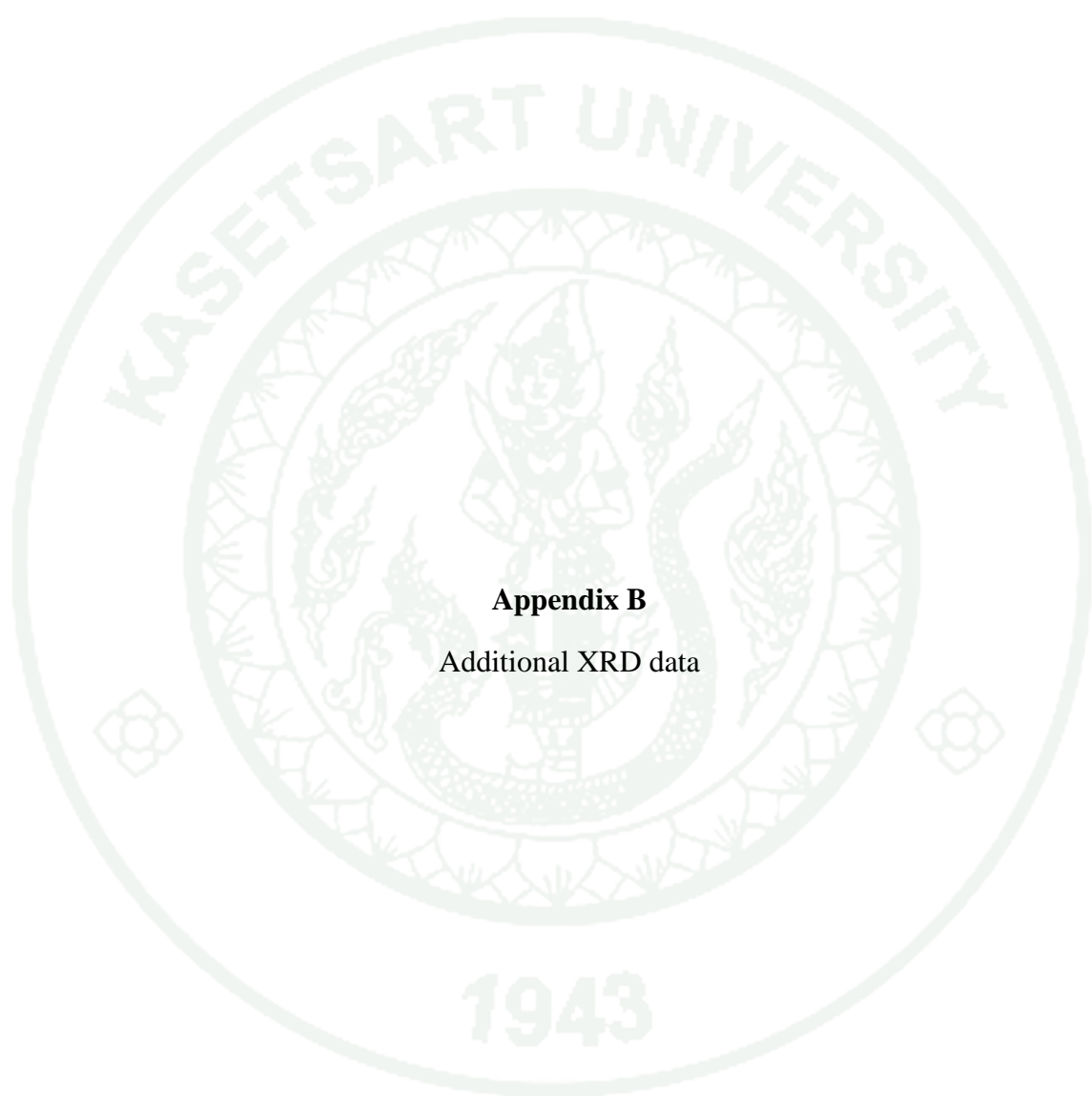
For 0.3333 g of Ni metal

$$\text{Palladium chloride required} = 0.3333 \times (129.6/58.6934) = 0.7360 \text{ g}$$

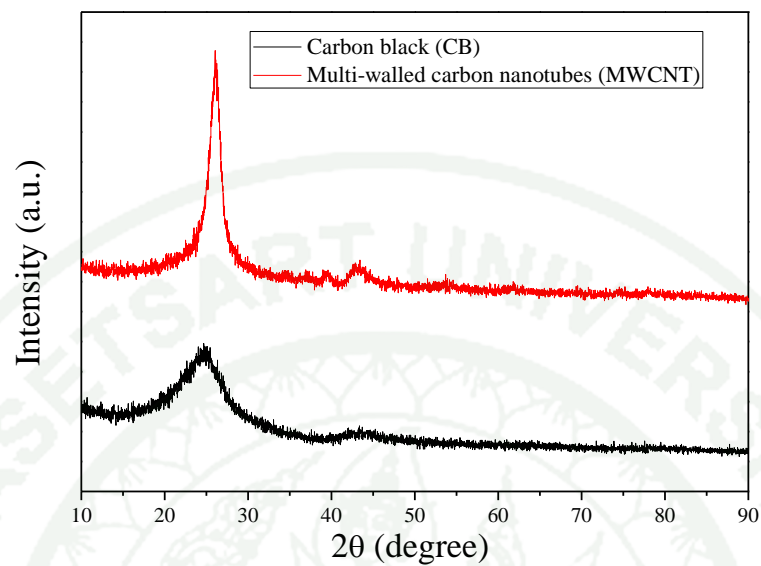
$$\text{Catalysts obtained} = 1 + (2 \times 0.3333) = 1.6666 \text{ g}$$

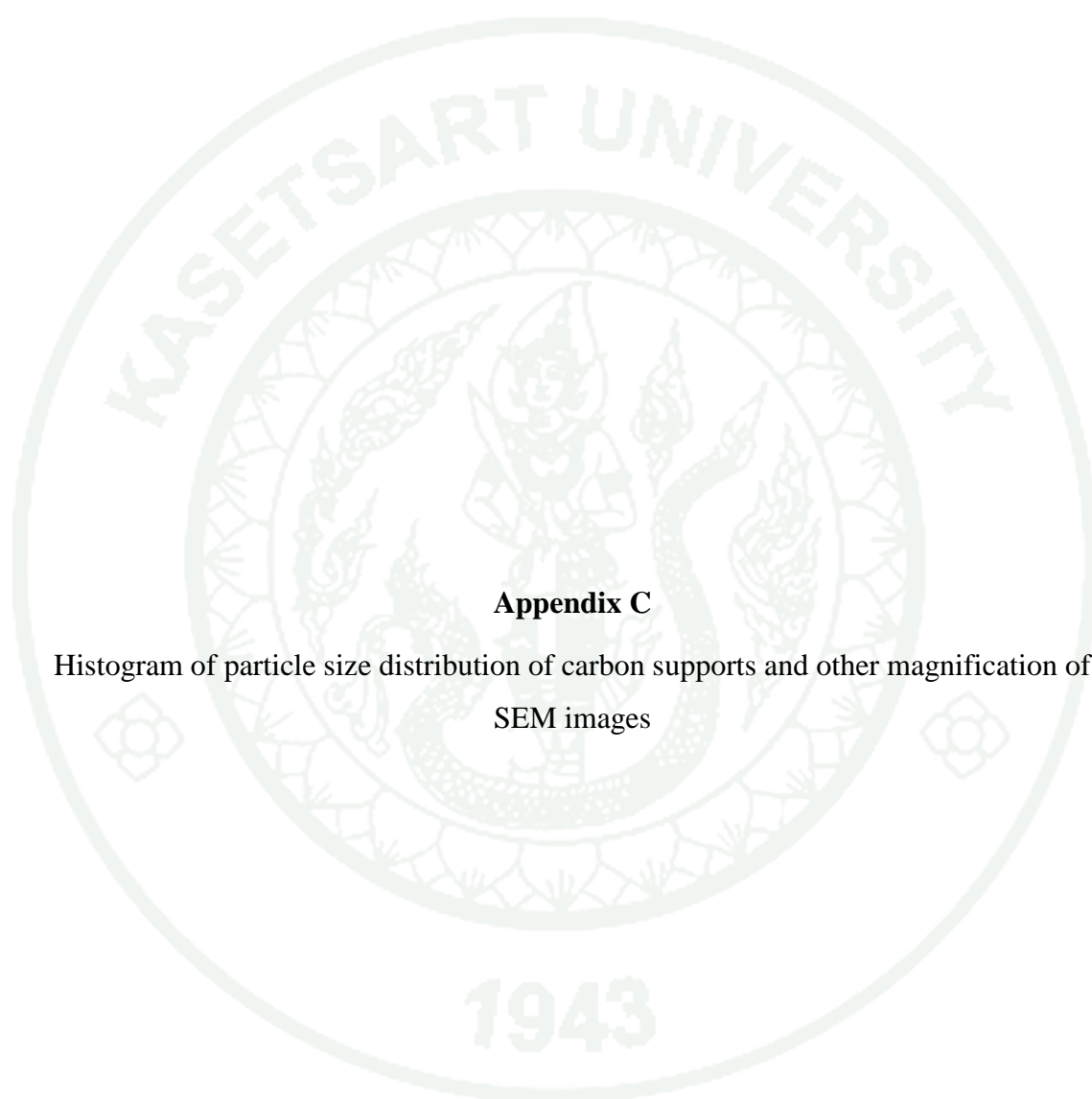
Appendix Table A2 Summary of the weight of substance for catalyst synthesis.

Catalysts prepared	Weight (g)			
	Pd	Ni	Sn	C
20%Pd/CB	0.5554	-	-	1
20%Pd20%Ni/CB	0.5554	0.736	-	1
20%Pd20%Sn/CB	0.5554	-	0.5323	1
20%Pd15%Ni5%Sn/CB	0.5554	0.5520	0.1331	1
20%Pd10%Ni10%Sn/CB	0.5554	0.3680	0.2662	1
20%Pd5%Ni15%Sn/CB	0.5554	0.1840	0.3993	1



Appendix B
Additional XRD data

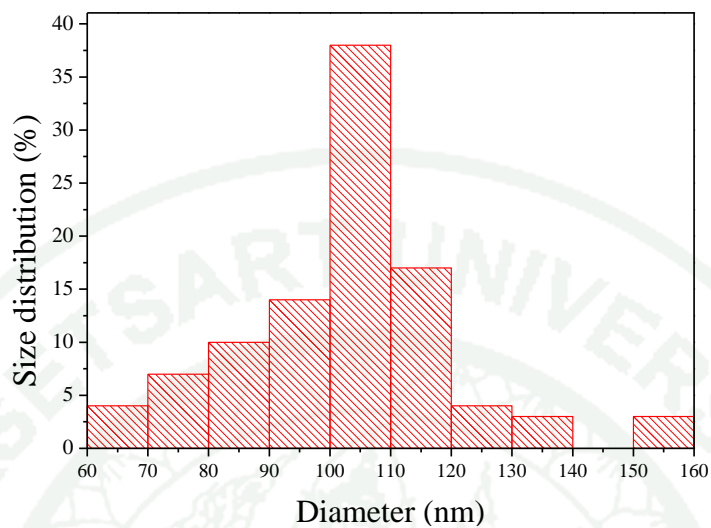
Additional XRD data**Appendix Figure B1** XRD patterns of carbon supports at 2θ between 10° to 90° .



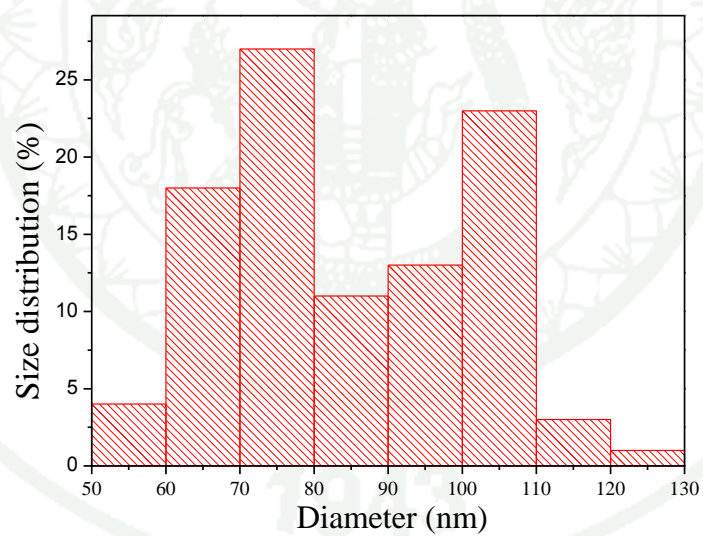
Appendix C

Histogram of particle size distribution of carbon supports and other magnification of SEM images

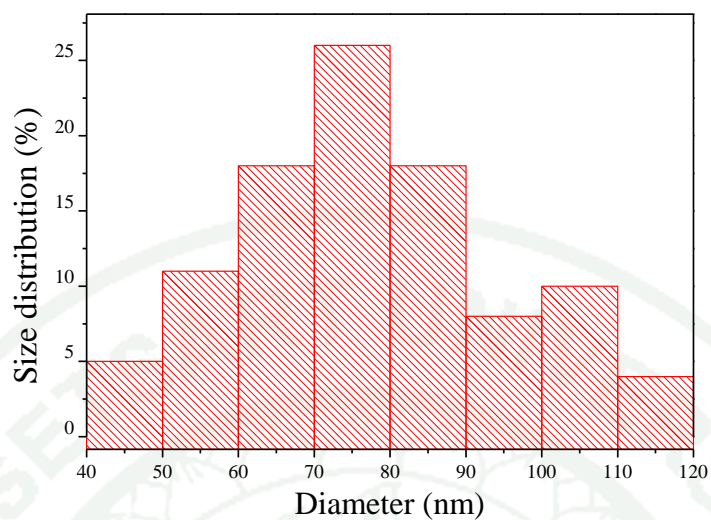
The size distribution of carbon supports



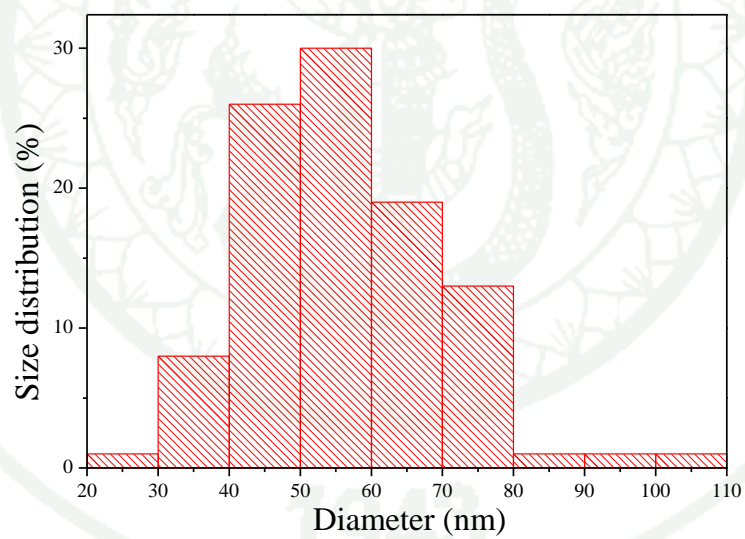
Appendix Figure C1 Histogram of particle size distribution of CB.



Appendix Figure C2 Histogram of particle size distribution of CB_{sn}.

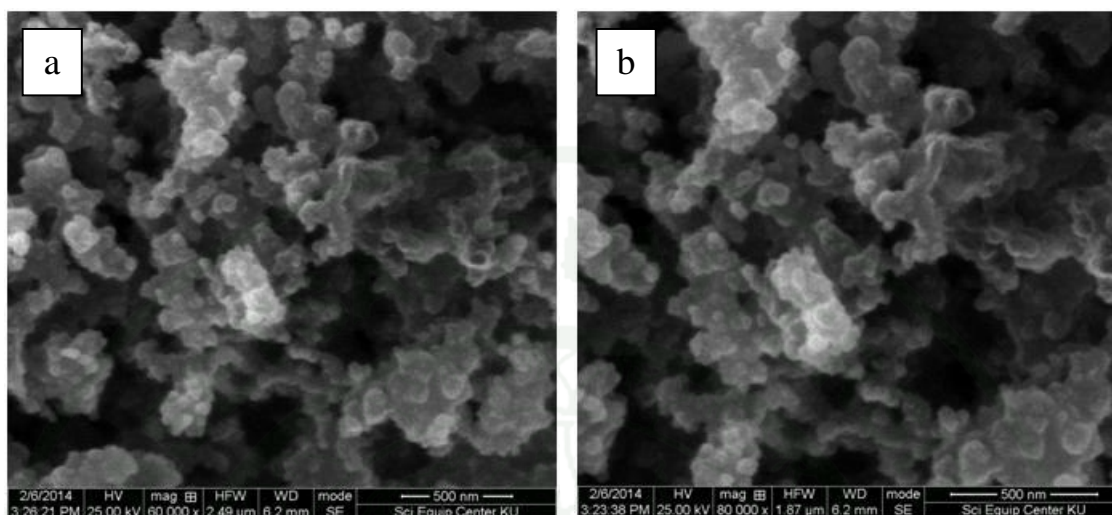


Appendix Figure C3 Histogram of tube diameter size distribution of MWCNT.

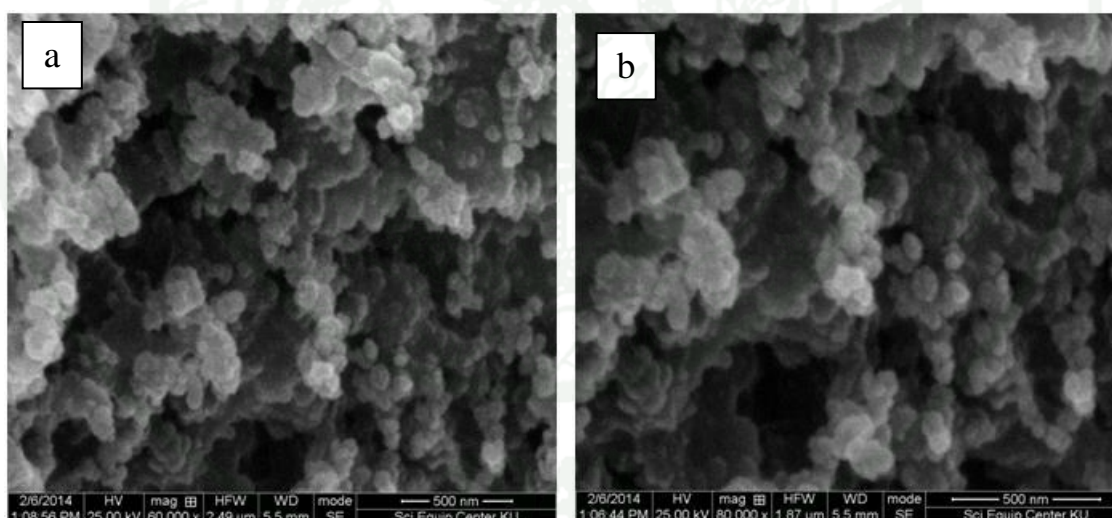


Appendix Figure C4 Histogram of tube diameter size distribution of MWCNT_{sn}.

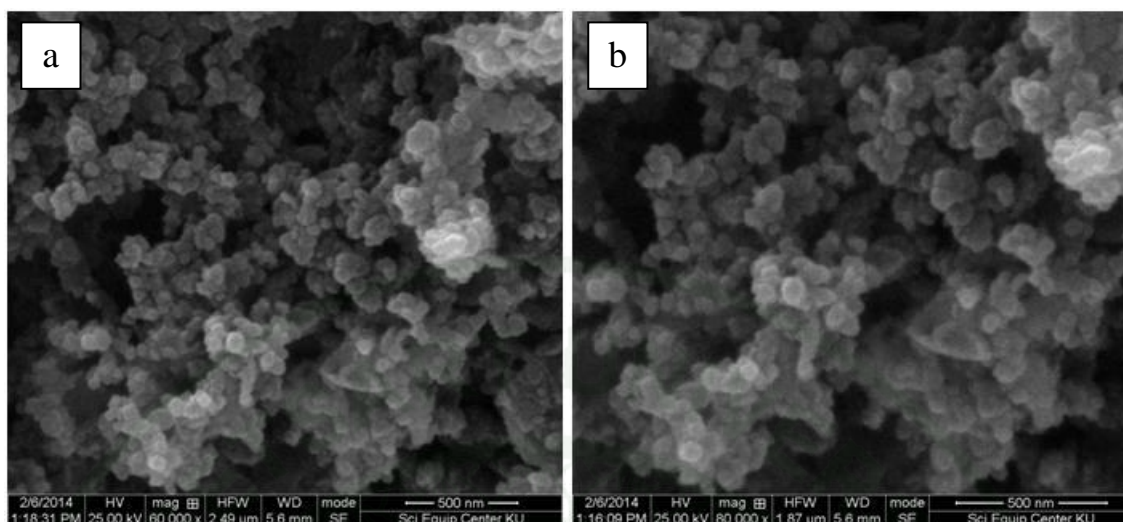
The SEM images of finding compositions and supports more magnification



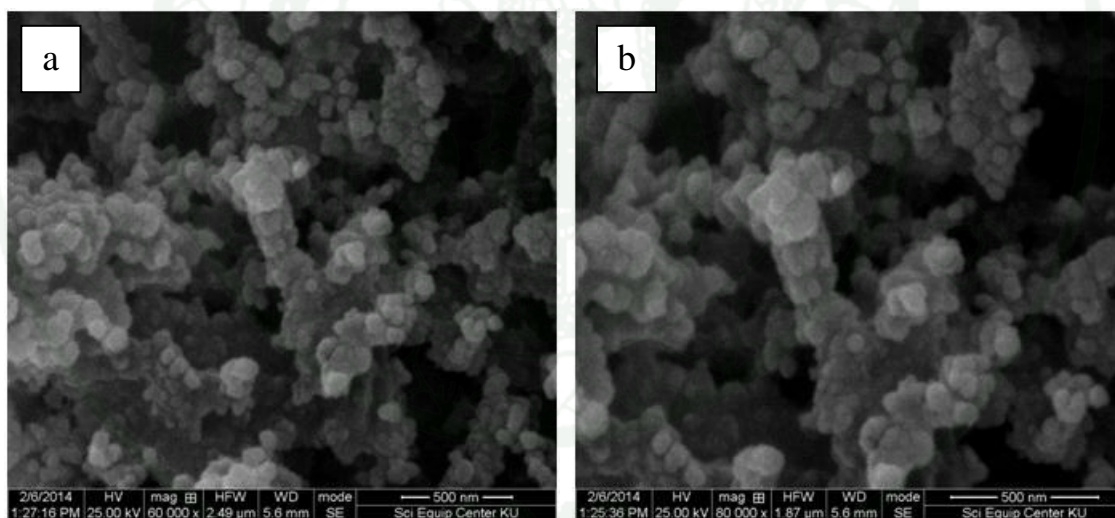
Appendix Figure C5 SEM images of 20%Pd/CB, (a) $\times 60,000$ and (b) $\times 80,000$.



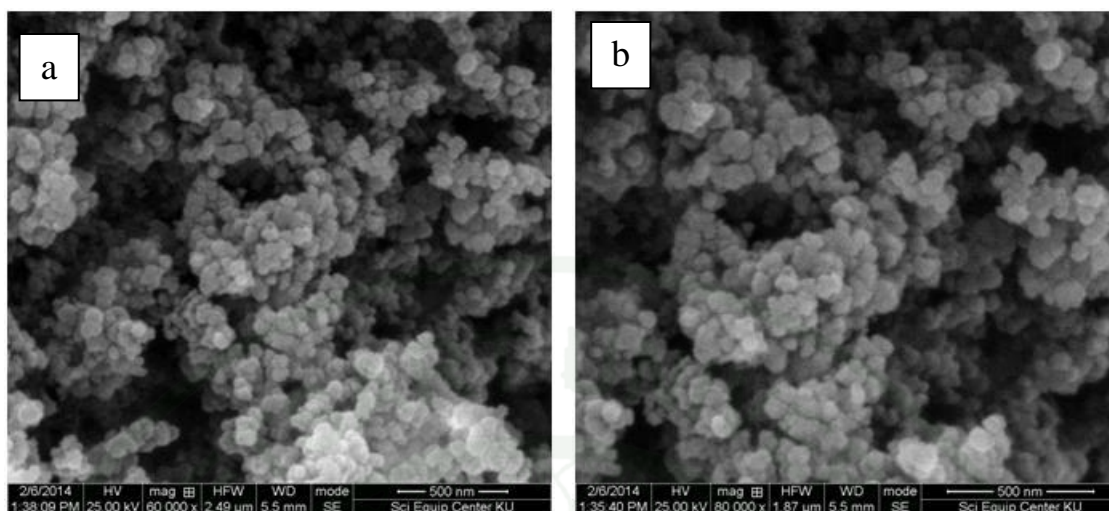
Appendix Figure C6 SEM images of 20%Pd20%Sn/CB, (a) $\times 60,000$ and (b) $\times 80,000$.



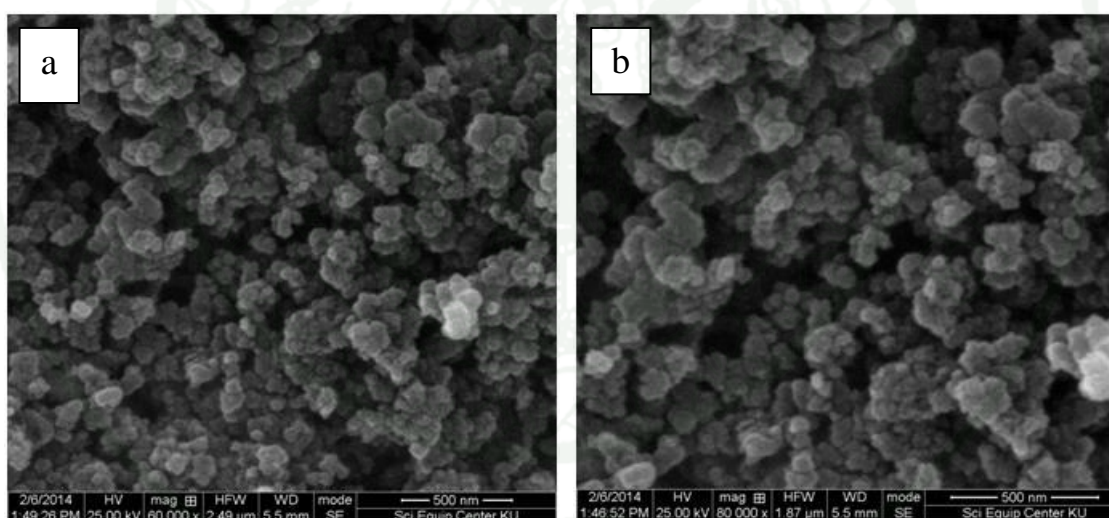
Appendix Figure C7 SEM images of 20%Pd20%Ni/CB, (a) $\times 60,000$ and (b) $\times 80,000$



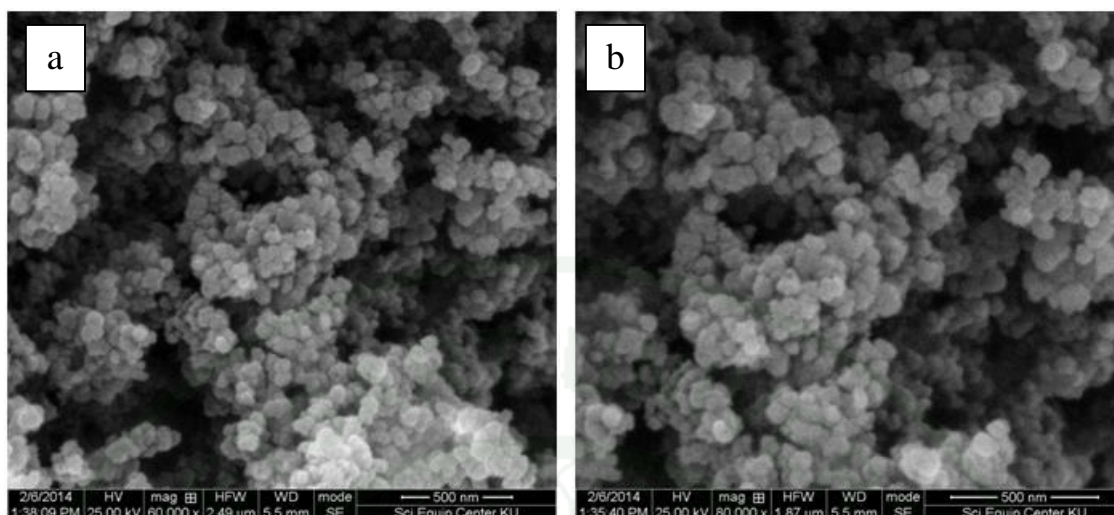
Appendix Figure C8 SEM images of 20%Pd5%Ni15%Sn/CB, (a) $\times 60,000$ and (b) $\times 80,000$.



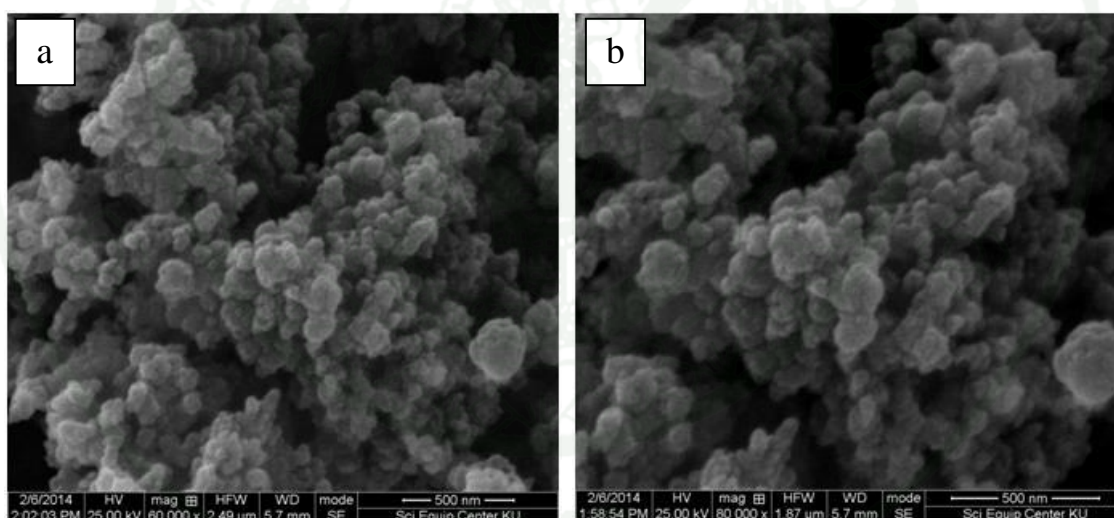
Appendix Figure C9 SEM images of 20%Pd10%Ni10%Sn/CB, (a) $\times 60,000$ and (b) $\times 80,000$.



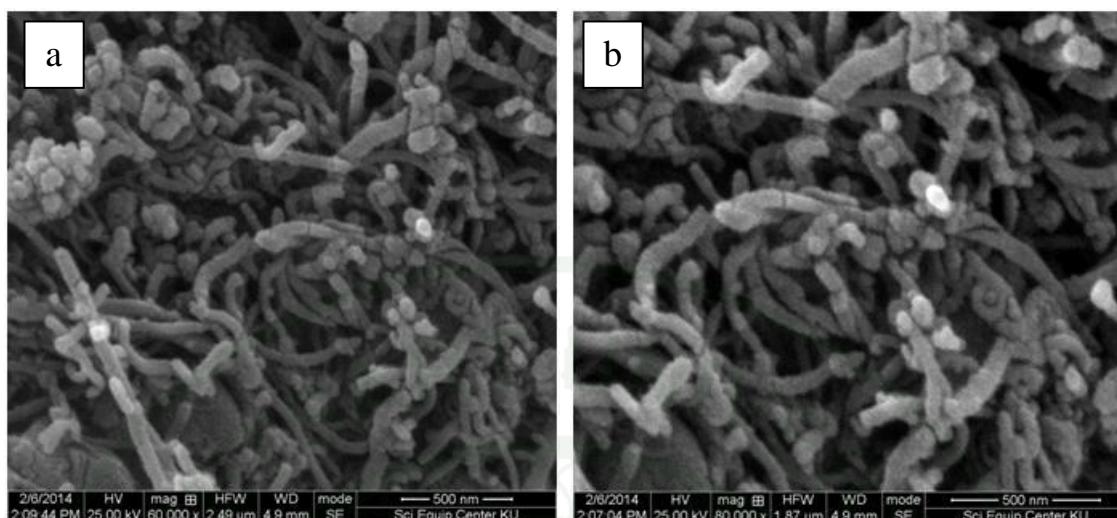
Appendix Figure C10 SEM images of 20%Pd15%Ni5%Sn/CB, (a) $\times 60,000$ and (b) $\times 80,000$.



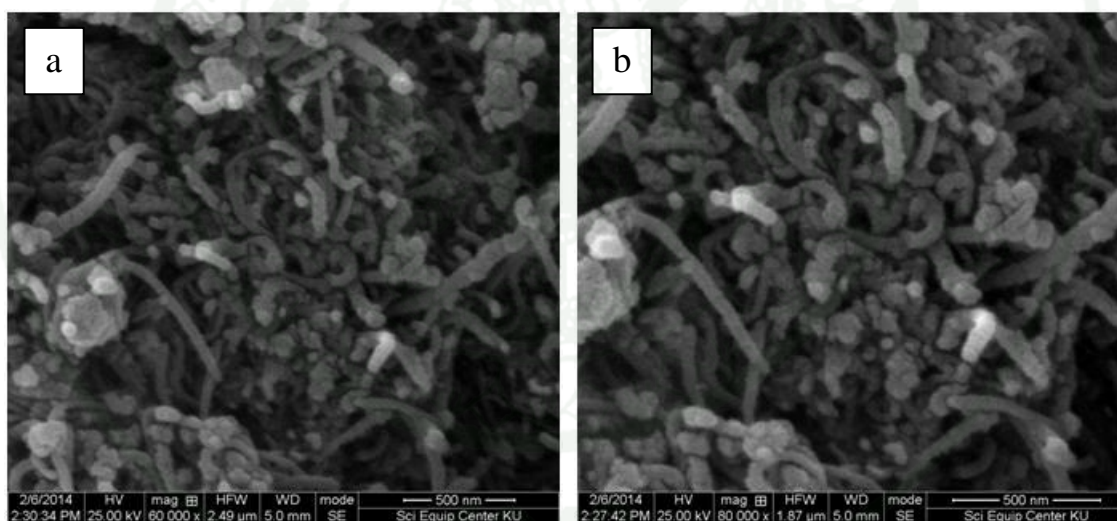
Appendix Figure C11 SEM images of 20%Pd10%Ni10%Sn/CB, (a) $\times 60,000$ and (b) $\times 80,000$.



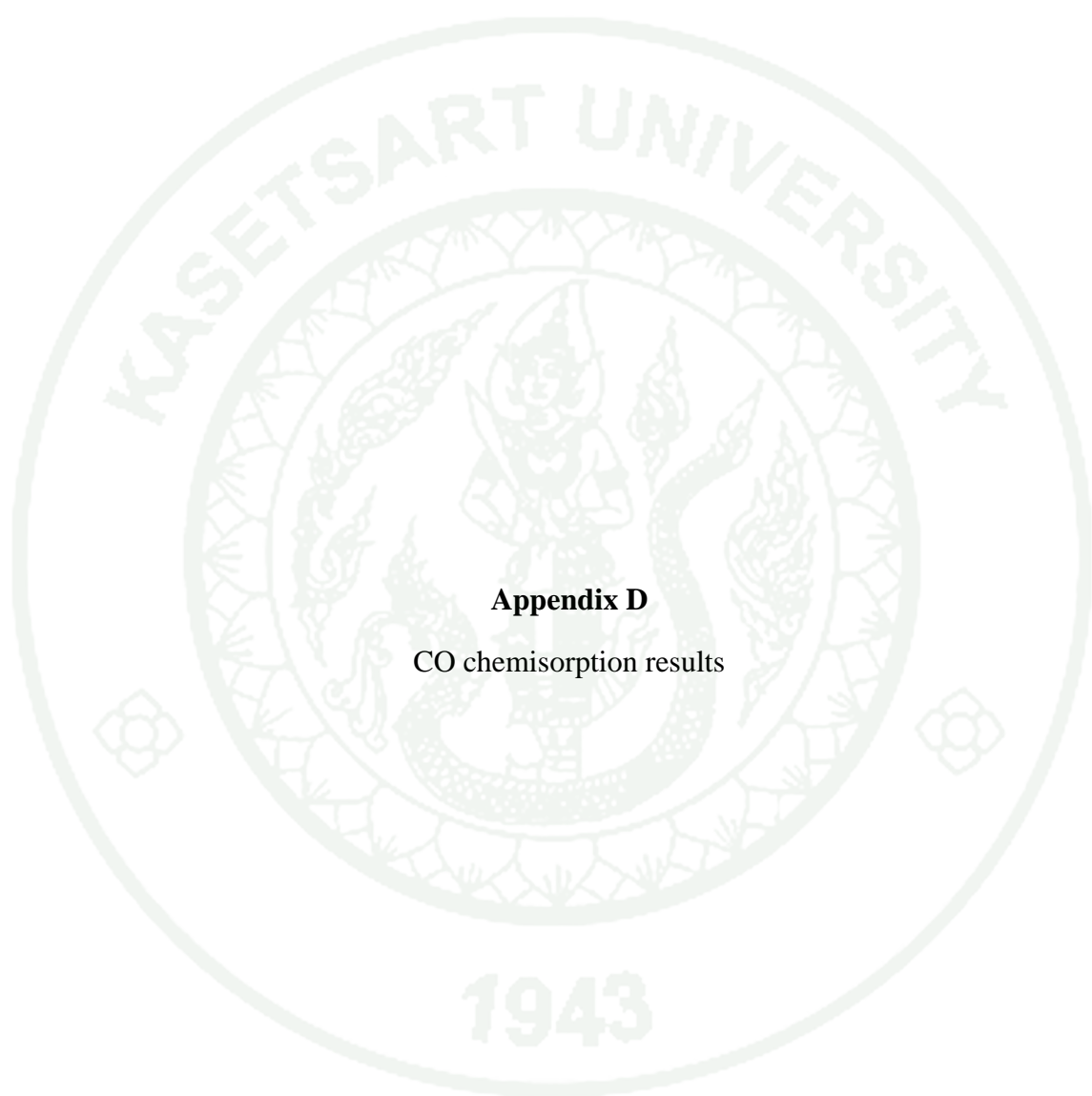
Appendix Figure C12 SEM images of 20%Pd10%Ni10%Sn/CB_{sn}, (a) $\times 60,000$ and (b) $\times 80,000$.



Appendix Figure C13 SEM images of 20%Pd10%Ni10%Sn/MWCNT, (a) $\times 60,000$ and (b) $\times 80,000$.



Appendix Figure C14 SEM images of 20%Pd10%Ni10%Sn/MWCNT_{sn}, (a) $\times 60,000$ and (b) $\times 80,000$.



Appendix D
CO chemisorption results

The CO chemisorption results of catalyst composition

Appendix Table D1 CO chemisorption of 20%Pd/CB (catalyst weight = 0.0250 g).

No	Peak type	Loop temp.(°C)	Loop press (kPa)	Dosing amount (cm ³ (STP))	Area (count)
1	PULSE	32.9	100.81	0.0891	18,288
2	CAL	33	100.78	0.089	19,434
3	CAL	33.1	100.79	0.089	19,485
4	CAL	33.3	100.79	0.0889	19,485

Appendix Table D2 CO chemisorption of 20%Pd20%Sn/CB (catalyst weight = 0.0245 g).

No	Peak type	Loop temp.(°C)	Loop press (kPa)	Dosing amount (cm ³ (STP))	Area (count)
1	PULSE	31.5	100.5	0.0892	19,805
2	CAL	31.5	100.5	0.0892	19,944
3	CAL	31.5	100.5	0.0892	19,988
4	CAL	31.6	100.5	0.0892	19,984

Appendix Table D3 CO chemisorption of 20%Pd20%Ni/CB (catalyst weight = 0.0260 g).

No	Peak type	Loop temp.(°C)	Loop press (kPa)	Dosing amount (cm ³ (STP))	Area (count)
1	PULSE	32.6	100.78	0.0891	17,484
2	CAL	32.6	100.76	0.0891	19,402
3	CAL	32.6	100.78	0.0891	19,472
4	CAL	32.6	100.78	0.0891	19,469

Appendix Table D4 CO chemisorption of 20%Pd5%Ni15%Sn/CB (catalyst weight = 0.0301 g).

No	Peak type	Loop temp.(°C)	Loop press (kPa)	Dosing amount (cm ³ (STP))	Area (count)
1	PULSE	32.1	100.53	0.0891	18,838
2	CAL	32.1	100.53	0.0891	19,539
3	CAL	32.1	100.53	0.0891	19,666
4	CAL	32.1	100.53	0.0891	19,687

Appendix Table D5 CO chemisorption of 20%Pd10%Ni10%Sn/CB (catalyst weight = 0.0278 g).

No	Peak type	Loop temp.(°C)	Loop press (kPa)	Dosing amount (cm ³ (STP))	Area (count)
1	PULSE	32.4	100.64	0.0891	15,318
2	CAL	32.4	100.62	0.089	18,761
3	CAL	32.4	100.62	0.089	18,961
4	CAL	32.4	100.64	0.0891	19,028

Appendix Table D6 CO chemisorption of 20%Pd15%Ni5%Sn/CB (catalyst weight = 0.0240 g).

No	Peak type	Loop temp.(°C)	Loop press (kPa)	Dosing amount (cm ³ (STP))	Area (count)
1	PULSE	32	100.82	0	18,038
2	CAL	32.1	100.82	0	19,662
3	CAL	32.1	100.82	0	19,720
4	CAL	32.1	100.82	0	19,692

The CO chemisorptions of 20%Pd10%Ni10%Sn on various supports

Appendix Table D7 CO chemisorption of 20%Pd10%Ni10%Sn/CB (catalyst weight = 0.0278 g).

No	Peak type	Loop temp.(°C)	Loop press (kPa)	Dosing amount (cm ³ (STP))	Area (count)
1	PULSE	32.4	100.64	0.0891	15,318
2	CAL	32.4	100.62	0.089	18,761
3	CAL	32.4	100.62	0.089	18,961
4	CAL	32.4	100.64	0.0891	19,028

Appendix Table D8 CO chemisorption of 20%Pd10%Ni10%Sn/MWCNT (catalyst weight = 0.0214 g).

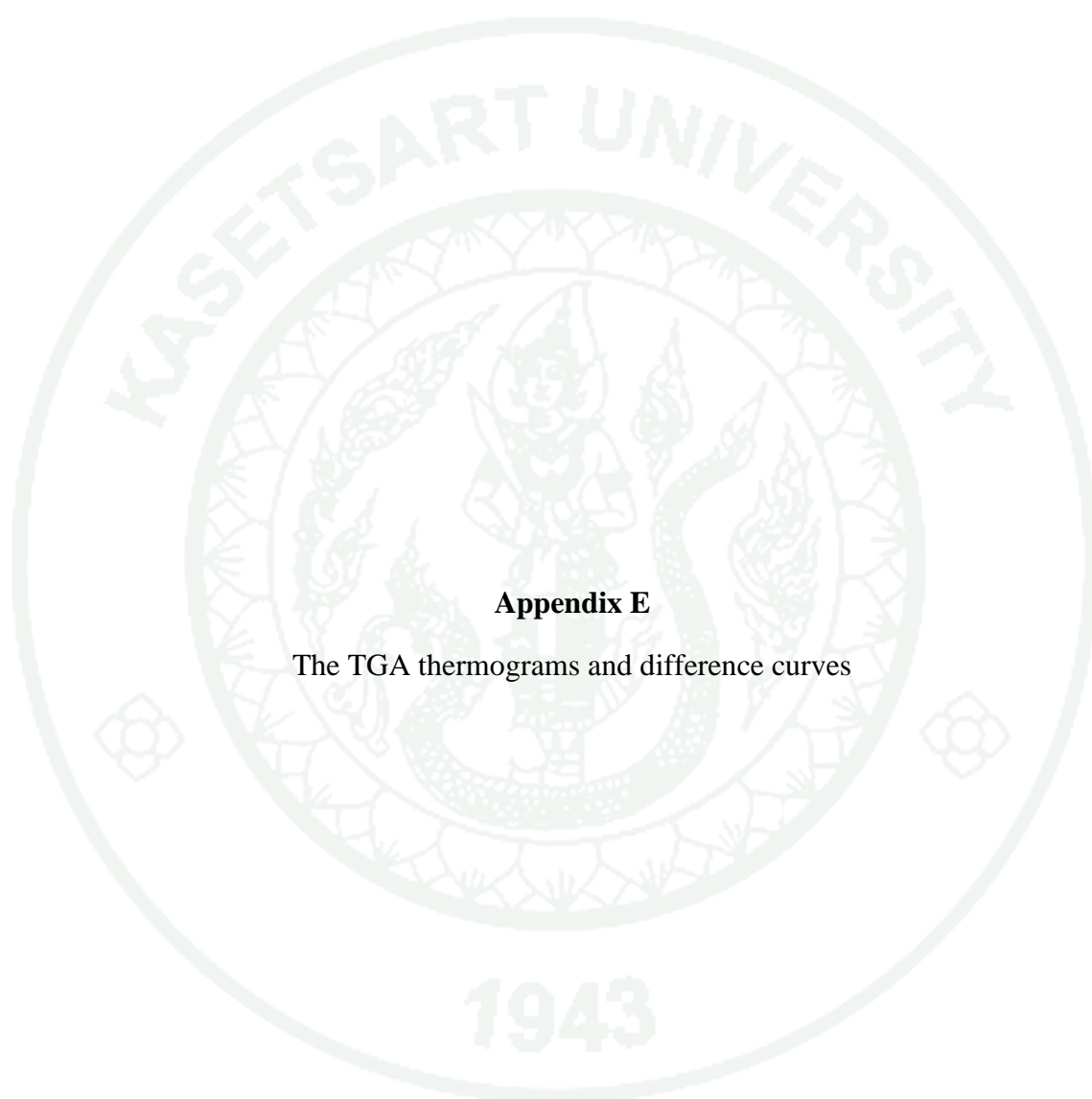
No	Peak type	Loop temp.(°C)	Loop press (kPa)	Dosing amount (cm ³ (STP))	Area (count)
1	PULSE	31.6	100.78	0.0894	17,823
2	CAL	31.6	100.75	0.0894	19,609
3	CAL	31.6	100.75	0.0894	19,640
4	CAL	31.6	100.73	0.0894	19,700

Appendix Table D9 CO chemisorption of 20%Pd10%Ni10%Sn/CB_{sn} (catalyst weight = 0.0216 g).

No	Peak type	Loop temp.(°C)	Loop press (kPa)	Dosing amount (cm ³ (STP))	Area (count)
1	PULSE	32.1	100.43	0.089	15,063
2	CAL	32.2	100.43	0.0889	19,220
3	CAL	32.2	100.44	0.0889	19,410
4	CAL	32.2	100.43	0.0889	19,438

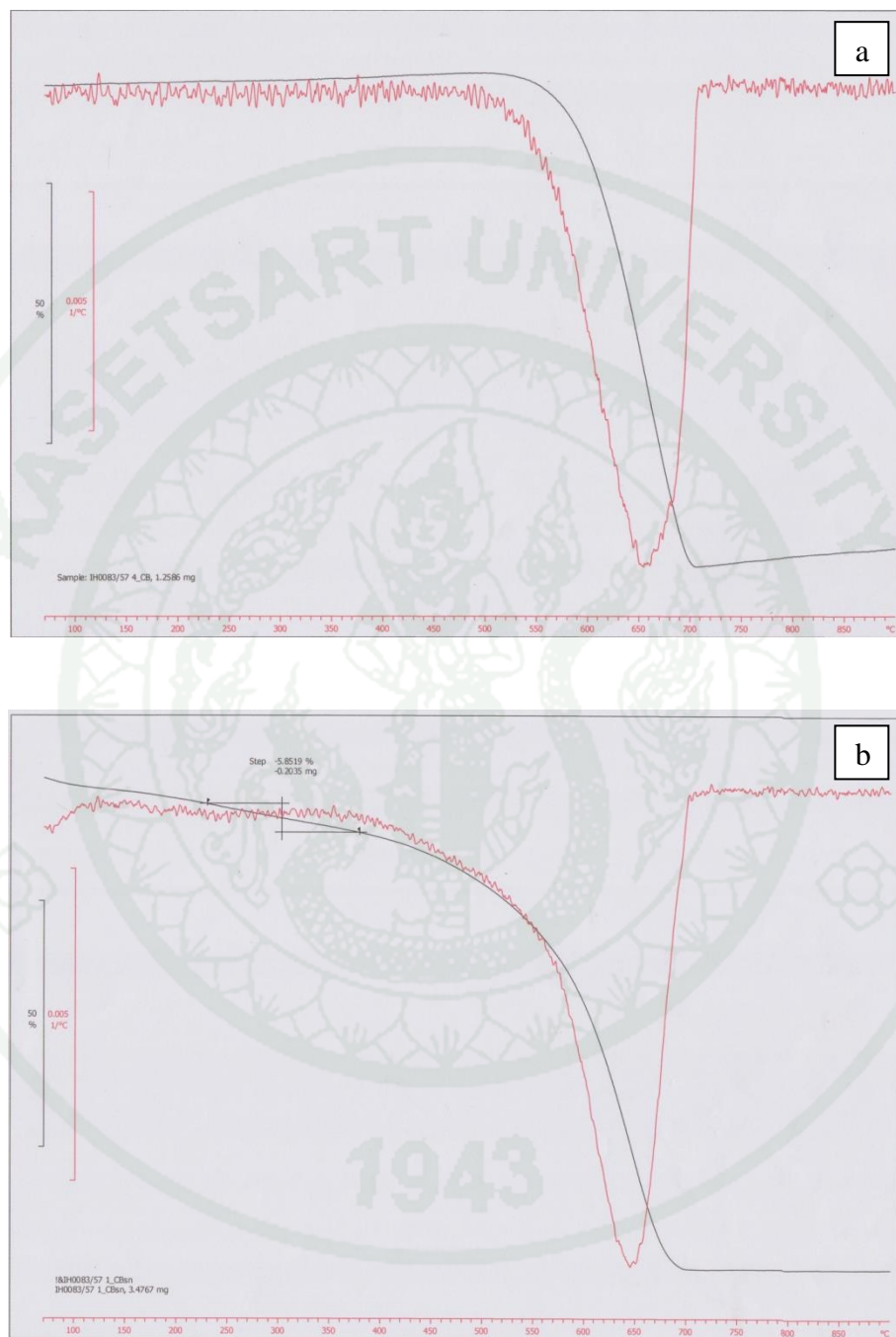
Appendix Table D10 CO chemisorption of 20%Pd10%Ni10%Sn/MWCNT_{sn}
(catalyst weight = 0.0252 g).

No	Peak type	Loop temp.(°C)	Loop press (kPa)	Dosing amount (cm ³ (STP))	Area (count)
1	PULSE	32.2	100.81	0.0893	12,512
2	PULSE	32.2	100.81	0.0893	18,064
3	CAL	32.2	100.81	0.0893	18,333
4	CAL	32.2	100.81	0.0893	18,472
5	CAL	32.2	100.81	0.0893	18,544

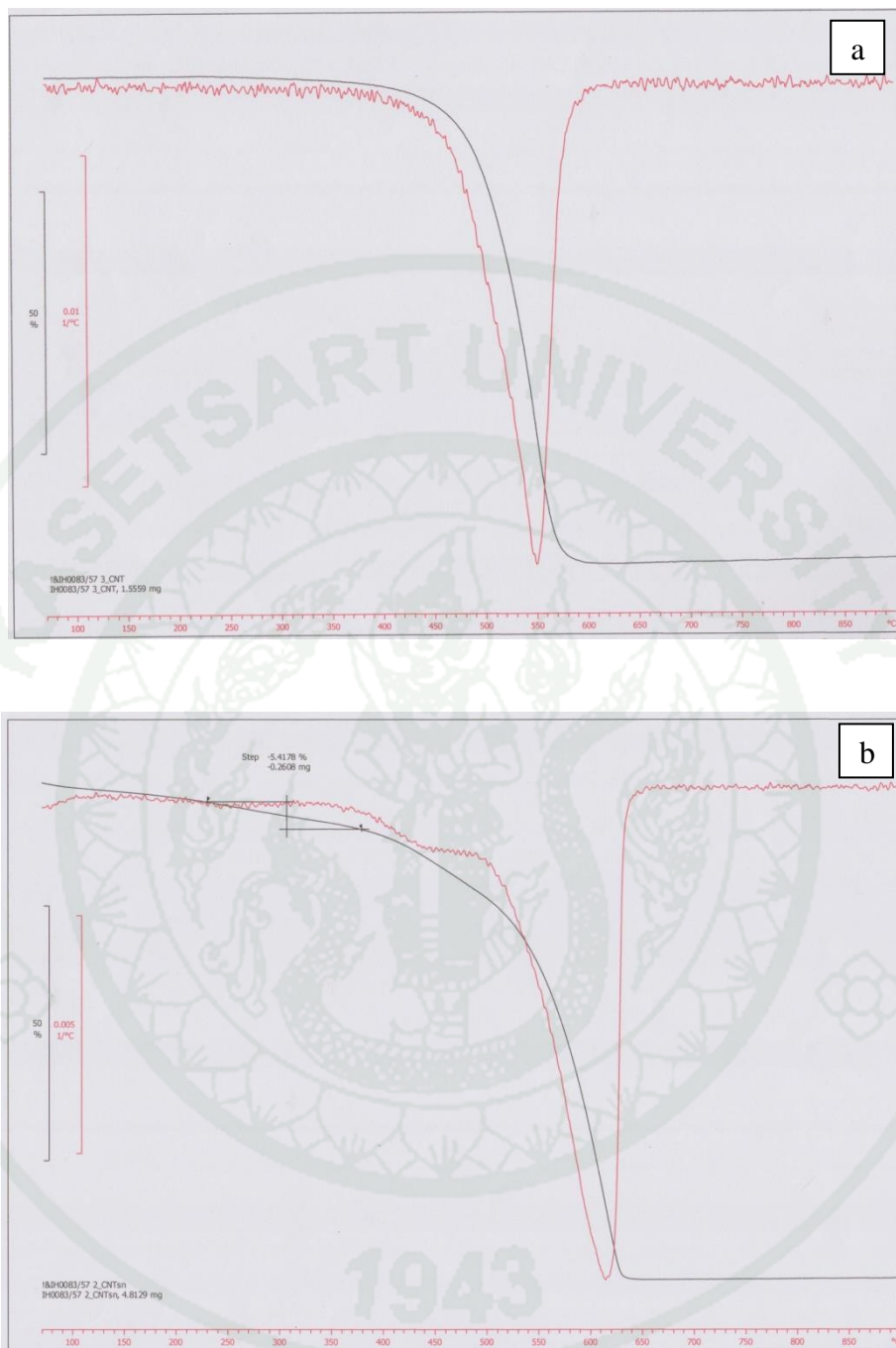


Appendix E

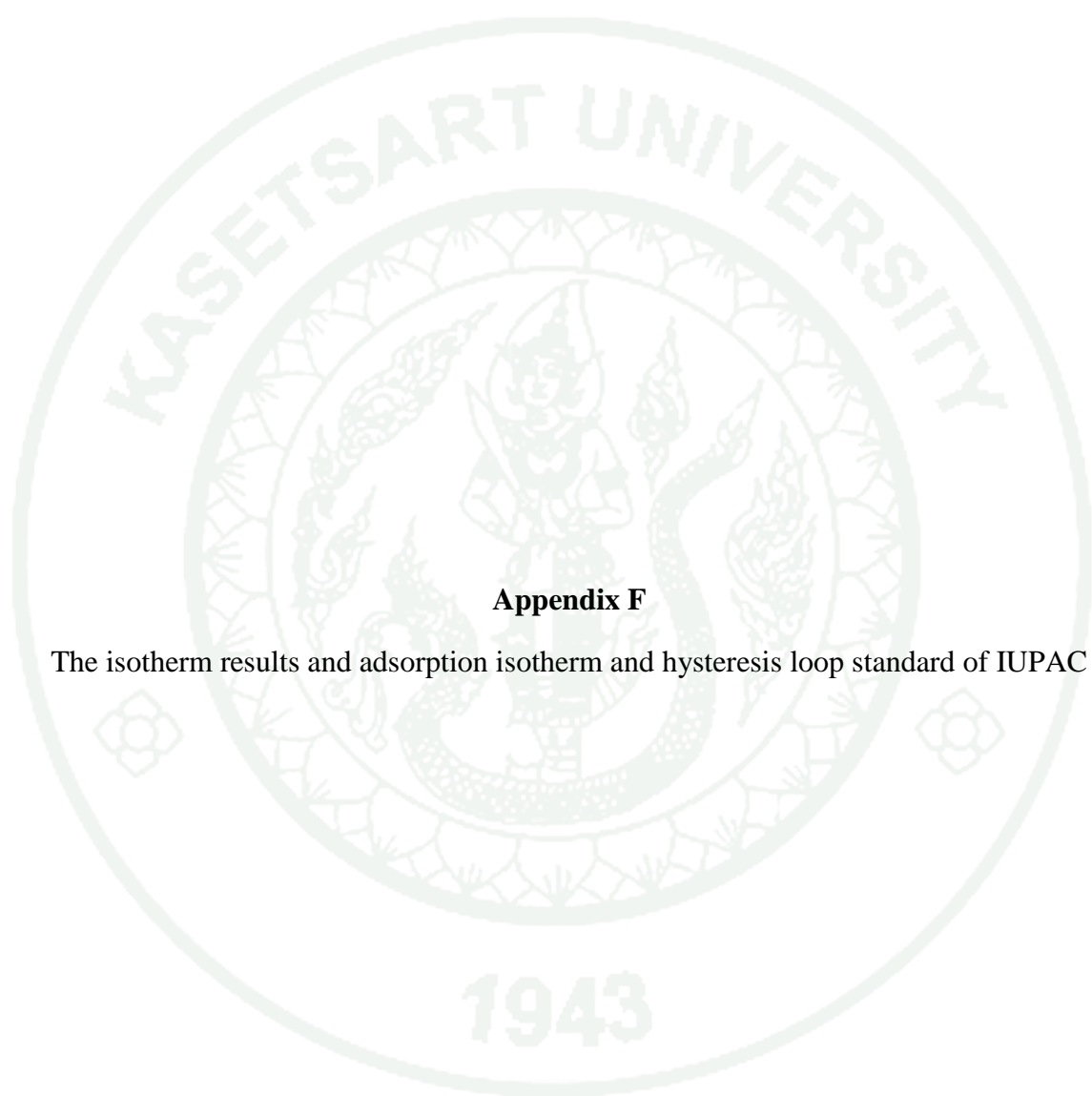
The TGA thermograms and difference curves

TGA thermograms and differential curves

Appendix Figure E1 The TGA thermograms and differential curve of (a) CB and (b) CB_{sn} .



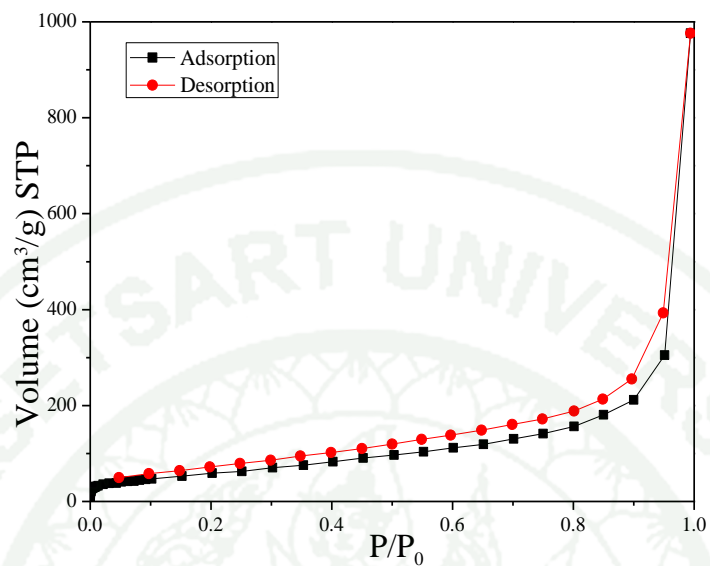
Appendix Figure E2 The TGA thermograms and differential curve of (a) MWCNT and (b) MWCNT_{sn}.



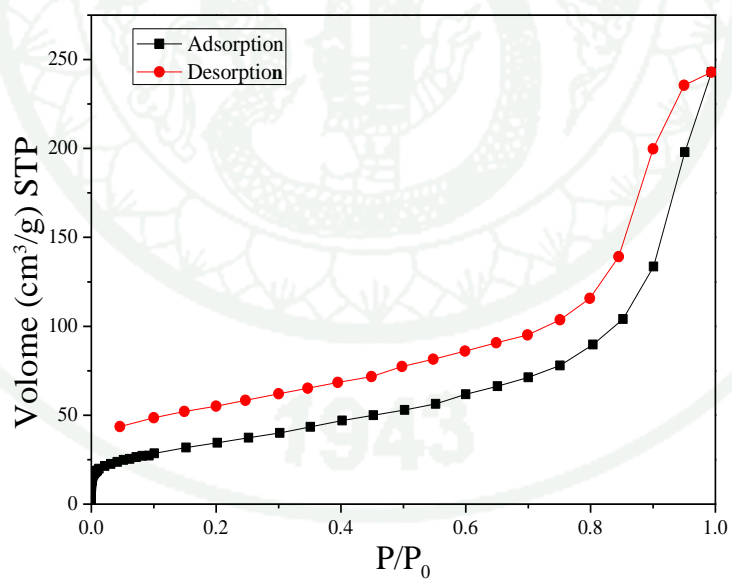
Appendix F

The isotherm results and adsorption isotherm and hysteresis loop standard of IUPAC

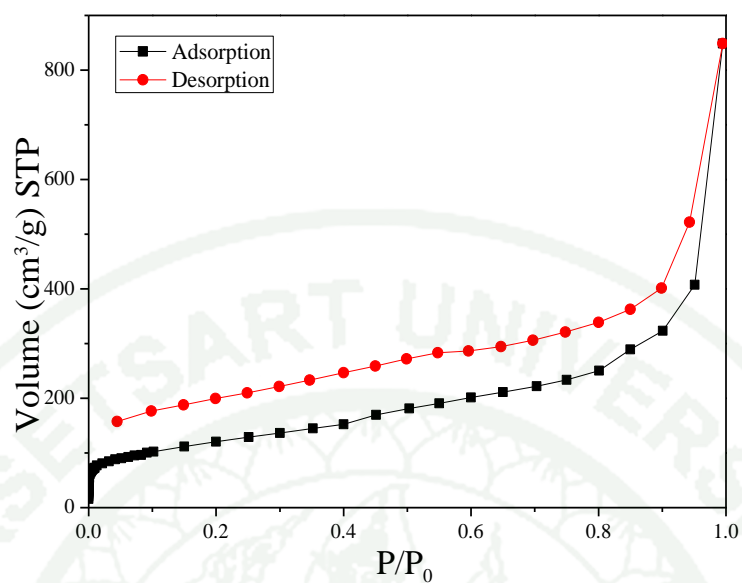
The isotherm results of carbon supports



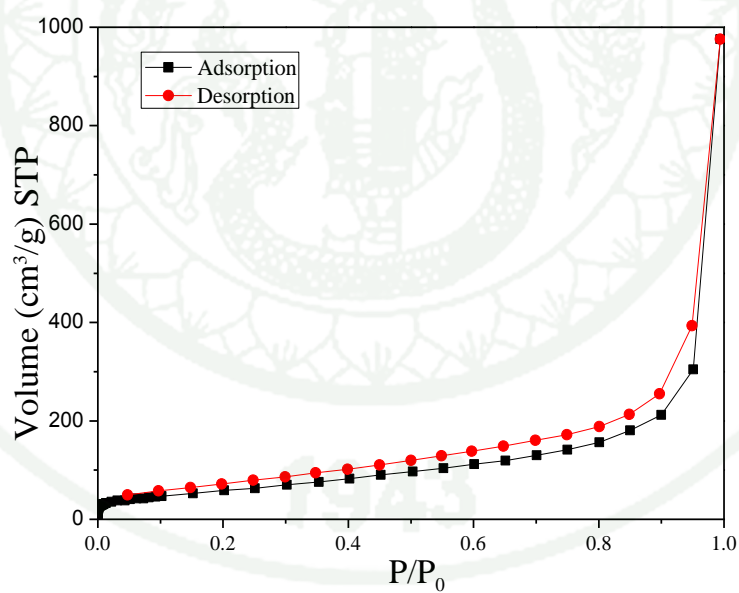
Appendix Figure F1 The isotherm of CB_{sn} support.



Appendix Figure F2 The isotherm of $MWCNT_{sn}$ support.



Appendix Figure F3 The isotherm of CB support.



Appendix Figure F4 The isotherm of MWCNT support.

Adsorption isotherm of the International Union of Pure and Applied Chemistry (IUPAC) standard

The complete adsorption/desorption analysis is called an adsorption isotherm. The six IUPAC standard adsorption isotherms are shown below in Appendix Figure F5, they behave different because the systems demonstrate different gas/solid interactions. The Type I isotherm is a typical isotherm of microporous solids and chemisorption isotherms. Type II is shown for finely divided non-porous solids. Type III and type V are typical of vapor adsorption (i.e. water vapor on hydrophobic materials). Type IV and VI show a hysteresis loop generated by the capillary condensation of the adsorbate in the mesopores of the solid. Finally, the rare type VI step-like isotherm is shown by nitrogen adsorbed on special carbon which is the rare found case (University of Oxford, 2008).



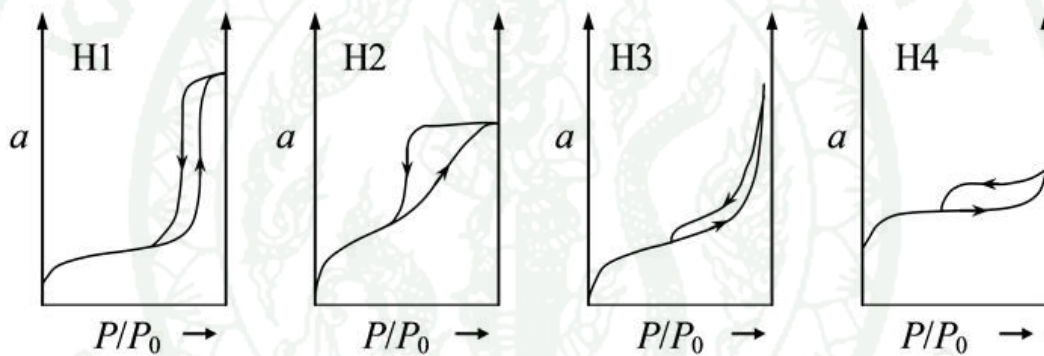
Appendix Figure F5 The adsorption isotherm types of IUPAC standard.

Source: University of Oxford (2008)

The hysteresis loops of IUPAC standard

The hysteresis loops can be divided into four categories based on the IUPAC guideline, as shown in Appendix Figure C6. The H1 and H4 represent two extreme

cases while the H2 and H3 are the intermediate situations. The shapes of hysteresis loops are associated with specific pore structures. For example, porous materials which consist of well aligned, spheres and briquettes can produce an H1 type loop line. Materials of this type tend to have relatively narrow distributions of pore size. For the H2 type loops, the hysteresis loop is wide and its desorption curve is more steep than the adsorption curve. This situation usually occurs when the distributions of pore size radii are wide. The presence of slit-shaped pores and/or panel-shaped particles generates the H3 and H4 curves. However, the exhibition of H4 loops indicates the existence of the micropore.



Appendix Figure F6 The hysteresis loop types of IUPAC standard.

Source: Sing *et al.* (1985)

The calculation of BET surface area

The conversion of the isotherm graph to BET graph is carried out by plotting $1/W[(P/P_0)-1]$ versus P/P_0 (see Appendix Figure F7). The BET surface area (S_{BET}) can be determined from equation (52).

$$\frac{1}{W\left[\frac{P}{P_0}\right]} = \frac{1}{W_m \cdot C} + \frac{(C-1) \cdot P}{W_m \cdot C \cdot P_0} \quad (28)$$

where P is the adsorbate equilibrium pressure
 P_0 is the pressure at room temperature
 C is BET constant
 W is adsorbate weight
 W_m is adsorbate monolayer weight

The slope and intercept of the graph provide the unknown variables C and W_m , respectively. The W_m is then substituted in equation (53) to calculate BET surface area (S_{BET}) (Lowell *et al.*, 2004).

$$S_{BET} = \frac{W_m \cdot \bar{N} \cdot A_x}{\bar{M}} \quad (29)$$

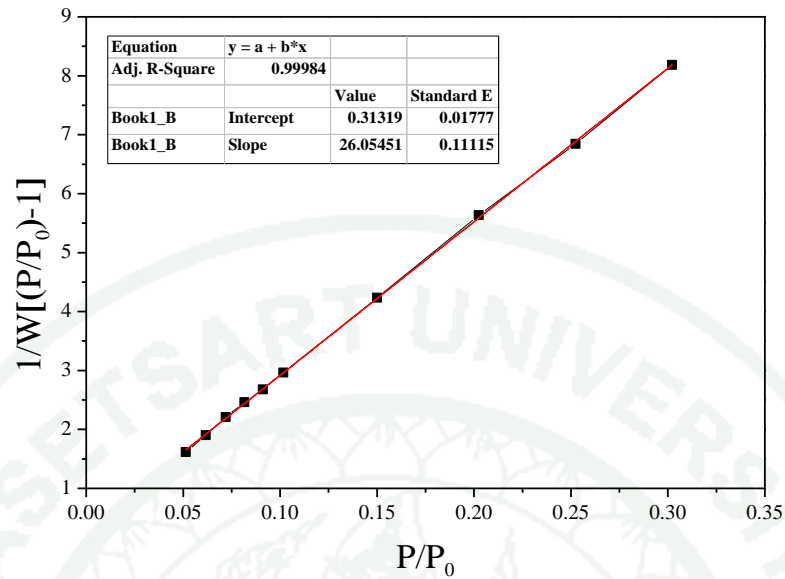
where \bar{M} is adsorbate molecular weight
 A_x is cross-section adsorbate area
 \bar{N} is Avogadro's number

For example of CB_{sn} , after converted isotherm graph to BET graph, fitting the curve to obtain slope and Intercept Y axis

Take slope and intercept Y axis from graph to equal slope and constant variables of this equation (52)

$$\text{Slope} = 26.0545 = (C-1)/(W_m C) \quad (30)$$

$$\text{Intercept Y axis} = 0.31319 = 1/(W_m C) \quad (31)$$



Appendix Figure F7 BET plot of CB_{sn} support.

From eq. (51)

$$C = 1/0.31319W_m \quad (32)$$

Take eq. (52) substitution in eq. (50)

$$26.0545 = (0.31319W_m - 1)/(0.31319W_m^2)$$

$$W_m = 0.0379$$

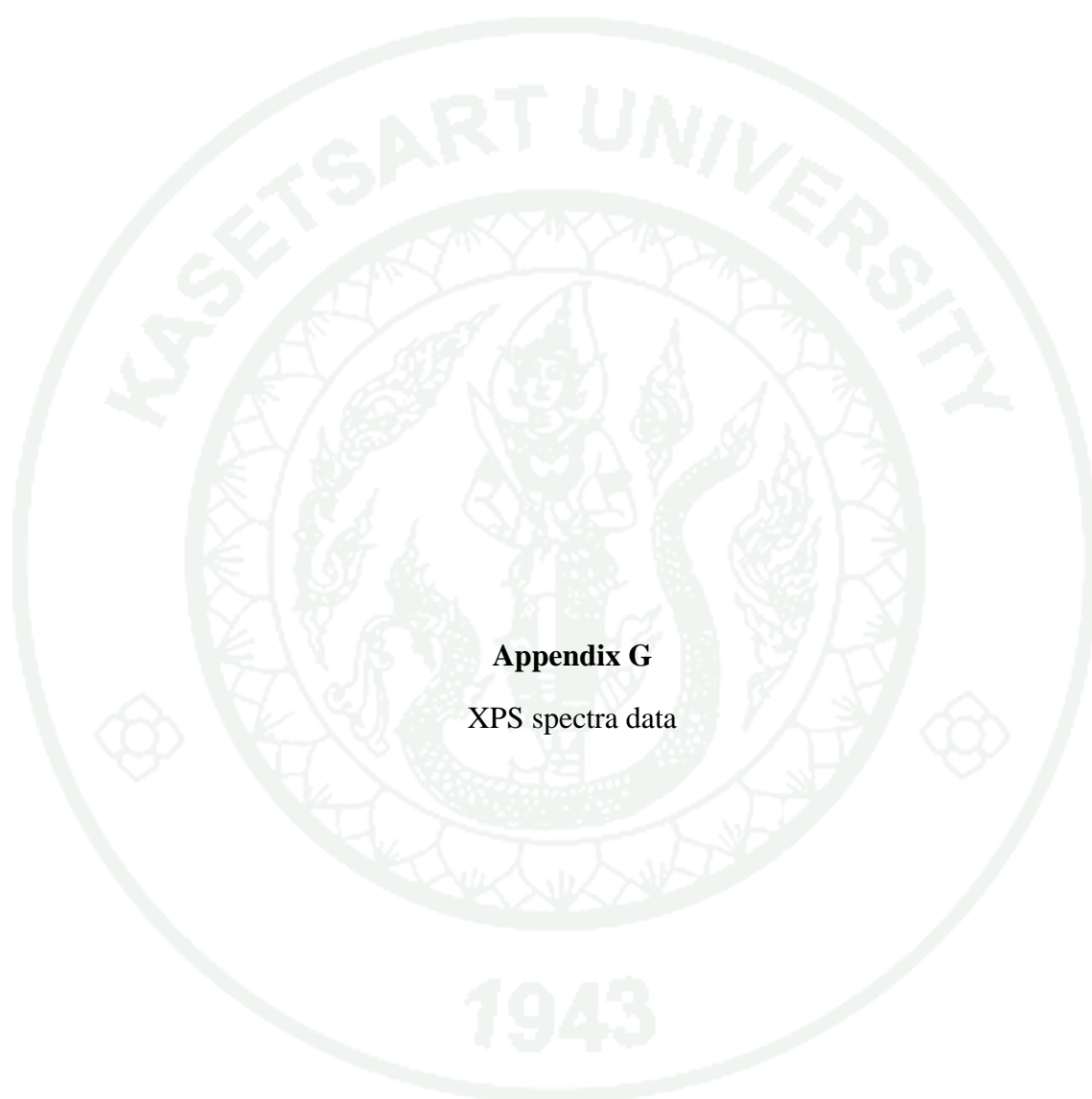
And take W_m substitution in eq. (56) and will obtain

$$C = 84.1907$$

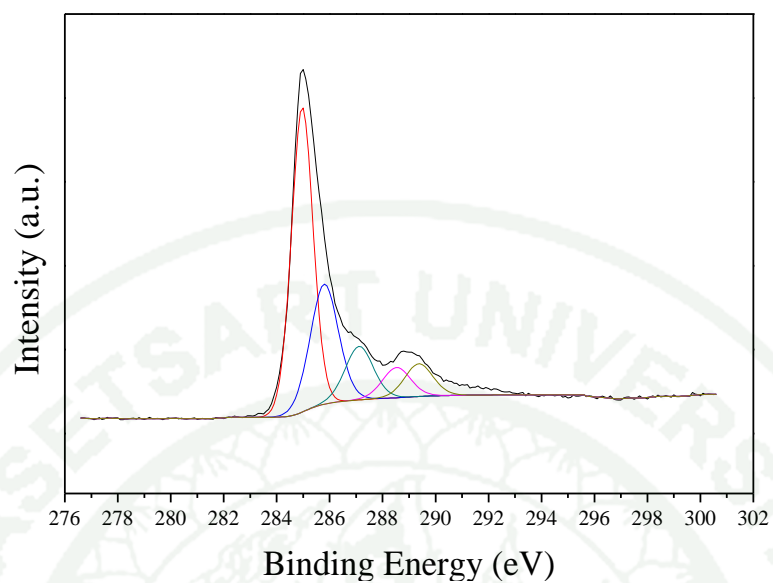
Finally, the W_m was taken into this eq. (53)

$$S_{BET} = 0.0379(6.02 \times 10^{23})(16.2 \times 10^{-20})/28$$

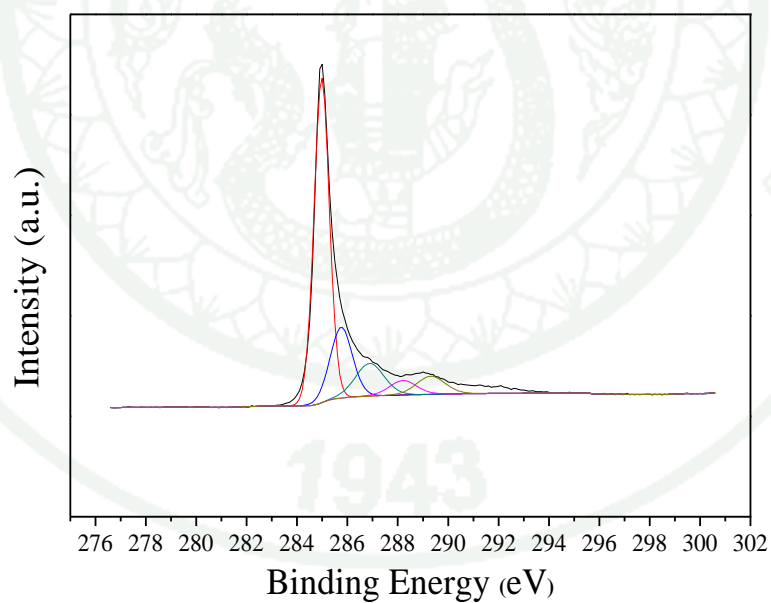
$$S_{BET} = 132.01 \text{ m}^2 \text{ g}^{-1}$$



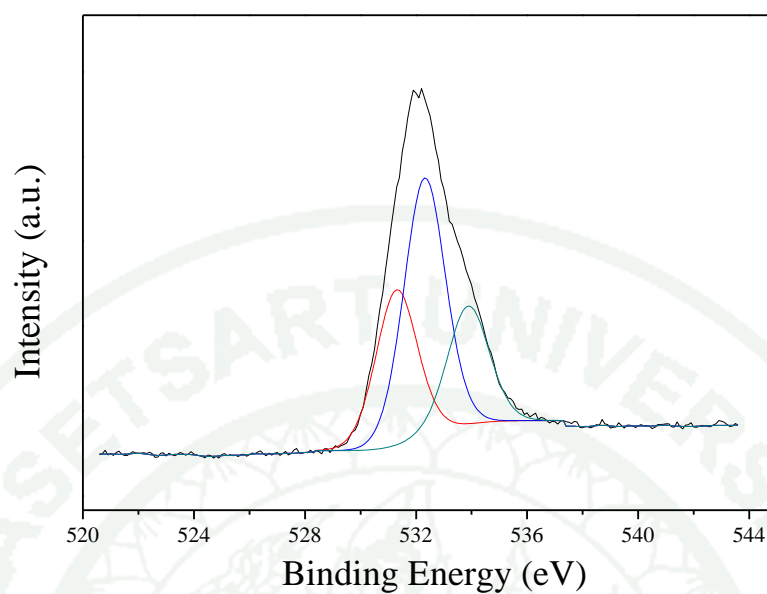
Appendix G
XPS spectra data



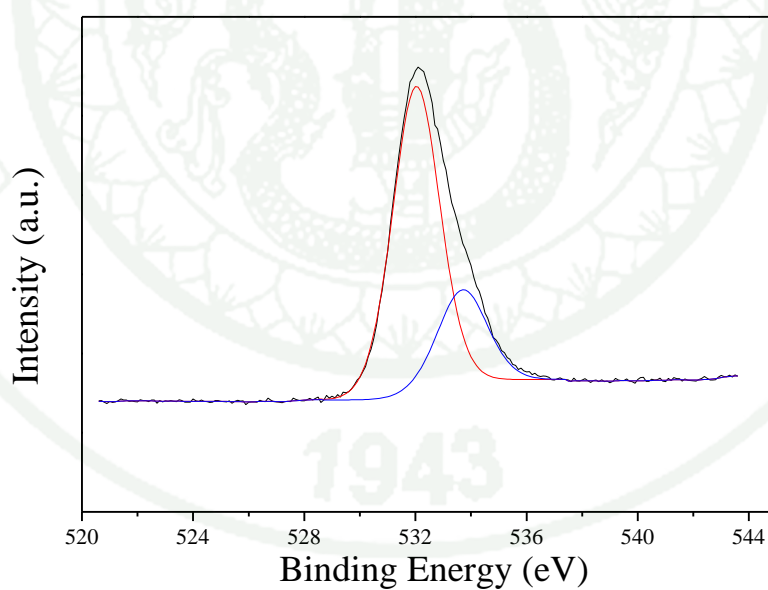
Appendix Figure G1 XPS spectra of C for 20%Pd10%Ni10%Sn/CB_{sn}.



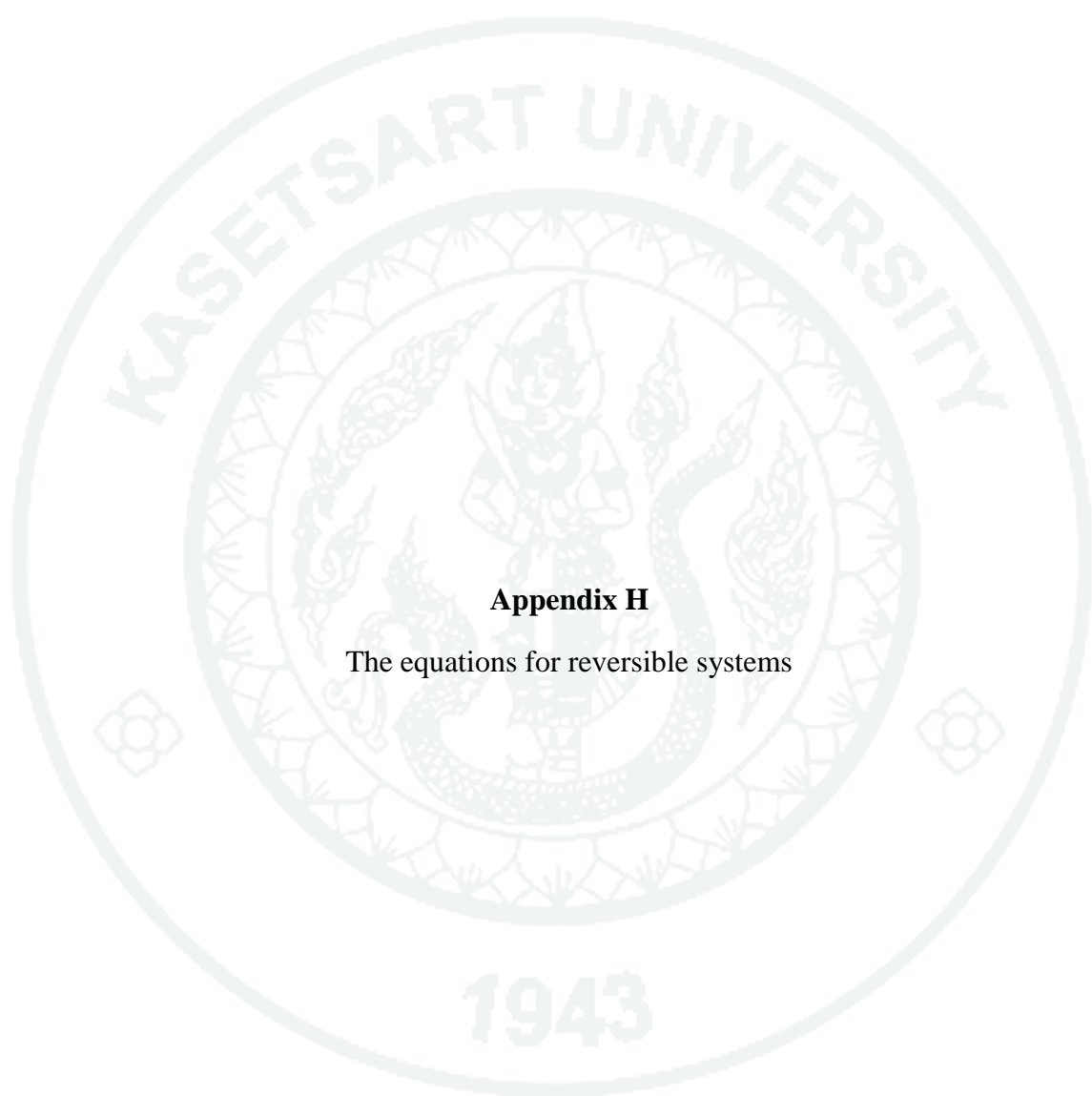
Appendix Figure G2 XPS spectra of C for 20%Pd10%Ni10%Sn/MWCNT_{sn}.



Appendix Figure G3 XPS spectra of oxygen for 20%Pd10%Ni10%Sn/CB_{sn}.



Appendix Figure G4 XPS spectra of oxygen for 20%Pd10%Ni10%Sn/MWCNT_{sn}.



Appendix H

The equations for reversible systems

Useful equations for reversible systems

Electrode potential (E):

$$E = E_i + vt \quad (33)$$

where E_i is the initial potential (V)
 v is the sweep rate ($V s^{-1}$)
 t is the time (s)

When the direction of the potential sweep is switched, the equation becomes,

$$E = E_s - vt \quad (34)$$

Where E_s is the potential at the switching point

$$|E_{pc} - E_{pa}| = 0.0565/n \quad (35)$$

Where (E_{pa}) is the anodic peak potential (V)
 (E_{pc}) is the cathodic peak potential (V)
 n is the number of electrons participating in the redox reactions.

Formal Reduction Potential (E°) is the mean of the E_{pc} and E_{pa} values:

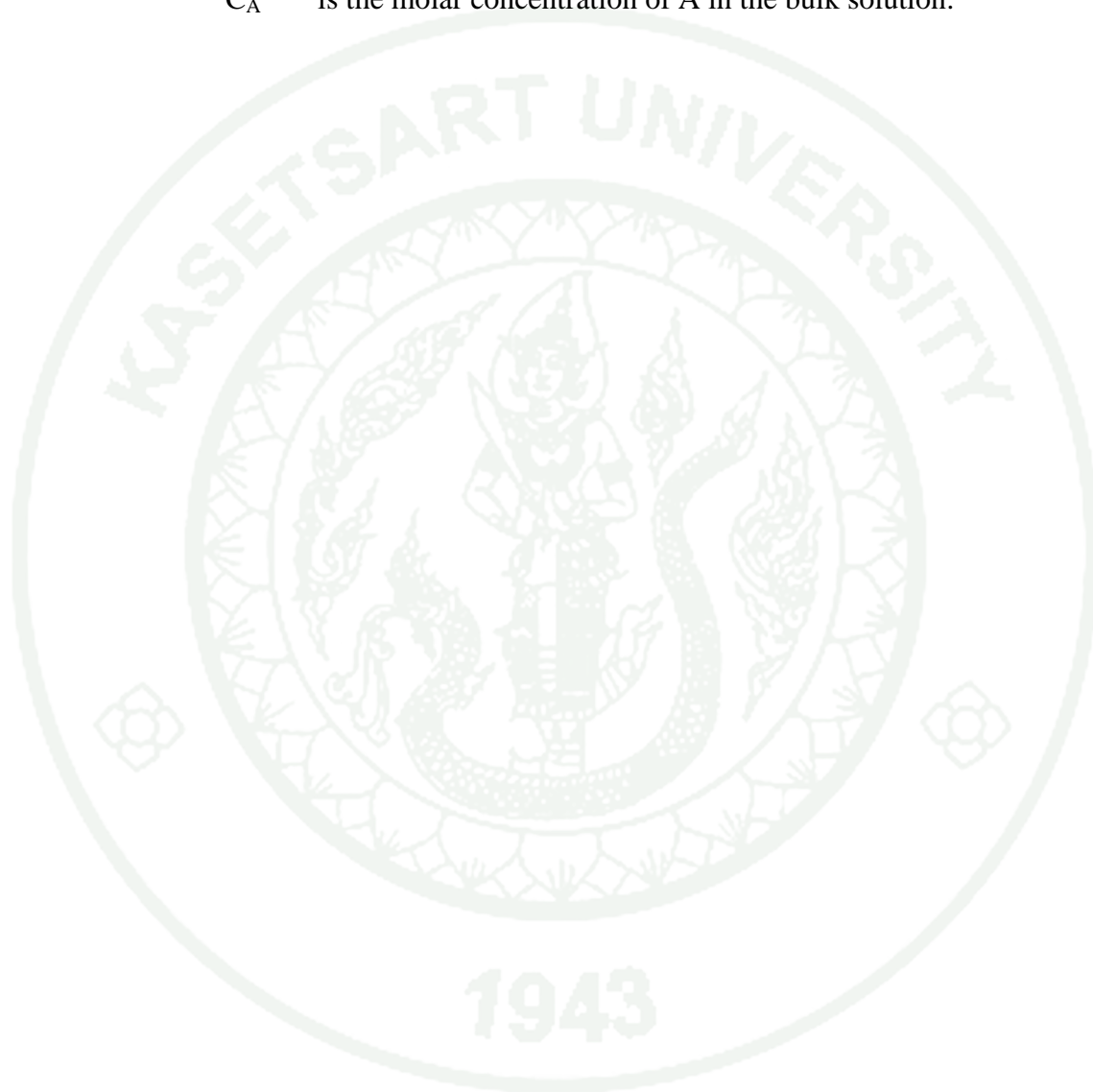
$$E^\circ = (E_{pa} + E_{pc}) / 2 \quad (36)$$

In this case, Fick's Law for mass transfer diffusion can be simplified to give the peak current.

$$i_p = (2.69 \times 10^5) n^{3/2} S D_A^{1/2} V^{1/2} C_A^* \quad (37)$$

where

- n is equal to the number of electrons gained in the reduction
- S is the surface area of the working electrode (cm^2)
- D_A is the diffusion coefficient
- v is the sweep rate (Vs^{-1})
- C_A is the molar concentration of A in the bulk solution.



CURRICULUM VITAE

NAME : Mr. Sompoch Jongsomjit

BIRTH DATE : March 10, 1989

BIRTH PLACE : Chiangmai, Thailand

EDUCATION	<u>YEAR</u>	<u>INSTITUTE</u>	<u>DEGREE/DIPLOMA</u>
	2012	Silpakorn Univ.	B.Eng (Chemical engineering)

POSITIVE/TITLE : -

WORKPLACE : -

SCHOLARSHIP/AWARDS : TAIST-Tokyo Tech Scholarship (Master's degree)
2012-2014